Napier, Austin

299

Austin Napier
"Neutral Particle Production in
Diffractive Pion-Proton and
Proton-Proton Interactions"

Ph. D. thesis, May 1979

E-299

FERMILAB
LIBRARY

FERMILAB
LIBRARY

NEUTRAL PARTICLE PRODUCTION IN DIFFRACTIVE PION-PROTON AND PROTON-PROTON INTERACTIONS AT 147 GeV/c

by

AUSTIN NAPIER

B.S., Massachusetts Institute of Technology
(1969)

SUBMITTED IN PARTIAL FULFILLMENT
OF THE REQUIREMENTS FOR THE
DEGREE OF

DOCTOR OF PHILOSOPHY

at the

MASSACHUSETTS INSTITUTE OF TECHNOLOGY

May 4, 1979

Signature of Author.....Austin Napier.....
Department of Physics, 1979

Certified by.....Richard K. Jaussaud.....
Thesis Supervisor

Accepted by.....George Fred Koster.....
Chairman, Departmental Committee

AAB487

NEUTRAL PARTICLE PRODUCTION IN DIFFRACTIVE PION-PROTON AND PROTON-PROTON INTERACTIONS AT 147 GeV/c

by

AUSTIN NAPIER

Submitted to the Department of Physics
on May 4, 1979 in partial fulfillment of the requirements
for the Degree of Doctor of Philosophy

ABSTRACT

A 273,000 picture exposure of the Fermilab 30-Inch Hybrid Bubble Chamber Spectrometer has been made to study π^+, K^+, and proton collisions with a proton target. A prototype lead glass gamma detector was used to determine energy and production angles of forward gamma rays and neutral pions. Single particle π^0 distributions have been compared with $\pi^\pm$ distributions in π^+-proton and proton-proton events. Production of fast π^0 and π^- in the proton beam was strongly suppressed relative to that observed in the π^+ beam. Production of ρ^0 and ρ^+, associated with the π^+beam, contributes to this effect. A sample of leading particle events was isolated by a selection procedure based on the kinematical configuration of all charged particles in the event. Cross sections, charge multiplicity distributions, and single particle distributions were obtained. The leading particle cross sections are predominantly diffractive, however, a decrease at higher energies is expected, due to PPR contributions in the context of a triple-Regge model.

Thesis Supervisor: Richard K. Yamamoto

Title: Professor of Physics

ACKNOWLEDGEMENTS

I would like to thank Professors Lee Grodzins and Robert I. Hulsizer for stimulating my initial interest in elementary particle physics as an undergraduate. It was a pleasure working with the members of the APC group through the course of my graduate study. I feel privileged to have worked with Professors Robert I. Hulsizer, Vera Kistiakowsky, and Irwin A. Pless. I deeply value the guidance, criticism, advice, and encouragement of my thesis supervisor, Professor Richard K. Yamamoto. I am especially grateful for his sharing of insight and knowledge in many lengthy conversations during my two-year stay at Fermilab.

I would like to thank the many people who contributed to the success of the experiment. Special thanks go to Marianne von Randow and the scanning staff, the PEPR operators, who performed the measurements, especially George Moody, and Ragnhild Gundersen who meticulously ran the track reconstruction programs. Bernard Wadsworth, Garry Schulze, and Charles Forte maintained high standards for the PEPR hardware. Special thanks go to Charles Forte, also, for his superb photography of the computer displays. Steven Myerow provided display subroutines and gave his time unselfishly to resolve software problems.

It was a pleasure conversing and working with Dr. James Brau throughout the experiment. During the detector test, it was also a pleasure to work with Luigi Ventura, Gianni Zumerle, Marco De Giorgi, Renato Conte, and Dino and Lucia Zanello. Marvin Johnson, Gordon Koizumi, Cecil Needles, and James Walker of Fermilab provided a great deal of technical assistance.

Gordon Koizumi and Michael Nazaretz contributed much extra time and effort in the preparation and execution of the experiment.

I am grateful to Professor Peter Stamer and Dr. Lawrence Bachman for supplying PEPR measurements soon after the experiment was completed.

Many members of the International Hybrid System Consortium have been helpful, directly and indirectly.

In particular, I would like to acknowledge Professors E.B. Brucker, William Bugg, Aharon Levy, Thomas Ludlam, Richard Plano, Terrence L. Watts, and Mildred Widgoff, and Drs. Fernando Barreiro, Odette Benary, David Brick, and Douglas Fong.

I would also like to take the opportunity to mention the following people whose sharing of knowledge and experience enhanced my stay at M.I.T.: Professor Elizabeth Hafen, Drs. Pierre Trepagnier, Patrick Miller, Jerome Silverman, and James Bober, Thomas Frank, and Steve Tether.

And, most of all, I wish to thank my partner, Linda Napier, for her constant love and support (and to acknowledge her extraordinary feat of typing this manuscript twice within one week).

There is no way of expressing the sincere gratitude I hold for the support given to me by my parents, parents-in-law, and many patient friends and relatives!

TABLE OF CONTENTS

Abstract 2

Acknowledgements..... 3

I. INTRODUCTION 6

II. DIFFRACTIVE PROCESSES..... 9

III. THE FERMILAB HYBRID 30-INCH BUBBLE CHAMBER SPECTROMETER 23

A. BUBBLE CHAMBER 23

B. PROPORTIONAL WIRE CHAMBER SYSTEM 28

IV. DATA REDUCTION AND PROCESSING 33

A. FILM SCANNING AND MEASURING 36

B. TRACK RECONSTRUCTION 42

C. DATA SAMPLE 47

V. FORWARD GAMMA DETECTOR 54

A. STABILITY AND CALIBRATION 59

B. GAMMA PROGRAM DESCRIPTION 70

1) SHOWER LOCATION 77

2) SHOWER PROFILE FIT 79

3) ENERGY FIT 81

C. ACCEPTANCE 93

D. DATA AND RESULTS 99

VI. EVIDENCE FOR DIFFRACTION DISSOCIATION OF HADRONS... 110

A. TWO COMPONENT MODELS..... 110

B. RAPIDITY GAP ANALYSIS 117

C. INCLUSIVE SINGLE PARTICLE DISTRIBUTIONS 134

1) CHARGED PARTICLE DISTRIBUTIONS..... 134

2) NEUTRAL PION DISTRIBUTIONS..... 144

D. RESONANCE PRODUCTION..... 159

VII. DISCUSSION AND CONCLUSIONS 169

Appendix 171

References 173

List of Figures 178

List of Tables 183

INTRODUCTION

The diffractive scattering of elementary particles has been the subject of extensive study in recent years, both due to its own inherent interest and because it is related by unitarity to other elementary particle interaction mechanisms. As particle accelerators provided higher beam energies, striking kinematic differences were observed between diffractive and non-diffractive interactions. Diffractive scattering of the beam or target particle yields a quasi-elastically scattered particle accompanied by excitation and subsequent break-up of the other particle. These excited states are predominantly of low invariant mass and decay into low multiplicity final states. The spectrum of excited states can yield important information regarding the internal structure of the initial hadron.

This thesis presents a detailed study of low multiplicity final states occurring in $\pi^+ p$ and pp interactions at 147 GeV/c beam momentum, including separation of diffractive and non-diffractive events, and examination of the role of neutral particles. The data come from a 273,000 picture exposure of the Fermilab 30" hydrogen bubble chamber spectrometer during November, 1976, the second phase of Fermilab experiment E299. The bubble chamber film allows measurements of all charged particle momenta in the final state, and the spectrometer provides high-resolution momentum measurements of fast

charged secondaries. The unique feature of this experiment is an electromagnetic shower detector at the downstream end of the spectrometer which allows measurement of the energies and production angles of forward-going gamma rays, electrons, and positrons. Additional information comes from gamma conversions, neutral hadron decays, and neutral hadron interactions observed in the bubble chamber. The production of π^0 mesons, as observed via $\pi^0 \rightarrow \gamma\gamma$, is compared with that of π^+ and π^- in terms of single particle distributions. Separation of diffractive events is accomplished by classifying each event according to the rapidity distribution of its charged final state particles, i.e. beam-diffractive and target-diffractive events. Cross sections are obtained for the diffractive excitation of beam and target particles. There is evidence for the dominance of two body processes in the non-diffractive two-prong events, as opposed to "central" particle production such as observed in events with high multiplicity. Resonance production is examined with special attention to π^+ beam dissociation events.

The following section will present an abbreviated introduction to diffractive processes and a survey of some recent approaches taken by theory. The scope of present experimental knowledge is then outlined and the importance of measurements of exclusive final states is discussed. Sections III and IV describe, respectively, the Fermilab Hybrid Spectrometer and the processing chain necessary to reconstruct events in space

and provide final state particle information. Section V details the assembly and performance of the forward gamma detector and explains the shower location algorithm.

II. Diffractive Processes

Diffractive scattering of hadrons on protons, neutrons, and nuclei has been widely studied (reviews: Leith, 1974; Whitmore, 1974; Derrick, 1975). In this section the principal characteristics of diffractive scattering are described, and the reasons for interest in such processes are summarized.

Classically, the term diffraction is applied to the scattering of light by an aperture or an obstacle. In the scattering process light may also be absorbed. The problem is to calculate the intensity and, perhaps, the polarization of scattered electromagnetic radiation. Kirchhoff applied Huygens' ideas on the superposition of waves to formulate a scalar theory, in which the scattered wave at a point distant from the scatterer is described as a superposition of outgoing spherical waves. For diffraction of a plane wave through an aperture, the amplitude ψ at distance $\vec{R}$ is:

$$\psi(\vec{R}) = \frac{k}{4\pi i} \int d^2r\, \psi_0 \; S(\vec{r}) \; (1 + \cos\theta') \frac{e^{ik|\vec{R}-\vec{r}|}}{|\vec{R}-\vec{r}|} \qquad (1)$$

ψ_0 is the amplitude of the incident wave and $S(\vec{r})$ describes the amplitude variation in the aperture at point $\vec{r}$. $k = 2\pi/\lambda$ where λ is the wavelength, and $\cos\theta' = \vec{n} \cdot (\vec{R}-\vec{r})/\vec{R}-\vec{r}$ where $\vec{n}$ is a unit vector giving the direction of propagation of the incident wave.

Generally the dimensions of the scatterer ($\sim L$) are larger than the wavelength of the incident radiation ($KL \gg 1$). Two zones have been classically distinguished: points at great

distances $(L/R) << 1$ are said to lie in the Fraunhofer zone if $(KL^2/R) << 1$ and in the Fresnel zone when $(kL^2/R) \approx 1$. For incident pions or protons on nuclei, Fraunhofer diffraction is the important case, since:

$$KL^2 = \frac{p}{\hbar} \sim \frac{150 \text{ GeV}}{.2 \text{ GeV-f.}} (1\text{f.})^2 = 750 \text{ fermis.} \quad (2)$$

and typically we observe final state particles at distances at least as large as centimeters from the interaction region. In the Fraunhofer zone, we may write:

$$|\vec{R} - \vec{r}| \cong R - \left(\frac{\underline{X}x + \underline{Y}y}{R} \right) \quad (3)$$

where $\vec{R} = (\underline{X}, \underline{Y}, Z)$ and $\vec{r} = (x, y, 0)$ for an aperture in the plane at $z = \emptyset$, and equation (1) reduces to:

$$\psi_{\text{Scat.}}(R) = \psi_o \frac{e^{ikR}}{R} f(\vec{q}) \quad (4)$$

$$f(\vec{q}) \equiv \frac{k}{2\pi i} \int d^2r \left[S(\vec{r}) - 1 \right] e^{i\vec{q} \cdot \vec{r}} \quad (5)$$

where the contribution of the incident wave has been removed. The vector q is the "momentum transfer" defined as $\vec{q} \equiv (K \frac{\underline{X}}{R}, K \frac{\underline{Y}}{R}, 0)$, and $f(\vec{q})$ is the scattering amplitude (e.g. Messiah, 1966). Once the scattering amplitude

is known, the diffraction problem is solved. In quantum scattering theory ($S(\vec{r})$ becomes the S-matrix, and we may write $S(\vec{r}) = e^{i\Delta(\vec{r})}$ where $\Delta(\vec{r})$ is a complex phase. $\mathrm{Im}\,\Delta$ is the absorption of the incoming wave and $\mathrm{Re}\,\Delta$ is its phase shift.

Spherical symmetry allows analytical integration for some cases. In particular, for a circular aperture we obtain:

$$f(\vec{q}) = ikR^2 J_1(qR)/(qR) \tag{6}$$

where $J_1(qR)$ is the Bessel function of the first kind. This case is typical of diffractive scattering -- sharply peaked forward distributions with, in some cases, secondary maxima of considerably smaller size.

The mathematical formalism developed to deal with the wave-like nature of light provided a sound basis for the scattering theory of wave packets in quantum mechanics (e.g. Messiah, 1966). The optical analogy has been often used in nuclear and particle physics as well (e.g. Perl, 1974). A particle or nucleus is regarded as an opaque object with certain probabilities for scattering an incoming particle or "absorbing" it through various reaction channels.

The simplest case in quantum scattering theory is the interaction of two identical spinless particles in the center of mass (CM) frame. The partial wave expansion expresses

the scattered wave in terms of definite angular momentum states:

$$\psi_{scat}(\vec{R}) = \frac{1}{2ik}\left(\frac{e^{ikR}}{R}\right)\sum_{\ell=0}^{\infty}(2\ell+1)P_\ell(\cos\theta)\left[S_\ell-1\right] \tag{7}$$

giving:

$$f(\theta) = \frac{1}{2ik}\sum_{\ell=0}^{\infty}(2\ell+1)\,P_\ell(\cos\theta)\,\left[S_\ell-1\right] \tag{8}$$

where P_ℓ is a Legendre polynomial and $|S_\ell-1|$ is the amplitude of the ℓth particle wave. Unitarity requires $0 \leq |S_\ell|^2 \leq 1$.

The differential elastic cross section is given by:

$$\frac{d\sigma}{d\Omega} = f(\theta)^2 \tag{9}$$

using $$\int_{-1}^{1} P_\ell(x)P_{\ell'}(x)dx = \frac{2\delta_{\ell\ell'}}{(2\ell+1)} \tag{10}$$

and the full elastic cross section is:

$$\sigma_{el} = \int |f(\theta)|^2 d\Omega = \sum_{\ell=0}^{\infty}\frac{\pi}{k^2}(2\ell+1)\,|1-S_\ell|^2 \tag{11}$$

The ratio of scattered to incident flux in the lth partial wave is $\pi(2\ell+1)/k^2$.

The inelastic cross section is proportional to that fraction of the incident wave which was absorbed:

$$\sigma_{INEL} = \sum_{\ell=0}^{\infty}\frac{\pi}{k^2}(2\ell+1)\left[1-|S_\ell|^2\right] \tag{12}$$

The total cross section is the sum of the elastic and inelastic cross sections:

$$\sigma_{total} = \sum_{\ell=0}^{\infty} \frac{\pi}{k^2} (2\ell+1) \cdot 2(1 - \mathrm{Re}S_\ell) \tag{13}$$

If we write $\ell = kb$, where b is the impact parameter, for the classical case to which many angular momentum states contribute, we find:

$$f(\theta) \to \frac{1}{2ik} \int_0^\infty d\ell \underbrace{(2\ell+1)}_{2\ell} \underbrace{P_\ell(\cos\theta)}_{J_0(\ell \sin\theta)} \left[S(\ell)-1\right] \tag{14}$$

for θ small; ℓ large

$$f(\theta) \cong \frac{k}{i} \int_0^\infty b\,db \; J_0(kb\sin\theta) \; \left[S(b)-1\right] \tag{15}$$

The equality:

$$J_0(x) = \frac{1}{2\pi} \int_0^{2\pi} e^{ix\cos\theta} \, d\theta \tag{16}$$

can be used along with $|\vec{q}| = k \sin\theta$ to obtain:

$$f(\theta) = \frac{k}{2\pi i} \int d^2b \; \left[S(\vec{b}) - 1\right] e^{i\vec{q}\cdot\vec{b}} \tag{17}$$

identical to the result found from Kirchhoff's formula.

This simple case illustrates basic features of diffractive scattering of hadrons: 1) a superposition of a large number of partial waves produces a diffractive cross section sharply peaked at small scattering angles, and 2) the diffrac-

tive and absorptive, i.e. elastic and inelastic, amplitudes are closely connected.

Glauber (1955), Feinberg and Pomeranchuk (1956), and Good and Walker (1960) considered the state of a hadron passing through a nucleus as a linear combination of eigenstates having the same intrinsic quantum numbers as the incident hadron. The observed final state will consist of a system of one or more hadrons with these intrinsic quantum numbers, i.e. charge, isotopic spin, strangeness, baryon number, and G-parity. However, the spin and parity of the final state may be different since angular momentum may be transferred to the incident particle during scattering.

Two-body scattering processes at high energy are commonly described using the Mandelstam variables s, t, u. The differential cross section is then written:

$$\frac{d\sigma}{dt} = \frac{\pi}{p^2} \frac{d\sigma}{d\Omega} = \pi \, |T(s,t)|^2 \tag{18}$$

where T(s,t) is the complex scattering amplitude, and p is the incident momentum in the CM frame.

The major phenomenological characteristics of diffractive processes in hadron-hadron interactions have been summarized by Leith (1974):

1) Cross sections, both elastic and total, become energy independent at high energies, except for factors of ℓn s.

2) Diffractive amplitudes are mostly imaginary.

3) Diffractive amplitudes factorize. That is, the ratio of two-body scattering amplitudes:

$$\frac{T_{AB\to A'B'}(s,t)}{T_{CB\to C'B'}(s,t)} = \frac{g_{AA'}(t)}{g_{CC'}(t)} \qquad (19)$$

is independent of B, B'.

4) $\frac{d\sigma}{dt}$ is sharply peaked near t=0, and the peak becomes sharper as s increases.

5) Vacuum quantum numbers are exchanged. The intrinsic quantum numbers of beam and target remain unchanged.

6) Spin, J, and parity, P of the interacting particles may change such that

$$P_{final} = P_{initial} \cdot (-1)^{J_{final}-J_{initial}}$$

7) Particle and anti-particle cross sections become equal at large s.

A successful theory of diffraction must incorporate these observations. This has been attempted by two distinct approaches: s-channel and t-channel depending on the way one views the interaction of the incident hadrons.

Figure 1 illustrates the s-channel view. Intermediate states, i.e. s-channel resonances, occurring between the initial and final states are explicit. Unitarity relates the imaginary

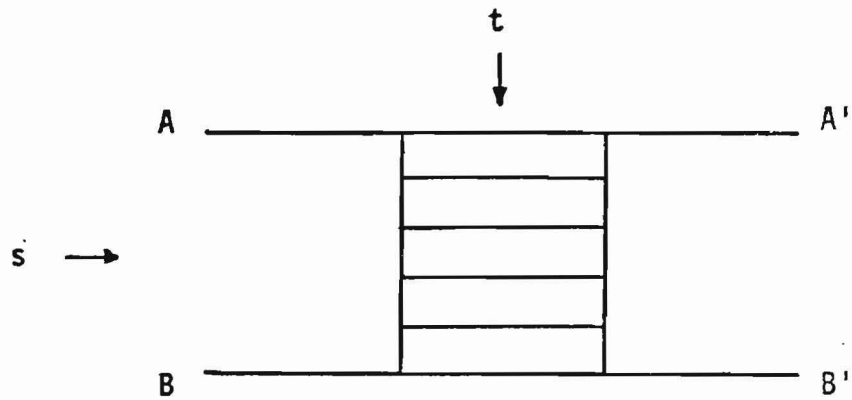

Fig. 1 s-channel view of diffractive scattering

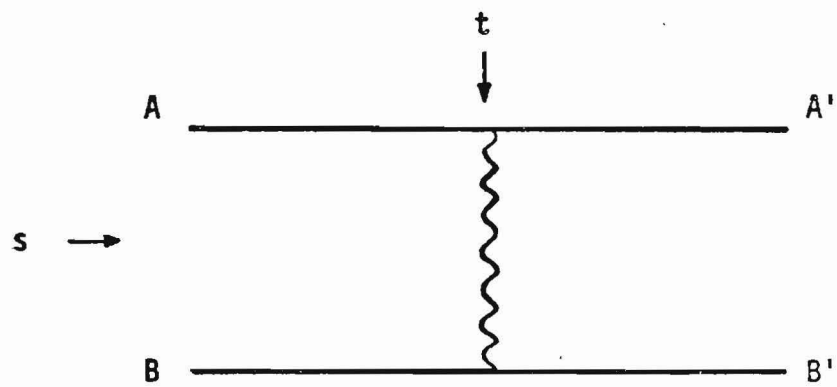

Fig. 2 t-channel view of diffractive scattering

part of the diffractive amplitude to a sum over all intermediate states:

$$\mathrm{Im}\ T_{AB \to A'B'}(s,t) = \sum_N T_{AB \to N}\, T^*_{A'B' \to N} \qquad (20)$$

The number of intermediate states is large and increases with s, leading to a very complex situation.

From the t-channel the interaction appears as the Regge exchange of an object with vacuum quantum numbers -- the Pomeron (Fig. 2). There are also complexities in this view. Multiple exchanges are possible and, a priori, just as important as a single exchange.

Abarbanel (1976) has written a comprehensive review of theoretical approaches in the s-and t-channels. The experimental properties of diffractive reactions were utilized to derive an asymptotic form for diffractive amplitudes:

$$T_{AB \to A'B'}(s,t) \underset{\substack{s \to \infty \\ t \text{ fixed}}}{\sim} is^{\alpha(t)} (\ln s)^{\beta} g_{AA'}(t) g_{BB'}(t) \qquad (21)$$

where $\alpha(t) = 1 + \alpha' t$. This is seen to account for factorization and the shrinking forward peak of $\frac{d\sigma}{dt}$. The amplitude is purely imaginary and the $\ln s$ rise of the total cross sections is built in. The Froissart bound (1961) requires $\beta < 2$ and $\alpha \leq 1$.

The theoretical challenges are to construct diffractive amplitudes which satisfy unitarity and to explain the origin of the bare Pomeron parameters involved. Low (1975) has constructed a model of the bare Pomeron in the framework of the M.I.T. bag model for hadrons. Diffractive scattering results from vector gluon exchange between confined quarks. Van Hove and Fiałkowski (1976) calculated diffractive cross sections using a model in which hadrons contain valence quarks and glue, and non-diffractive interactions are primarily due to the glue. Miettinen and Pumplin (1978) have calculated diffractive cross sections as the shadow of "soft" parton interactions (short range in rapidity). Through unitarity, the global properties of diffraction must depend on the distribution and interactions of "wee" partons only -- in particular, on fluctuations in the number of wee partons and their distributions in impact parameter and rapidity. They find the diffractive cross sections and the forward peak and slope of $\frac{d\sigma}{dt}$ are in reasonable agreement with experiment, as is the differential cross section distribution in impact parameter.

We have now a rather coherent picture of the global properties of hadron diffraction, and recent models indicate how these properties may arise from the hadron's internal constituents. One may anticipate further interesting developments, especially from quantum chromodynamics.

Certain diffractive reactions have been studied with great precision in recent years. Elastic scattering has been studied through the highest available Fermilab energies for incident beams of $\bar{p}$, p, π^-, π^+, K^-, K^+ on protons (Ayres et al. 1977). The pp elastic cross section and differential cross section $\frac{d\sigma}{dt}$ have been obtained at the ISR (Nagy, 1979). Bubble chamber experiments at Fermilab have studied missing mass distributions in events with a slow recoil proton for incident $\pi^{\pm}$ and p beams (for references, see Whitmore, 1974). High precision missing mass stuides have been performed in the Fermilab internal target area using a gas jet target, and at the ISR. The exclusive diffraction dissociation process $p \rightarrow p\ \pi^+\ \pi^-$ has been studied by Fermilab hybrid bubble chamber systems (e.g. Derrick et al. 1974a) and at the ISR (Webb et al. 1975). The exclusive process $\pi^-\ p \rightarrow \pi^-\pi^+\pi^-p$ has also been studied using the Fermilab bubble chambers (e.g. Bingham et al. 1974; Fong, et al. 1976b)

Exclusive dissociation processes involving neutral particles have not been well studied at Fermilab and ISR energies. Two notable exceptions are $p \rightarrow \Lambda\ K^+$ at the ISR (Baksay et al. 1976) and $n \rightarrow p\pi^-$ at Fermilab (Biel et al. 1976) and the ISR (DeKerret et al. 1976). Fermilab bubble chamber experiments have shown that at high energy more than half of the $\pi^{\pm}$ and p dissociation involves neutral particles, presumably π^0 's and, for proton breakup, neutrons. Kinematic fits (Day et al. 1974)

can be performed to isolate a sample of events which contain no neutrals. Knowledge of the beam momentum and energy gives a four-constraint fit, once a set of masses is assumed for the outgoing particles. Events with an overall χ^2 less than (typically) six times the number of constraints have, with high probability, no neutral particles. Successful fits for each topology (number of prongs, or charged particles, in the final state) will be labelled by prong count and number of constraints (e.g. 4P,4C for successful four-constraint fits to four prong events). The following table presents results from 147 GeV/c $\pi^- p$ interactions (Fong et al. 1974, 1976a, 1976b):

Table I

Topology	Cross Section	Leading π^- Cross Section	Leading π^- Cross Section(4C)	Leading p Cross Section	Leading p Cross Section (4C)
2 Prongs	1.80 ± .12	.79 ± .20	0.	.66 ± .11	0.
4 Prongs	4.12 ± .10	.91 ± .16	.232 ± .023	.93 ± .12	.388 ± .031
6 Prongs	4.47 ± .10	.18 ± .09	.032 ± .009	.40 ± .13	.037 ± .010

The total non-4C single-diffractive cross section is 3.18 mb (1.62 leading π; 1.56 leading p) while the total 4C diffractive cross section is only .69 mb (.26 leading π ; .43 leading p). The cross sections for leading particles were obtained by simple cuts in the single particle inclusive Feynman -x distributions.

Restricting $|x| > .96$ gives a diffractively excited mass $\lesssim 3.3$ GeV/c^2

and the 4C channels show mass enhancements in the $A_1(1100)$, $A_2(1310)$, $A_3(1640)$ regions for π excitation and in the N*(1470, N*(1520), N*(1688) regions for p excitation. It is evident from the table above that other processes must play an important role. Consider π excitation to A_1, A_2, or A_3. The decay modes have been measured to be(Barash-Schmidt et al. 1978):

$A_1^-(1100)$	$\rightarrow$	$\rho^0\pi^- \rightarrow \pi^+\pi^-\pi^-$ $\rho^-\pi^0 \rightarrow \pi^-\pi^0\pi^0$	$\sim$ 100%
$A_2^-(1310)$	$\rightarrow$	$\rho^0\pi^- \rightarrow \pi^+\pi^-\pi^-$ $\rho^-\pi^0 \rightarrow \pi^-\pi^0\pi^0$	70.3 $\pm$ 2.1%
		$\eta\pi^-$	14.4 $\pm$ 0.9 %
		$\omega_0\pi^0\pi^-$	10.6 $\pm$ 2.5 %
		K^0K^-	4.7 $\pm$ 0.5 %
$A_3^-(1640)$	$\rightarrow$	$f\pi^- \rightarrow \pi^+\pi^-\pi^-$	$\geq$ 83%

If we denote the probability of exciting a π^- into an A_1, A_2, or A_3 by a_1, a_2, a_3 respectively, the branching ratios for η and ω together with the above give:

$$\sigma(4P,4C) \rightarrow .5\,a_1 + .35a_2 + .55a_3$$

$$\sigma(4P,\text{non-}4C) \rightarrow .14a_2$$

$$\sigma(2P) \rightarrow .5\,a_1 + .51a_2 + .28a_3$$

From the 4P,4C sample (Snyder, 1975), one can estimate the values of a_1, a_2, a_3:

σA_1	~ 105 μb		a_1 ~ 210 μb
σA_2	~ 98 μb		a_2 ~ 280 μb
σA_3	~ 112 μb		a_3 ~ 202 μb
σ_{non-A_1,A_2,A_3}	~ 73 μb		

This would account for ~304 μb/660 μb of π^- excitation in the 2-prong diffractive sample and ~39 μb/542 μb in the 4-prong, non-4C diffractive events. What processes account for the majority of the diffractive events? Are the missing neutral particles π^0's or other particles?

G-parity conservation requires an odd number of pions from π-breakup. If we surmise that most beam dissociation events contain only pions in the final state, we would assume that $\pi^- \to (7\pi)^-$ states occur frequently because of the sizeable non-4C cross section in the 6-prong events ~ .36mb; however, virtually no leading protons are seen in the 8-prong events. Why would $3\pi^- 2\pi^+ 2\pi^0$ states occur but not $4\pi^- 3\pi^+$? The small 6P,4C cross section ~ 37 μb for $\pi^- \pi^+ \pi^- \pi^+ \pi^-$ also supports the hypothesis that $\pi^- \pi^+ \pi^- (\pi^0 \pi^0)$ states may not be the dominant process in 4P,non-4C diffractive π-excitation.

Similar arguments for proton diffractive excitation lead one to conclude that if N*(1470), N*(1520), N*(1688) production is dominant, then the 2-prong cross section should be considerably larger than the 4-prong. Measurements indicate the reverse is true (Barish et al. 1974; Derrick et al. 1974b).

Questions such as those discussed above motivate experimental studies of diffractively produced exclusive final states. Furthermore, no theory of diffraction can be complete without explaining why particular final states occur.

III. The Fermilab Hybrid 30-Inch Bubble Chamber Spectrometer

The spectrometer consists of the Fermilab 30" bubble chamber augmented with a system of multi-wire proportional chambers (PWC's), Cerenkov counters, and a forward-gamma detector.

The apparatus is located in the N3 hadron beam in the Neutrino Area at Fermilab. Protons from the main ring of the accelerator are delivered to a target in beam line enclosure 100, producing charged secondary beams of lower energy. No particle separation is performed: positive beams generally contain a mixture of π^+, K^+, p, and μ^+; negative beams contain the corresponding antiparticles. Particle identification is accomplished by Cerenkov mass tagging. The upstream PWC's define the trajectory of the incoming beam. Beam momentum is not measured for individual particles; the average value is computed statistically from the deflection of non-interacting beam tracks by the bubble chamber magnetic field. Momentum dispersion is small, typically ¼ to 1%, depending on collimator settings. The downstream PWC's are used for momentum determination of fast secondary particles from interacitons in the bubble chamber. The next two subsections describe the bubble chamber and the spectrometer system, with the exception of the gamma detector which is discussed in Section V.

A. Bubble Chamber

The most important single element in the Fermilab Hybrid Spectrometer is the 30-inch Hydrogen Bubble Chamber. Built by Midwestern Universities Research Association in Madison, Wisconsin, the chamber was moved to

Argonne National Laboratory in May, 1963, where the first physics pictures were taken in October, 1964. With the advent of higher energy particle beams at Fermilab, this chamber was selected as an ideal instrument for observing charged particle multiplicities, providing accurate momentum and ionization (dE/dx) measurements of the slower charged particles and angles for the fast ones.

The bubble chamber, as shown in Figures 3 and 4, is a stainless steel cylinder approximately 76cm in diameter and 38cm deep, bounded by two 10cm thick glass windows. During normal operation, the chamber is filled with liquid hydrogen at 27°K and at a vapor pressure ~ 50 psi (boiling point 20.4^{o}K). The three pistons at the top allow expansion to ~ 25 psi vapor pressure permitting the liquid to become "sensitive" to bubble nucleation and growth. One expansion and recompression of the chamber requires 20-30 msec. Beam particles enter the chamber just before maximum expansion producing tracks of bubbles suitable for photography 200-300 microns in size after a delay of 1.5 - 3 msec. Beam particles enter the chamber through a relatively small "window" of stainless steel 18.69cm X 5.56cm in area and .300cm thick. Fast particles exit through the large (75°) window of .318cm thick stainless steel, allowing a reduction of interactions in the chamber exit wall to acceptable levels (~ 5%) for the downstream hybrid system. Two 7.5^{o} wedges of magnet steel were removed from the bubble chamber magnet on the downstream side, Figure 3, to increase hybrid system acceptance. The optical system is dark field and allows four stereo views of the chamber. Each camera sits diagonally opposite an elliptical xenon flash tube. Two large condensing lenses on the flash tube side of the chamber focus light from each tube to a ring around the corresponding camera, such that

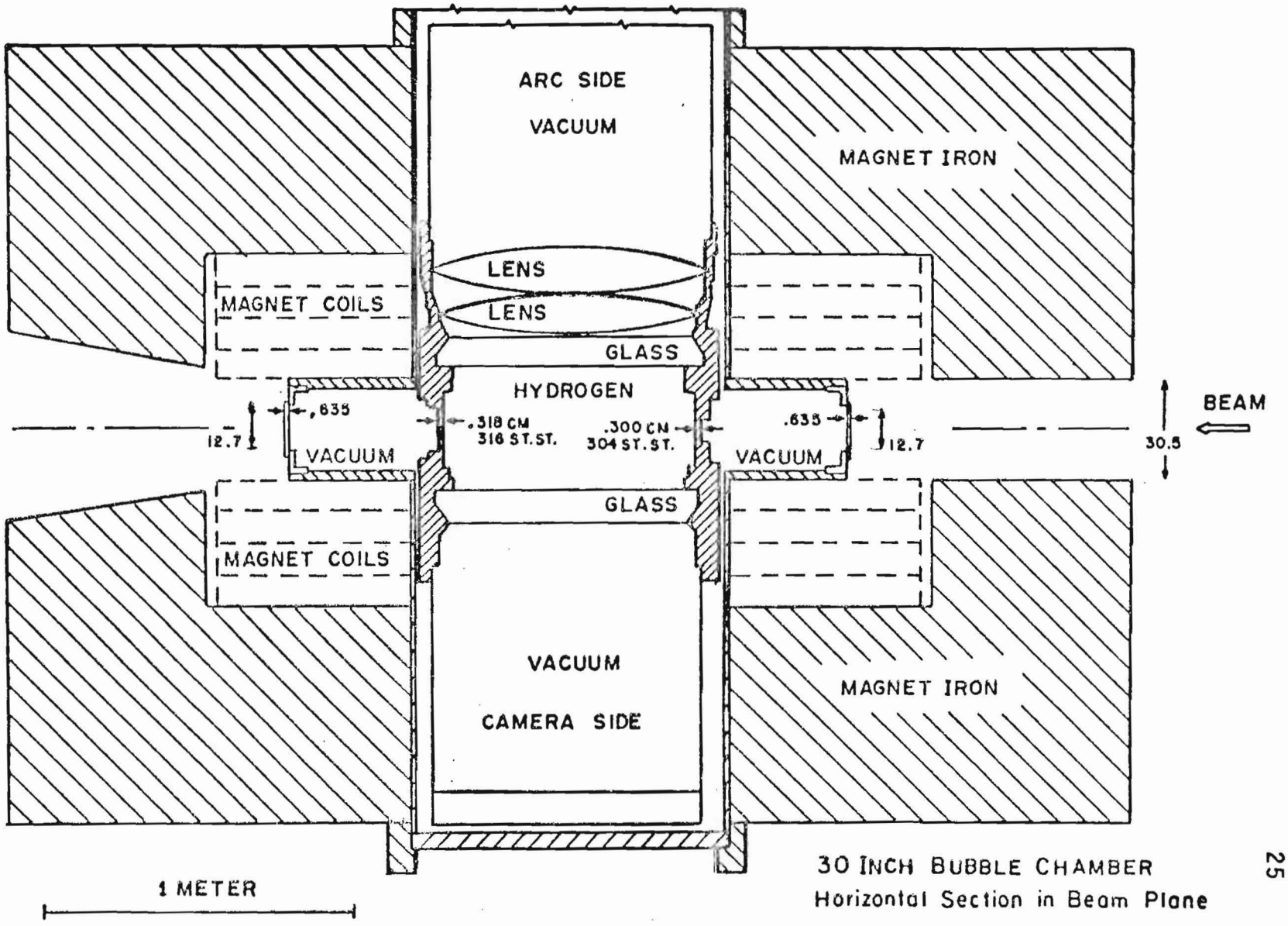

30 INCH BUBBLE CHAMBER
Horizontal Section in Beam Plane

Fig. 3.

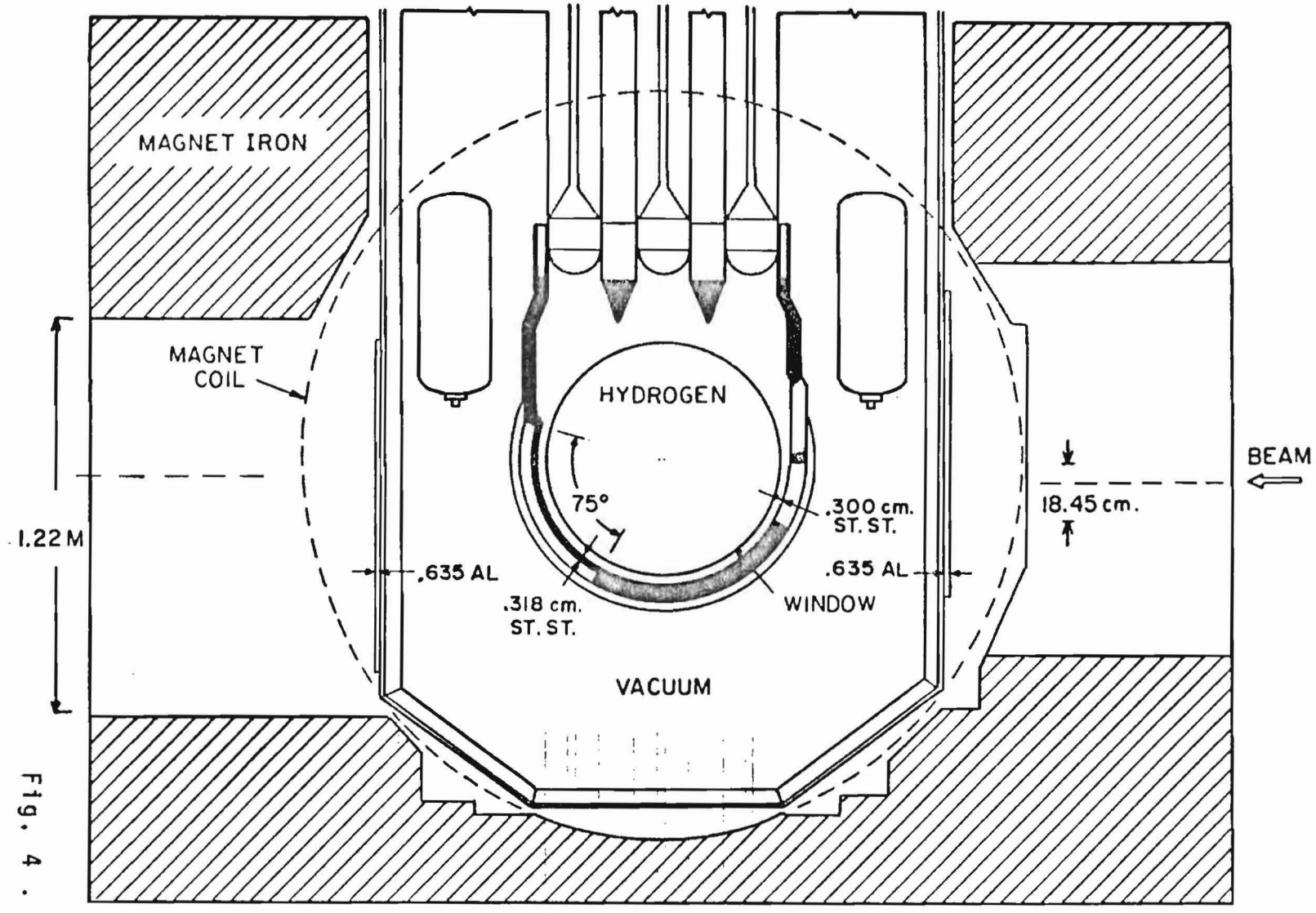

1 METER

30 INCH BUBBLE CHAMBER
Vertical Section along Chamber

Fig. 4.

no light directly enters the camera lens. Track bubbles scatter light and appear bright against a dark background. After film development, tracks appear as dark bubbles on a light field.

The camera lenses were chosen so as to minimize coma and astigmatism and are fixed focus. There are no shutters -- chamber illumination is provided by the xenon flash tubes. At present there are three 35mm Multidata cameras for camera ports (views) 1, 2, and 3. Port 4 is generally unused or equipped with a special test camera. An observation port allows direct visual inspection and can be fitted with a Polaroid camera.

Two camera views are required to reconstruct space points in the chamber from film images. A third view allows kinematic fits to be performed. To facilitate reconstruction, each of the two windows has eleven fiducial marks (crossed lines intersecting at 90°) etched into the glass at the liquid hydrogen interface. An optical survey determines spatial coordinates of each fiducial after the chamber is filled with liquid hydrogen and cooled to the operating temperature. The survey is repeated at the end of the running period, before the liquid hydrogen is dumped. These fiducial measurements and corresponding film image measurements are input to an optics program together with the refractive indices and thicknesses of the glass and hydrogen. This program calculates camera positions, film-to-lens distances, and lens-distortion parameters crucial for high precision spatial reconstruction. An average roll of 35mm film (single view) in this experiment, contained approximately 2700 frames and yielded about 600 scanned interactions.

The polarity of the bubble chamber magnet is adjusted so as to bend beam particles upwards. Maximum field is 32.5 kilogauss; however, for cost

advantage, the normal operating value is 27 kilogauss. The magnetic field, including the downstream fringe field, was mapped using Hall probes in 1973 (prior to removal of some magnet steel). The field was again mapped using search coils in August 1978, and a new parametrization is forthcoming.

B. Proportional Wire Chamber System

Figure 5 is a schematic of the principal detector elements in the spectrometer. An incident beam particle passing through the two scintillator paddles, SC 1 and SC 2, produces coincident electronic pulses which trigger a master gate of 150 nanoseconds duration. This gate is used to strobe signals from the proportional wire chambers (PWC's), Čerenkov counters, and other elements into local memory. Each of the PWC's A-G consists of three or more parallel planes of sense wires which are used to measure transverse beam displacement. A sense wire plane consists of parallel gold-plated tungsten wires with a spacing of approximately two millimeters. Sense wire planes in PWC's A, B, and C contain 48 wires each, while planes in PWC's D-G contain 156 wires each. A gas mixture of argon, carbon dioxide, and freon (80%, 19.45%, 0.55% respectively) flows through each sealed plane assembly. A sense plane is sandwiched between two parallel copper-beryllium wire planes to which negative high voltage is applied, producing gas amplification in the proportional region. A beam particle passing near a sense wire generates a current pulse which is amplified and converted to differential logic signals. Signals from all wires in the system are simultaneously transported by ribbon cable, with

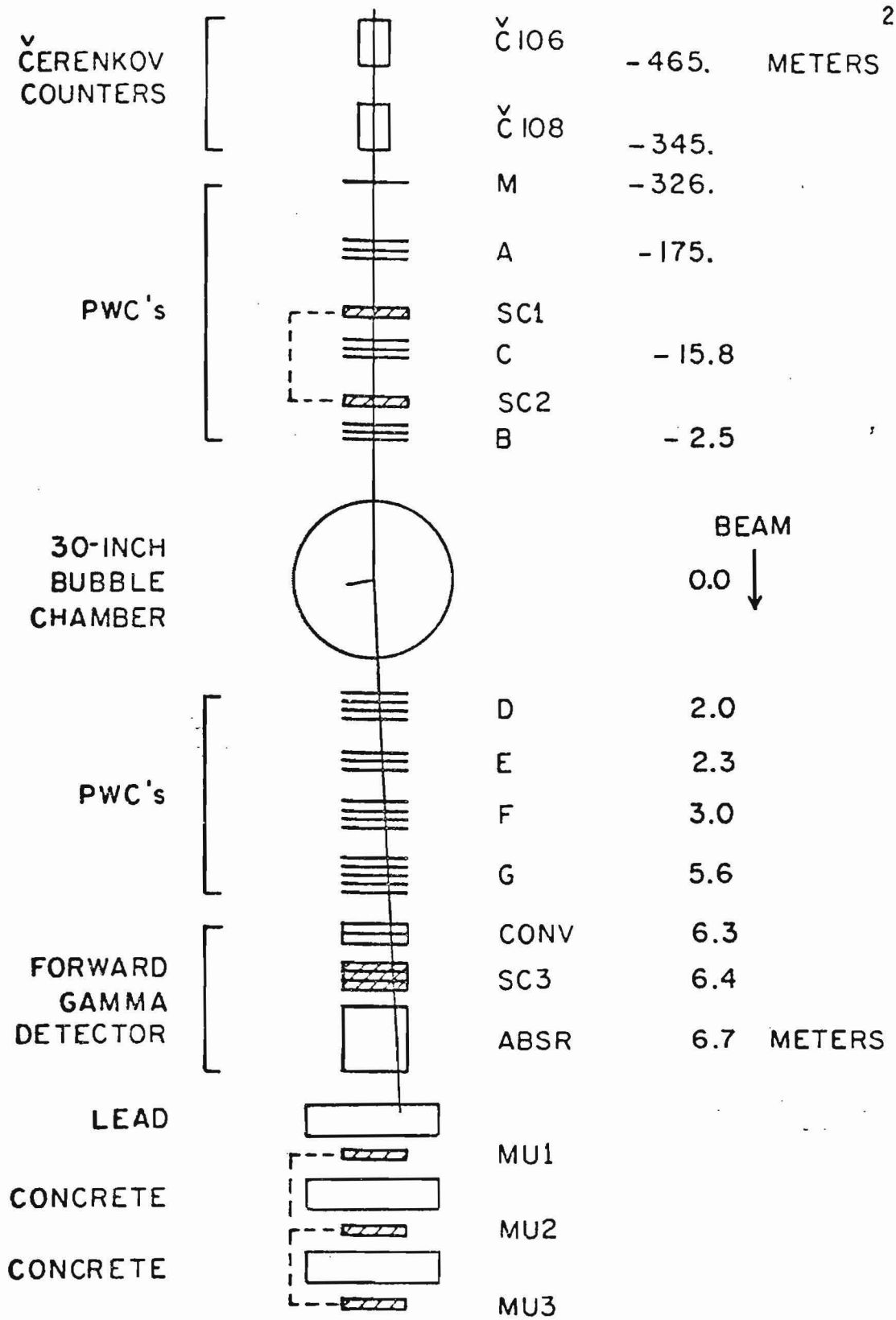

Fig. 5- FERMILAB HYBRID SYSTEM CONFIGURATION

appropriate delays, to common buffers where they may be strobed into local random access memory (RAM) by the master gate. Three of the planes in each chamber are oriented such that the wires in one plane lie at 60° angles to wires in the other two planes. This geometry greatly facilitates track reconstruction from the wire data. Chambers with more than three planes have one or more pairs of planes with parallel wires offset by half the wire spacing, to provide better spatial resolution.

It is worthwhile, at this point, to digress and explain the timing considerations involved. During this experiment, the fundamental injection-acceleration - extraction cycle of the accelerator occured every thirteen seconds. Circulating 400 GeV/c momentum protons in the main ring were extracted over a two second period in the form of eight "pings" (spills) spaced 183 milliseconds apart, each spill lasting about 250 microseconds.

Secondaries from the proton target were selected to produce a positive beam at 150 GeV/c momentum for the bubble chamber. A fast "kicker" magnet was activated during each spill after a maximum of seven secondary beam particles. An upper limit is necessary so that efficient measurement of the bubble chamber film is possible. The RAM was chosen to allow storage of associated wire data for the maximum of sixteen beam particles. During the interval between spills, the bubble chamber picture was taken and wire data was transferred from local RAM to the online PDP 11/45 computer. A parallel CAMAC system was used for the data tranfer, interfaced to the PDP 11/45 with an E.G.& G. BD011 branch driver. The PWC hardware was linked to CAMAC via two custom-built modules. While the number of "logical" PWC planes was twenty-six, not including some pseudo-planes of Čerenkov signals etc., the number of "physical" plane assignments was less than

twenty-four, allowing one CAMAC word to contain wire firing information of a given wire address for all physical planes in the system. Transfer to CAMAC could occur at a maximum rate of 250 kHz. The wire data was re-formatted and stored by the computer after each spill. At the beginning of the next accelerator cycle, separate wire data records were written onto magnetic tape for each spill. For further details of the online computer program, tape format, and read-out system, see R.K. Yamamoto, 1976.

Each Čerenkov counter (Č106 and Č108) is a helium-filled differential threshold counter. Gas pressure was adjusted to provide (separate) photo-tube signals for π and K discrimination while protons remained below threshold. Muon contamination in the beam was measured by three plastic scintillator paddles (MU1, MU2, MU3). MU3 was situated behind one meter of lead and 3.7 meters of shielding concrete. The beam composition varied somewhat during experiment E299. Cerenkov tagging results gave, typically, 30% proton, 10% kaon, 57% pion/muon, and 3% ambiguous for the data sample used in this thesis.

The acceptance of the downstream PWC system, as a function of the momentum of charged secondary particles, is shown in Figure 6.

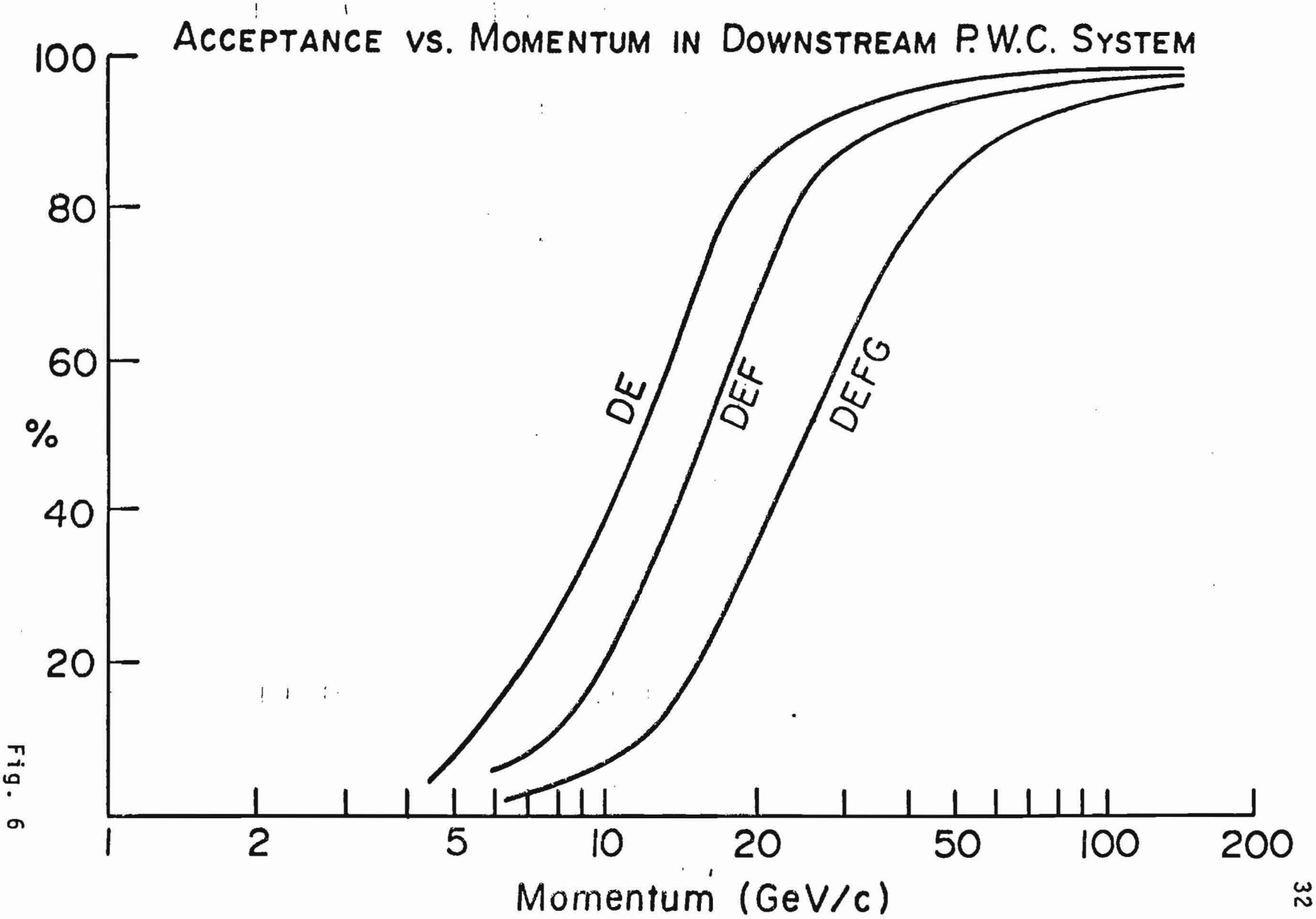
ACCEPTANCE VS. MOMENTUM IN DOWNSTREAM P.W.C. SYSTEM
100
80
60
%
40
20
DE
DEF
DEFG
1
2
5
10
20
50
100
200
Momentum (GeV/c)

Fig. 6

IV. Data Reduction and Processing

This section describes the bubble chamber film analysis and the data processing chain. Each topic will be treated in greater detail after a general description of the procedure. Figure 7 delineates the processing chain used for this experiment.

Each roll of bubble chamber film has three corresponding views which are simultaneously mounted on an Image-Plane Digitizer (IPD). This machine allows an operator to examine each frame of film in order to select events for precision measurement. An on-line PDP-8 computer writes information for each examined event into a record on magnetic tape. This record contains event identification information (roll, frame, event numbers), a reject code, a count of charged secondary tracks leaving the interaction point (prong count), and the coordinates in the film image plane of guidance points for subsequent precision measurement. A PDP-8 tape contains information from many IPD machines, each of which may be processing different experiments. Program COPY-8 sorts the IPD information on the PDP-8 tape and writes a tape containing only information for a particular experiment and roll. Program CHARON reformats the data to prepare for precision measuring;program LETHE provides an editting capability in case of errors in the original scan. The LETHE output tape provides event information to a PDP-10 computer which initiates and guides the precision measurement of the

FILM ANALYSIS AND DATA PROCESSING

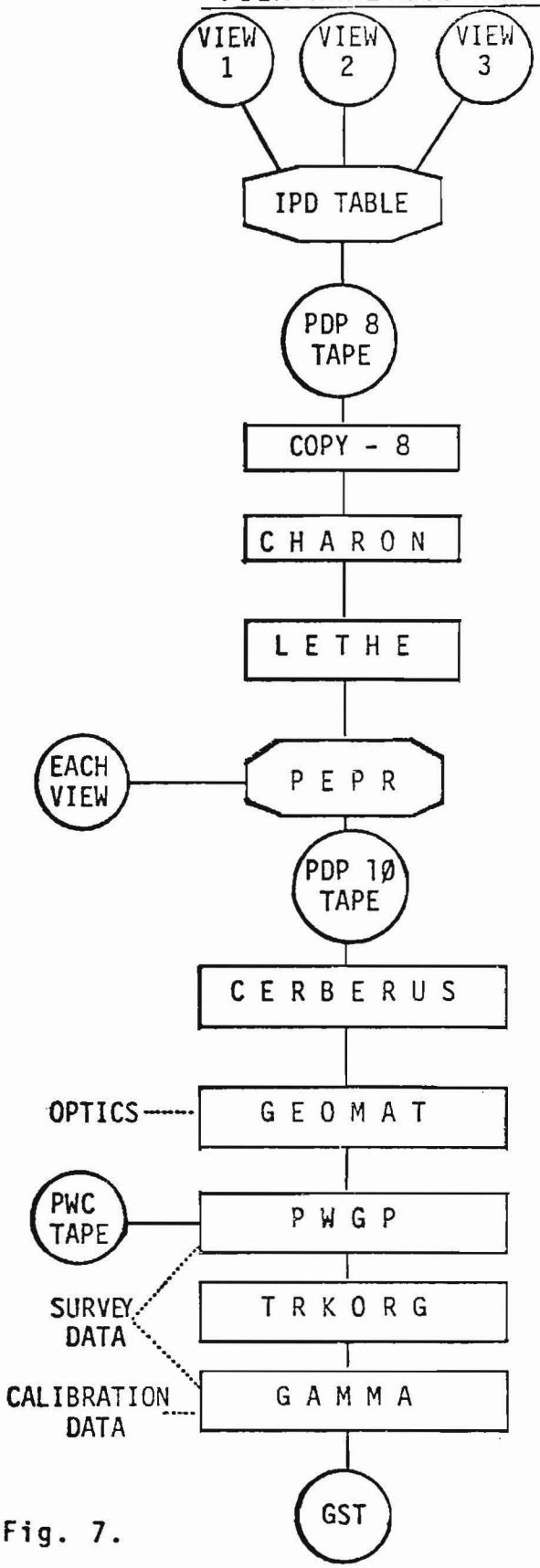

BC Film is

scanned, data is

written on tape,

sorted by roll.

Data is reformatted,

editted if necessary.

Precision measurements of tracks on film

are recorded on tape,

examined and reformatted.

BC tracks are reconstructed in space.

PWC tracks are reconstructed in the hybrid system,

matched with BC tracks, and a combined fit performed.

Forward gamma data is processed.

A Geometry Summary Tape is written.

Fig. 7.

film by PEPR (Precision Encoding and Pattern Recognition, see Pless '65). Each of the three views is measured separately. Program CERBERUS checks the measurements and reformats the data for the track reconstruction programs. Program GEOMAT reconstructs the charged particle tracks in the three-dimensional bubble chamber coordinate system using measured points from the three film views. In most cases, track curvature due to the bubble chamber magnetic field allows determination of the momentum three-vector of a particle at the interaction vertex. In some cases the mass of a particle can be deduced from the track information. Program PWGP (Proportional Wire Geometry Program) searches for the beam track associated with a bubble chamber event. A unique PWC beam track allows determination of beam particle mass from the Čerenkov data. Secondary tracks in the downstream PWC system are also reconstructed by PWGP. Program TRKORG (TRACK ORGANIZER) attempts to match secondary tracks from PWGP with bubble chamber tracks. If a match is found, then a combined fit is performed to accurately determine the track trajectory. Program GAMMA examines the FGD (Forward Gamma Detector) data to locate and determine the energy of electromagnetic showers associated with the bubble chamber interaction. Finally, a GST (Geometry Summary Tape) is written containing selected information for each event.

A. Film Scanning and Measuring

Each roll of developed film was scanned on Image-Plane Digitizers (IPD's) to select events for automatic measurement. The IPD's project one frame of bubble chamber film onto a flat white table at which the scanner is seated. Each of three views may be examined or all views superimposed. Digitization is accomplished by positioning the vertex of a projected reticule over a point to be measured and pressing a button. The projector for the reticule slides along a mechanical arm which extends across the table towards the scanner. The arm is capable of lateral motion as well. Shaft encoders allow simultaneous measurement of the Cartesian coordinates of a selected point on the image plane with a least count of 75mm. Measurements from IPD's and manual measuring machines are transmitted to an online PDP-8 computer and written on magnetic tape. Additional information is exchanged between scanner and computer via a small tabletop control console. All events within a fiducial volume in the bubble chamber were digitized except those falling into certain reject categories.

The scanning rules were defined by Hafen and Hulsizer (1977). A count of the number of charged tracks (prong count) at the beam track interaction vertex is recorded for each event, except for frame rejects (unbiased). A beam track is recognized to be a minimum-ionizing track in the fiducial volume, parallel to the beam direction to within .0025 radian. Non-beam tracks

are labelled as secondary tracks.

The reject criteria for scanning are as follows:

Frame Rejection Criteria

A) One or more views missing

B) The beam tracks have an average of fewer than 15 bubbles per mm on film.

C) More than 16 incoming beam and secondary tracks cross the front edge of the fiducial volume. Multiple crossings of a single track are not counted.

D) More than two events lie in the fiducial volume.

Event Rejection Criteria

A) A secondary scatter is visible less than 225 um on film from the primary vertex in any view.

B) More than two beam tracks, not associated with the event, lie within 90 microns on film of the event's beam track.

IPD points for each view of an accepted event must include fiducials #13 and #22, the primary vertex, a point in a "clear" region on the beam track, and two points on a reference beam track for PEPR's ionization measurement. At least two points are digitzed for each track originating at the primary vertex: 1) an end point which is either the last track point visible in the bubble chamber or the point where the track has turned by 120°, and 2) a clear point between the vertex and the end point which is in a region as clear as possible of other tracks

and film obstructions. Up to eight points may be digitized.

Slow proton scatters where the recoil, if visible, is less than 135 microns and all secondary tracks from decay vertices (odd prongs) are also digitzed. Vee's from decays of neutral particles and electron-positron pairs from gamma conversions are digitized with the associated event. A Vee or gamma which points back to more than one primary vertex is digitized with both events, and a bit is set in the scanner comment word to flag the ambiguity. Tracks which end in the chamber are labelled "stopping" tracks. A charged track is said to be a "one prong decay" if a kink is present where the track direction changes by more than 2° and/or the ionization is observed to change. If such a track is positive and has high bubble density it is labelled a "proton kink" if the ionization does not change. The distinctive π-μ -e decays are also given a separate label. An electron or positron is identified if the track has minimum ionization and is observed to spiral in by at least 180°. Dalitz pairs (electron-positron pairs at the primary vertex) must have one or both tracks identified as electron or positron.

If a secondary vertex is not seen in one or two views, then the end point is not labelled a vertex, and the track identifier word is set to the corresponding value for that vertex type. (Table II)

After the initial scan and IPD of each roll, a check and correction scan is performed. A second scanner is given only a

TABLE II

VERTEX TYPES

1	Primary Vertex
2	Secondary Interaction Vertex
3	V vertex
4	One prong decay vertex
5	Straight gamma vertex
6	Curly gamma vertex
7	Proton kink vertex
8	End of stopping pi track that decays into a muon and then an electron
9	Dalitz electron pair at primary vertex
10	Stopping track end point
11	Short stopping track
12	Three pronged decay vertex

list of frames and asked to record independently the number of events and the topology of each. This scan is then compared with the original, the differences are resolved, and the IPD output tape is corrected if necessary.

In addition to the check and correction scan, a second scan was made of every fourth roll according to the same rules, but with no IPD measurements. This allows the efficiency of the original scan to be determined.

The pre-measurement programs COPY-8, CHARON, and LETHE will not be further discussed, since their primary function is data handling.

The PEPR measurement system was conceived and developed at M.I.T. in the mid-1960's, and it is now used in a number of high energy physics laboratories around the world (Pless 1965). Briefly, it is a computer-controlled, semi-automatic measurement system capable of locating tracks and digitizing coordinates of points along the trajectories. The output tape from program LETHE is read by the computer, and event information is used to automatically position the film at the proper frame for PEPR measurement. During the measurement procedure, the film is clamped in the optical path between a cathode ray tube (CRT) and a photomultiplier. The computer issues commands to the PEPR controller based on the guidance points from the LETHE tape. The CRT electron beam is positioned appropriately, and the desired area of film is scanned by the spot of light on the CRT

face. Intensity variation of the light reaching the photomultiplier allows, together with a knowledge of the scan pattern, the measurement of points along track segments on film. Fiducial marks on the film corresponding to known coordinates in the bubble chamber are also measured to allow subsequent spatial reconstruction of the interaction. The frame is rejected when less than seven fiducials can be measured.

At Fermilab energies, previous PEPR measurement techniques for low energy interactions were found to be inadequate. Bubble chamber pictures often contained many close, straight tracks requiring more precise angle measurement, noise filtering, and careful handling of intersecting tracks. PEPR now uses a spot scan consisting of a series of about sixty sweeps at intervals along a line segment approximating the track element (Andersson and Pless, 1975). Track elements can be measured with this procedure to a precision of 0.4 micron and 0.2 degree. As many as twenty-five elements, each characterized by an x-coordinate, a y-coordinate, and an angle, may be measured along each track.

Program CERBERUS checks the PEPR measurements in each view for various failures, such as too few measured points on a track, insufficient fiducial measurements, points out of order and missing vertices or tracks. The data is then merged and organized into the appropriate format for track reconstruction (Warshaw, 1978).

B. Track Reconstruction

The measurement of one film view provides coordinate pairs for points along each charged track associated with the event of interest. Non-corresponding points in the three views must be used to obtain the trajectory of the charged particle in space. This is done by GEOMAT, a program written by Francis Bruyant and Elizabeth Hafen (1975). The trajectory of each particle is parametrized as a helix in the magnetic field of the bubble chamber. Energy loss in the liquid hydrogen is negligible only for particles having more than a few GeV of energy. This reduces the radius of the helix as a function of path length from the vertex (increases the radius for the incoming beam track). The vertex position is determined as the intersection point of the trajectory fits.

The spatial locations of the fiducials are necessary for track reconstruction. These were determined by optical survey of the bubble chamber under (static) operating conditions, before and after the experiment. Camera locations in space and optical distortion parameters (lens distortion, film stretch) were determined by program PYTHYD (Trepagnier, 1975), which uses film measurements of the fiducials and the optical survey data. For this purpose, all fiducials visible in each view are measured several times on a few selected frames of film. Camera locations, fiducial locations, and optical distortion parameters were grouped as "OPTICS" in Figure 7.

Program PWGP uses the GEOMAT vertex to locate the PWC beam track associated with a bubble chamber event, and then reconstructs secondary tracks in the downstream wire chambers. PWGP was written by T.L. Watts, T.C. Ou, T. Ludlam, and D. Fong. As described in Section III-B, PWC data is grouped according to the arrival times of the beam particles during a beam spill; once the correct "time slot"is known, Čerenkov beam-tagging information and downstream wire data are available. Track location and reconstruction proceeds in several steps. First, possible track intersection points are identified in each PWC. There are at least three planes in each chamber which are oriented at 60° relative angles, and the wires in each plane are numbered sequentially from a plane edge. A track at normal incidence passing through the three planes gives three wire firings such that the wire numbers add up to a constant value regardless of the intersection point. A small tilt correction is used for tracks not at normal incidence. The next step is to search for associated points in a contiguous set of chambers. Since the magnetic field axis lies approximately in the horizontal plane and perpendicular to the beam direction, charged particles are primarily bent either up or down, depending on the charge. The net result is that the trajectories would appear as straight lines pointing to the vertex if the wire chamber hits could be viewed from above. Each "triple" of wire hits in the PWC farthest from the bubble chamber is extrapolated to the event vertex. If the wire planes along this path contain nearby

hits, the corresponding set of adjacent triples is assumed to define a particle trajectory. A linear fit to the wire hits gives four parameters: $y(x_p)$, $z(x_p)$, $\frac{dy}{dx}\Big|_{x_p}$, $\frac{dz}{dx}\Big|_{x_p}$ for the track. The particle momentum and charge are determined by swimming the downstream track back to the vertex (effective impact parameter). Documentation for PWGP has been written (Napier, 1977).

The location and orientation of each wire plane are required for track reconstruction by PWGP. The relative orientation of the planes in a PWC was fixed when the chamber was assembled. A survey of PWC locations determined the beamline coordinate and an orientation angle for each plane. The remaining parameters, transverse displacements of the centers of all planes, were determined statistically from fits to non-interacting beam tracks (bubble chamber magnet off). This was done by program SURVEY (Bugg, 1974a,b) SURVEY was also used to determine the average beam momentum from non-interacting beam tracks measured with the magnet on. Program FITROT (Bugg, 1974a,b) determined the transformation parameters which map the PWC coordinates into bubble chamber coordinates and vice versa.

TRACK ORGANIZER is a program which attempts to match tracks from PWGP with bubble chamber tracks reconstructed by GEOMAT. This program was written by Douglas Fong (documentation: Brau, 1977). The PWC downstream tracks are extrapolated through

the bubble chamber magnetic field to the vertex, and then projected into each of the three film views. Track image points from PEPR (IPD points when PEPR measurement failed) of the fast bubble chamber tracks and of the GEOMAT reconstruction failures are stored by GEOMAT for TRACK ORGANIZER. These images are compared with the projected PWGP track. When a match is found, a combined fit is performed using the image points in all three views and the parameters of the downstream track fit from PWGP. Tracks are classified according to their reconstruction status:

MULT	INTERPRETATION
-2	DOWNSTREAM TRACK MATCHES UNUSED FILM IMAGES
-1	DOWNSTREAM TRACK MATCHES RECONSTRUCTED GEOMAT TRACK
0	UNMATCHED DOWNSTREAM TRACK
1	DOUBTFUL GEOMAT MATCH
2	TWO-VIEW GEOMAT RECONSTRUCTION
3	THREE-VIEW GEOMAT RECONSTRUCTION

A GEOMAT track match is considered doubtful when the PWGP track matches with one or two images, but not all, used in the GEOMAT reconstruction. In this case, the GEOMAT track is labelled MULT 1 and a combined fit is made to the downstream track and the matching images.

Hybridized tracks have much more reliable momenta and angles than bare bubble chamber tracks. A track reconstructed in downstream chambers D, E, F, G has angular error ~ .17 milliradian compared to typical errors of the order of one milliradian in the bubble chamber. Momentum resolution for 147 GeV/c beam tracks has been determined to be:

$$\frac{\Delta p}{p} \cong .06\ p\ \%$$

This is also consistent with the momentum spread observed from elastic scattering. Bare bubble chamber momentum resolution for beam tracks is $\frac{\Delta p}{p} \sim 50\%$.

The GAMMA program will be explained in detail in Section V-B. The remainder of this section describes the data format at the end of the track reconstruction chain. Each event may have three associated types of records: 1) a GEOMAT format record, 2) a SQUAW record, used for subsequent kinematic fits to specific reactions, and 3) a GAMMA record, containing the ADC data associated with the event and the GAMMA program results. The first record on each tape is an identification record (type zero) which contains version numbers of the reconstruction programs used to produce the tape.

The GEOMAT record format (Morecroft, 1978) consists of six blocks: 1) the header block contains event identification

and measurement status, 2) the space point block contains the label, type, and location of each vertex in the event, 3) the GEOMAT track block contains track identification and reconstruction information including the particle momenta and angles at the track end points plus associated errors, 4) the track image block contains measured PEPR points, or IPD points, for the fast GEOMAT tracks and for those images not successfully matched by GEOMAT, 5) the PWGP track block contains downstream track identification and results of the trajectory fit, 6) the TRACK ORGANIZER block contains track information, hybridized if possible, for each track in the GEOMAT and PWGP blocks.

The SQUAW records were not used for the present analysis, and their format will not be described. The GAMMA (type 3) record format will be discussed in Section V-B.

C. Data Sample

The data used for the present analysis consists of interactions form 36 rolls of film. All rolls were measured by PEPR: 11 at M.I.T., 17 at Rutgers University, and 8 at Johns Hopkins University. Table III provides a comparison of data from these different measurements. No significant bias was found, however, track ionization was not measured initially at Rutgers. Ionization information from M.I.T. and John Hopkins

University was processed using subroutines PWGION (Ljung, 1974), and HOPION (Bachman, 1978). Measurement of the recoil proton is crucial for identification of target diffractive scattering events; the procedure adopted to identify slow protons in the Rutgers' data sample is described in the Appendix. Topological cross sections have been obtained for a considerably larger data sample than the one used for this analysis. Tables IV and V give the calculated prong cross sections for π^+-proton and proton-proton interactions from approximately 140,000 pictures (Brucker, 1978).

Three types of biased rejects deserve special mention. The first is an event reject, type 99, which occurs during GEOMAT processing when the necessary computer memory exceeds the maximum available to the program. The second event reject, type 888, occurs when more than fifteen minutes of computer time are necessary for GEOMAT processing of the event. These rejects may be reprocessed in the future, if the amount of computer time necessary is not prohibitively large. Figure 8 shows the percentage of reject 99's as a function of prong count. One may expect the number of reject 99's should increase roughly as the cube of the number of fast secondaries, since this reject results from too many three-view match possibilities.

The third type of event reject is due to incomplete measurement, or to misidentification of the charge of a track. Such events are labelled incomplete, or not charge-balanced.

TABLE III

EVENT SUMMARY

	Rutgers	M.I.T.	Johns Hopkins
Total Events Scanned	10623	7609	4796
Scan Rejects	2527	1927	1218
PEPR Rejects	0	4	1
GEOMAT Rejects:			
Reject 99	475	278	97
Reject 888	14	2	2
No Vertex	506	135	162
PWGP Rejects:			
No time slot	705	462	297
Other	93	50	28
Total Non-Rejects	6303	4750	2991

TABLE IV

Topological Cross Sections in pp Interactions at 147 GeV/c

Number of charged prongs	Number of events seen	Corrected number of events	Cross Section, mb
2	2149	2964.6	10.49 ± 0.23
	elastic	1978.3	7.00 ± 0.34
	inelastic	986.2	3.49 ± 0.21
4	1572	1777.6	6.29 ± 0.16
6	1770	1965.4	6.95 ± 0.17
8	1451	1634.6	5.78 ± 0.15
10	1000	1188.3	4.20 ± 0.13
12	593	750.9	2.66 ± 0.11
14	239	348.7	1.23 ± 0.08
16	113	189.8	0.67 ± 0.05
18	33	67.2	0.24 ± 0.03
20	10	24.6	0.87 ± 0.018
22	-	6.3	0.022± 0.009
24	1	1.1	0.004± 0.004
TOTAL	8931	10919.0	38.62

TABLE V

Topological Cross Sections in π^+p Interactions at 147 GeV/c

Number of charged prongs	Number of events seen	Corrected number of events	Cross section, mb
2	1938	2693.4	5.03 ± 0.13
	elastic	1783.3	3.33 ± 0.14
	inelastic	910.1	1.70 ± 0.08
4	1737	1951.2	3.64 ± 0.09
6	2040	2246.3	4.19 ± 0.09
8	1897	2149.9	4.01 ± 0.09
10	1338	1574.8	2.94 ± 0.08
12	755	971.2	1.81 ± 0.07
14	348	486.6	0.91 ± 0.05
16	145	233.8	0.44 ± 0.04
18	42	74.6	0.14 ± 0.02
20	12	25.8	0.048± 0.014
22	5	8.2	0.015± 0.007
TOTAL	10257	12415.8	23.17 ± 0.23

Figure 9 gives the percentage of complete, charge-balanced events as a function of prong count. The decrease is approximately linear with prong count. Weights were used to produce correct cross sections when inclusive distributions were drawn only from the sample of complete and charge-balanced events.

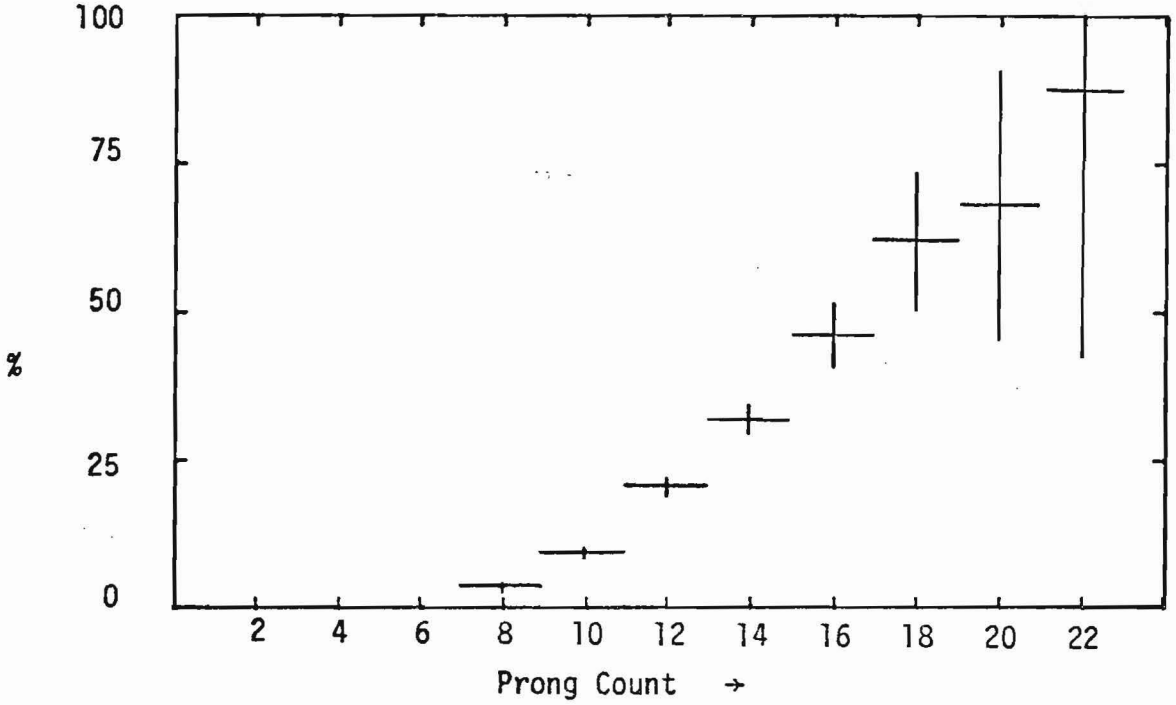

Fig. 8 - Reject 99 Events by Topology.

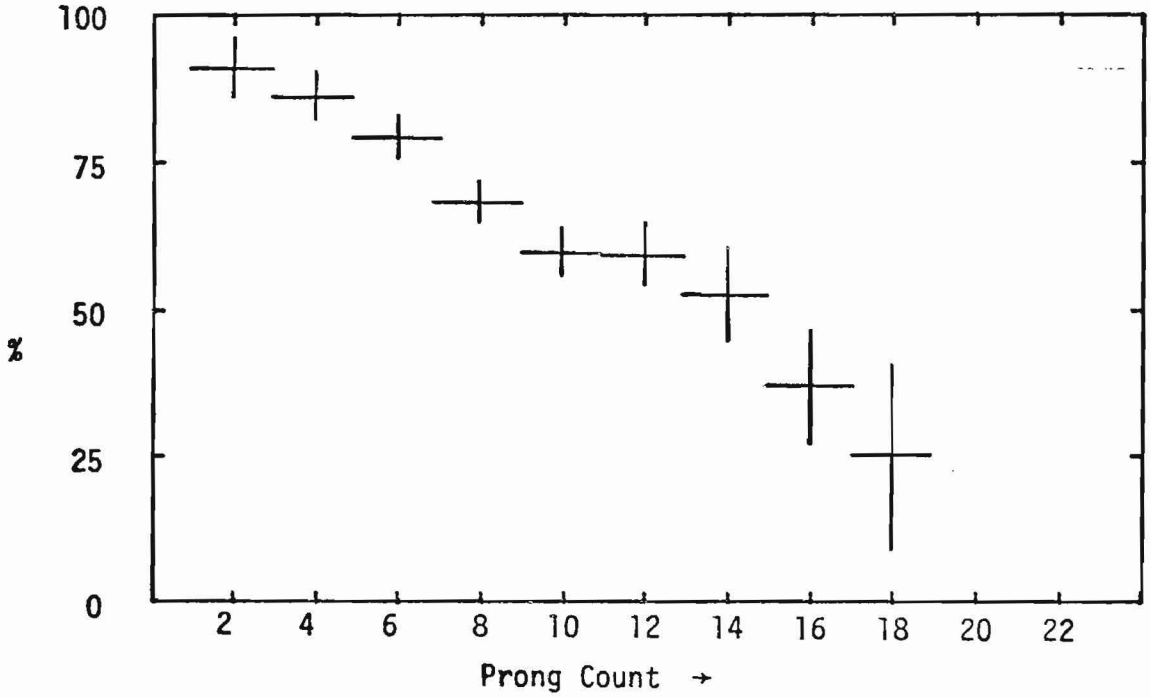

Fig. 9 - Successful Events which were Complete and Charge-Balanced

V. Gamma Detector

The gamma detector used in this experiment is a prototype of a large detector to be used in the Fermilab Hybrid Spectrometer. Initial plans for the detector resulted from collaboration of the Proportional Hybrid System Consortium (PHSC) with high energy groups from Padova, Rome, and Trieste, who were designing an external gamma detector to be used with BEBC at the CERN SPS (Bettini, et al. 1975).

Fiugre 10 is a schematic of the active elements in the detector. Two layers of five lead glass bars of type F-2, 76.2 x 6.35 x 6.35 cm^3, are used to initiate an electromagnetic shower. Each bar is wrapped with aluminized mylar to channel the Čerenkov light from electrons and positrons in the shower toward a photomultiplier tupe at the end of the bar. A clear silicone resin wafer provides optical contact between the glass and an AMPEREX 56AVP photomultiplier. The entire converter assembly was mounted in a light-tight wooden box. Three planes of plastic scintillator fingers of type NE100, 1.5cm wide and 1cm thick, sample the transverse shower profile. Lucite light guides connect the the scintillator to inexpensive RCA phototubes of type 931A (Fig. 11). A Lucite head on each light guide serves to focus the light on the side-view photomultiplier window. Finally four large lead glass blocks of type SF-5, 15 x 15 x 60 cm^3, absorb the bulk of the shower. The absorber blocks were wrapped in aluminized mylar, stacked on a

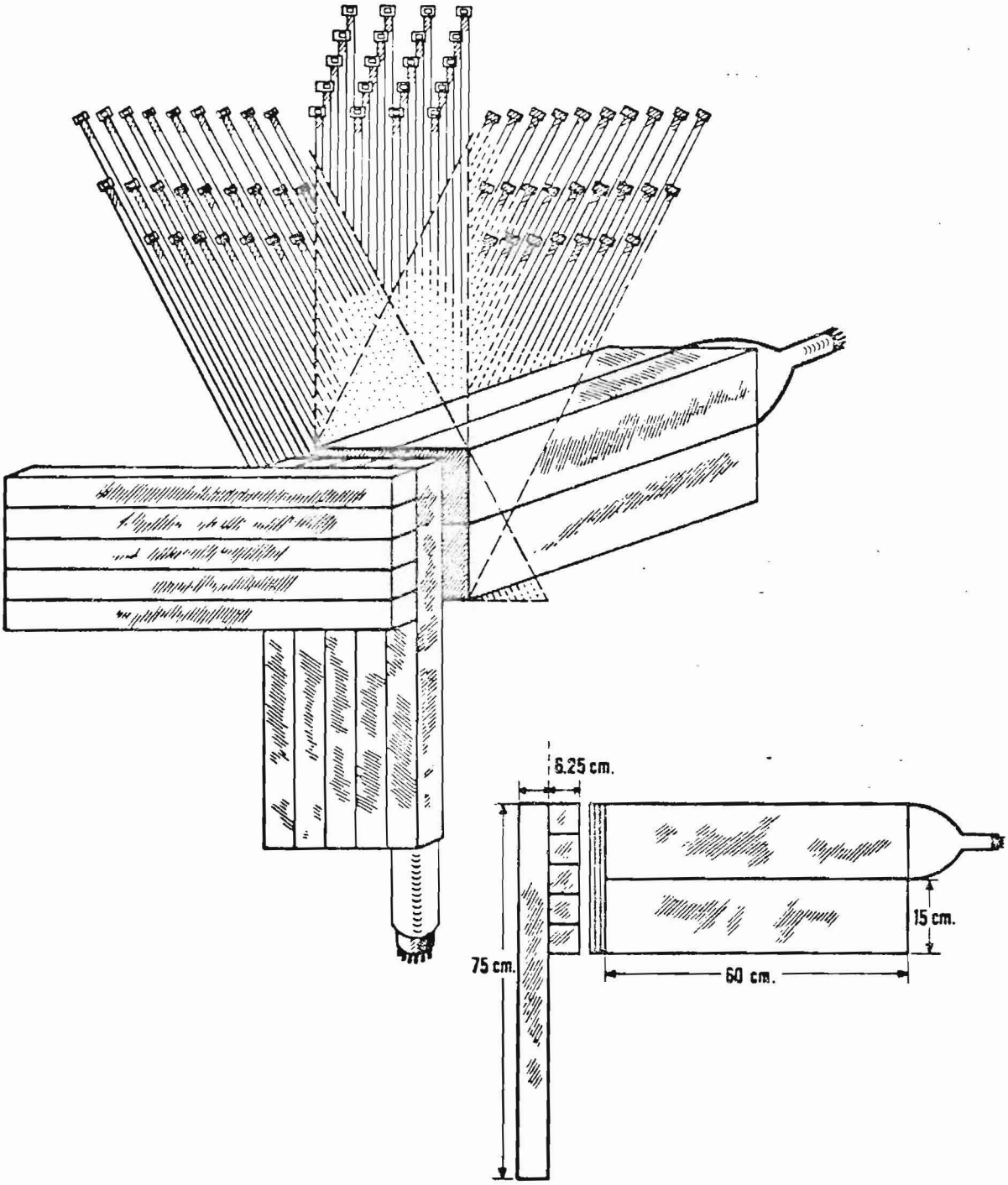

Fig. 10

Fig. 11 - Light pipes and phototube mounts in the scintillator hodoscope.

supporting table, and shrouded with black felt. Five-inch EMI 9530R photomultipliers, coated with optical grease, were spring loaded against the blocks. The converter bars provide four radiation lengths of lead glass in front of the scintillator hodoscope; the absorber blocks supply an additional twenty-five radiation lengths.

Photomultiplier signals are carried by individual coaxial cables to Lecroy 2250Q buffered analog-to-digital converters (ADC's). The ADC's provide nine bit precision according to the formula:

$$Q = aN^2 + bN + c$$

where Q is the integrated PM signal charge, and N is the corresponding number of counts. a, b, c are coefficients supplied by the manufacturer for each unit. A pedestal value, calculated by the same formula, must be subtracted to obtain the true charge from the photomultiplier. Signals were integrated during a 450 nanosecond gate and then digitized during the following nine microseconds. In the next microsecond, the digital count is stored in a first-in, first-out buffer which has a capacity of thirty-two words. ADC data for beam particles arriving during a spill were stored until the end of the spill and then read out to the online computer using direct memory access. During the long ADC dead time following a beam master gate, other beam particles may enter the bubble chamber. Since PWC data is stored for all beam tracks in the spill, approximately

one of every four beam tracks has no ADC data. A second CAMAC system, distinct from that for the PWC hardware, linked the ADC system to the PDP 11/45 computer. Data for all spills in an accelerator cycle accumulated in a buffer until end of the cycle, at which time a single gamma detector data record was written onto magnetic tape. This preceeded the PWC data records for the individual spills.

A. Stability and Calibration

An electromagnetic shower detector should be limited primarily by the statistical process of shower development. The total Čerenkov light deposited in the lead glass by a shower is directly proportional to the energy of the incident particle. An ideal photomultiplier (PM) produces an output current response which is 1) a linear function of the total incident Čerenkov light, and 2) stable against time variation.

The response of each PM was monitored periodically using a light flash calibration system. Figure 12 shows a schematic of the setup used for the lead glass blocks. The flash unit consists of a hydrogen thyratron tube and flash driver (Kerns, 1975) designed to deliver highly reproducible ($\sim$1%) light pulses of intensity and duration comparable to pulses from electromagnetic showers.

Light from the flash lamp is carried by fiber optic light guides to the face of each lead glass block opposite the PM. The stability of the flash is also checked using a reference PM

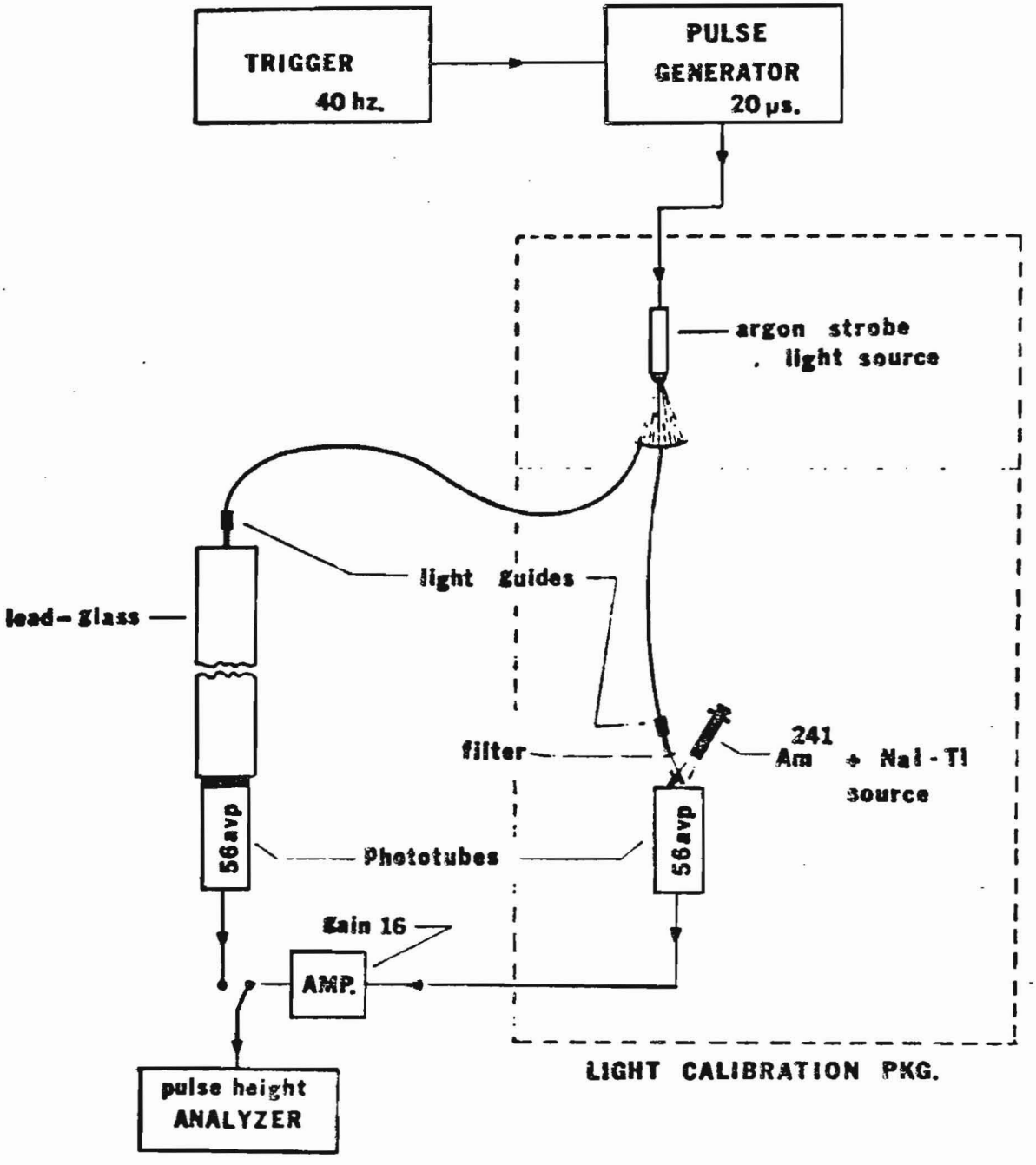
TRIGGER
40 hz.
PULSE
GENERATOR
20 μs.
argon strobe
light source
light guides
lead-glass
filter
241
Am + NaI-Tl
source
56avp
Phototubes
56avp
Gain 16
AMP.
pulse height
ANALYZER
LIGHT CALIBRATION PKG.

Fig. 12

which views both a light guide from the flash lamp and a NaI (Tl) scintillator doped with radioactive Am^{241}. A neutral filter attenuated the flash lamp signal at the reference tube to provide PM response comparable to that from the scintillator source. Two separate flash lamps and fiber optic systems were used, one for the converter lead glass bars and one for the absorber lead glass blocks. Both lamps were synchronously driven by the same flash driver at a maximum rate of 30 Hz.

Figure 13 illustrates the calibration flash system for each plane of the scintillator hodoscope. Uniform PM response within each plane is necessary to insure accurate position determination of the shower center. A flash of pink light from a Krytron (E.G. & G. KN22) illuminates a piece of plastic scintillator producing a flash of scintillation light which travels down the tapered lucite bar at the base of the hodoscope. A band of white paint on the bottom edge of the bar reflects light into the hodoscope fingers. The white coating and the shape of the bar were experimentally designed for uniform light delivery to each finger. The variation was found to be less than 2%.

The lead glass converter assembly was designed, constructed and tested at M.I.T. (Bober and Frank, 1976). The flash lamp drift was observed to be constant to ± 1 channel over time periods of four to five hours. Scintillation light from the Am^{241} source was used to eliminate the photomultiplier drift. In

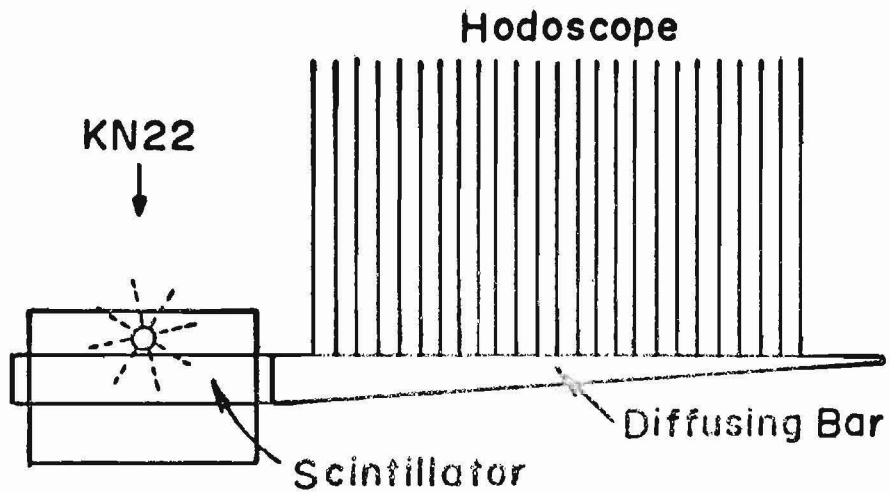

Schematic of Light Calibration System for Hodoscope

Fig. 13

thirteen trials the phototube drift was found to be $\leq$ 1.76 counts or 0.77%.

The complete detector, consisting of converter, scintillator hodoscope, and absorber, was tested using tagged electrons in the Fermilab N-5 beam line in March, 1976. Exposures were made at nominal beam energies of 30, 40, 50, 60, 75 and 100 GeV. A proportional wire chamber in front of the detector allowed determination of the point of incidence of a charged particle to an accuracy of approximately two millimeters. Results of these tests have been published (Heller et al. 1978) and only a brief summary will be presented here.

Calibration of the detector is accomplished when the mathematical function is determined which relates the energy deposited in an element to the measured PM signal. Neglecting non-linear PM response and energy losses due to the geometry of the detector, the total energy of a shower is just the sum of the energies deposited in the lead glass blocks:

$$E_i = \sum_{j=1}^{14} \alpha_j C_{ij}$$

where E_i is the energy (GeV) of the shower i, C_{ij} is the PM signal (picoCoulombs) for the element j resulting from the shower i, and α_j is the unknown energy coefficient for element j. During the tests, the electron beam was dispersed over an area of 10 cm horizontally by 6 cm vertically to allow determination of coefficients for several adjacent blocks during a given

run. In addition, the entire detector and PWC could be moved vertically or horizontally in order to expose any desired point of the detector to the maximum beam intensity. The energy E_i is taken to be equal to the momentum of the incident electron. Momentum dispersion was such that $(\Delta p/p) \sim 1\%$. High statistics data taken at 50 GeV beam energy were used to determine the α_j by minimizing χ^2:

$$\chi^2 = \sum_i \left(E_i - \sum_{j=1}^{14} \alpha_j C_{ij}\right)^2$$

These values were then used to calculate shower energy for runs taken at the other beam energies.

A typical 50 GeV electron shower deposits 5-20% of the total energy in the converter (Fig. 14) and the rest in the absorber (Fig. 15). The distribution of total shower energy is shown in Figure 16. The tail of the curve is due to hadron showers which deposited sufficient energy to trigger the detector. A gaussian fit to the electron peak gave an energy resolution of 3.5% full width at half maximum (FWHM) for 50 GeV showers.

Figure 17 displays the averages of the measured shower energy distributions as a function of the known beam energy. The detector is found to be linear to within 1% accuracy for electron showers of energy 25-100 GeV. The resolution, expressed as the FWHM of the electron peak, is shown in Figure 18 as a function of beam energy. The statistical nature of the shower

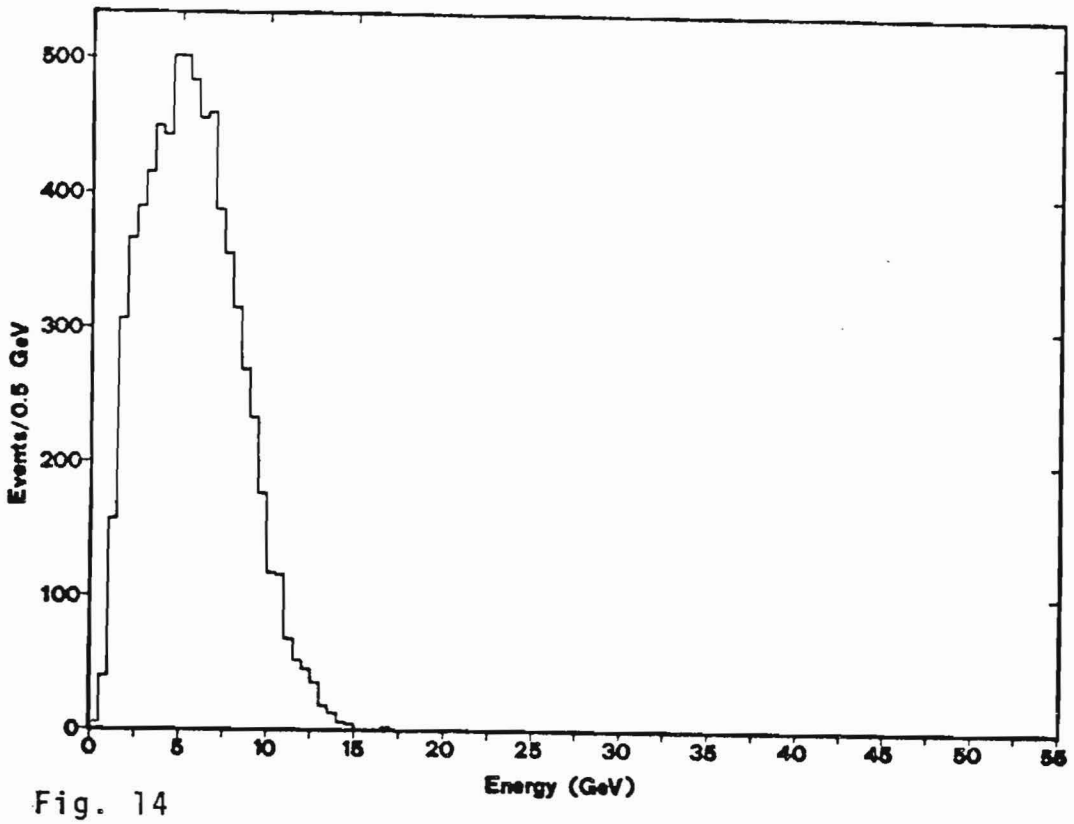
Events/0.5 GeV
Energy (GeV)
0
100
200
300
400
500
0
5
10
15
20
25
30
35
40
45
50
55

Fig. 14

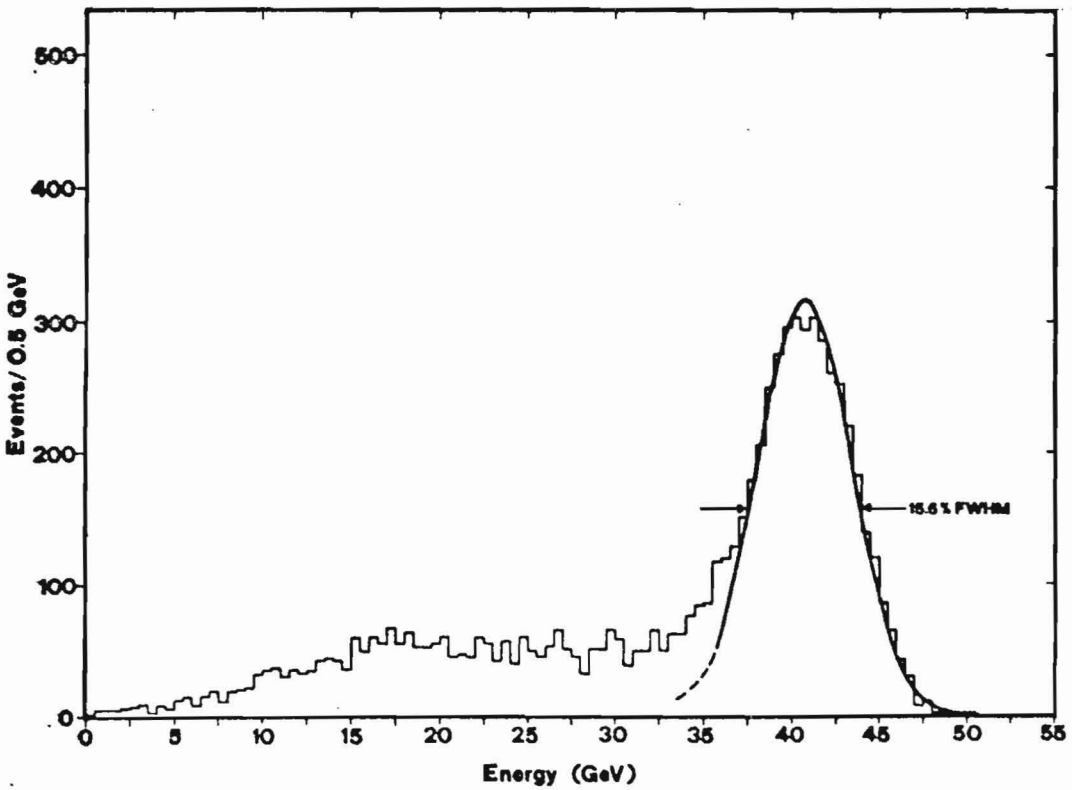
Events/0.5 GeV
Energy (GeV)
15.6% FWHM
0
100
200
300
400
500
0
5
10
15
20
25
30
35
40
45
50
55

Fig. 15

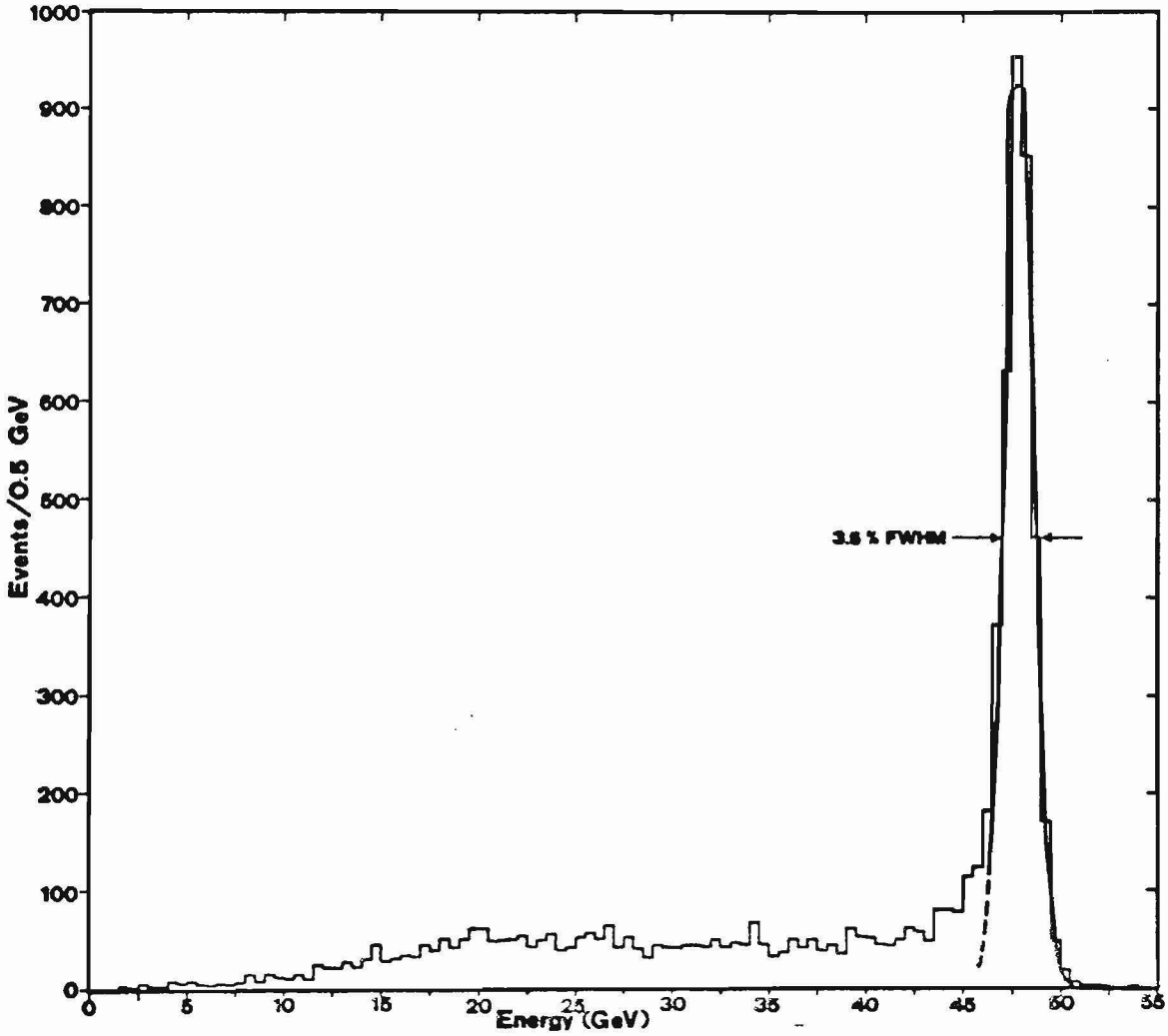
1000
900
800
700
600
500
400
300
200
100
0
Events/0.5 GeV
3.6 % FWHM
0
5
10
15
20
25
30
35
40
45
50
55
Energy (GeV)

Fig. 16

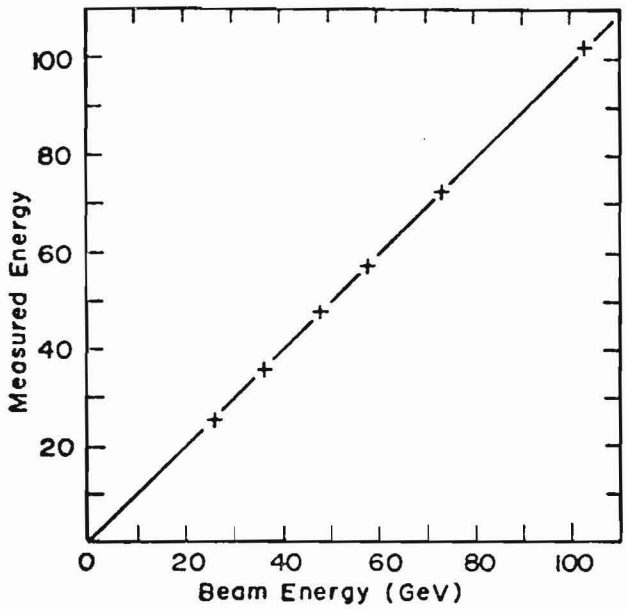
Measured Energy
100
80
60
40
20
0
20
40
60
80
100
Beam Energy (GeV)

Fig. 17

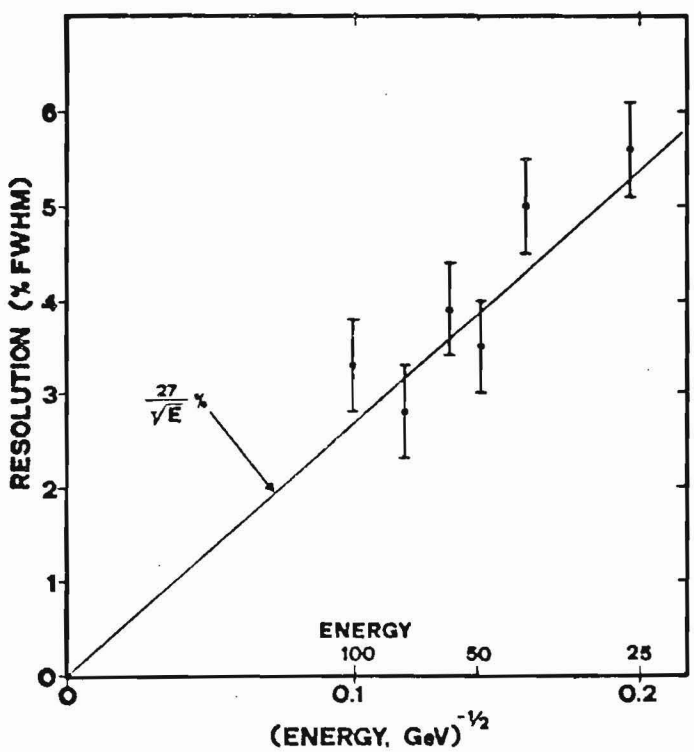
RESOLUTION (% FWHM)
6
5
4
3
2
1
0
27/√E %
ENERGY
100
50
25
0
0.1
0.2
(ENERGY, GeV)^-½

Fig. 18

energy determination implies that $\Delta E \sim \sqrt{E}$. The result was:

$$\frac{\Delta E}{E} \text{ (FWHM)} = \frac{27 \pm 2}{\sqrt{E}} \%$$

where E is the electron energy in GeV.

The scintillator hodoscope provides a sampling of the transverse shower development across a plane in the detector near the depth of maximum shower intensity. A histogram of the signals from a shower in one scintillator plane is characteristically peaked with nearly exponential decrease on both sides of the peak. Figure 19 was generated by superimposing the centers of many electron shower histograms for a single scintillator plane. The result is well described by an exponential decrease in intensity with increasing distance from the shower center. A coordinate can be determined for each of the scintillator planes by forming the weighted average of the PM signals:

$$U_i = \sum_{j=1}^{N} j \cdot C_{ij} \Big/ \sum_{j=1}^{N} C_{ij}$$

where U_i is the coordinate of the center of shower i, j is the scintillator finger number, C_{ij} is the PM signal from finger j due to shower i, and N is the number of fingers used to form an average for the plane. The width of the fingers is roughly comparable to the half-width of a 50 GeV shower ($\cong$ 1.2 cm).

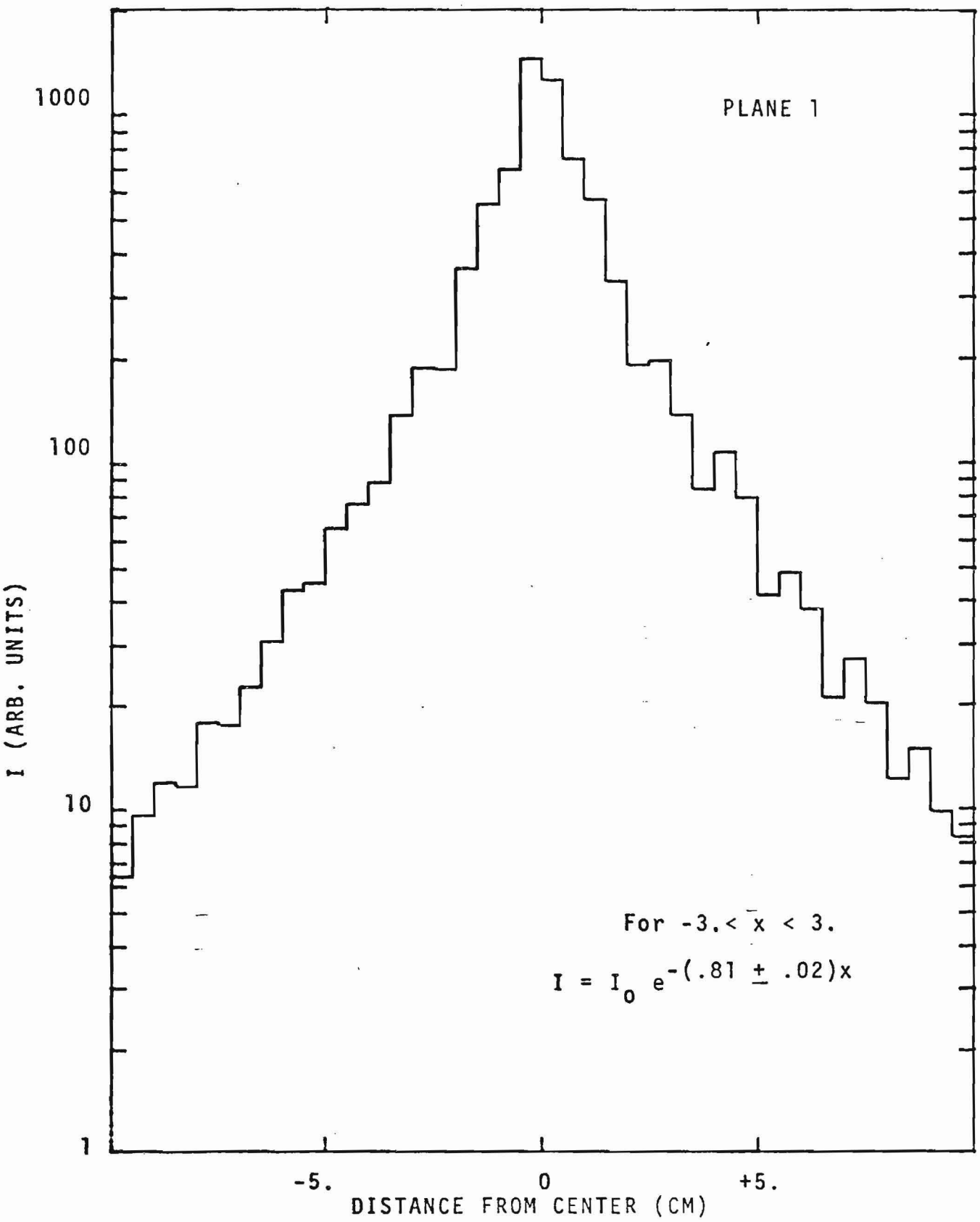
PLANE 1
1000
100
10
1
I (ARB. UNITS)
For -3.< x < 3.
I = I0 e-(.81 ± .02)x
-5.
0
+5.
DISTANCE FROM CENTER (CM)

Fig. 19

This introduces a non-negligible systematic error in the coordinate average (Bushnin et al. 1973, Bushnin et al. 1974), which is approximately given by:

$$\Delta U = .075 \sin \left[\frac{2\pi}{w} (U - U_0) \right]$$

where w is the finger width (=1.5cm) and U_0 is the coordinate of the center of the finger in which U lies. This correction was applied to hodoscope data from the tests. By histogramming the difference between the PWC coordinates and the coordinates determined from the scintillator hodoscope, the spatial resolution in each plane was found to be σ = 1.4mm.

B. Gamma Detector Data Processing

Output tapes from TRACK ORGANIZER were processed by program GAMMA (Napier, 1979) to locate electromagnetic showers in the forward gamma detector and determine the two production angles and energy of each shower. As the tape is read,each GEOMAT format (type 1) record is examined and the following blocks are stored: header, space point block, and TRACK ORGANIZER block. If a matching ADC data (type 3) record occurs before the next type 1 record, subroutine PROCES is called to initiate and steer subsequent processing of this event. Three tests must be passed before shower location is attempted: 1) the event must have source code 110, indicating

that the event was successfully processed by PWGP and TRACK ORGANIZER, 2) the ADC multiple flag must be clear (a set multiple flag indicates more than one beam track triggered the PWC system during the ADC gate ~450 nsec), and 3) the energy deposited in the converter blocks must exceed 500 MeV. The last test bypasses the shower location logic for events having minimal signals in the hodoscope, eliminating unnecessary computation.

Gammas which lose very little energy in the converter are undetected. This problem will be discussed in greater detail in a subsequent section; however, it should be noted that the fraction of gammas which do not convert in the converter layers is $e^{-12.70/3.22} = .019$.

Due to the proximity of the gamma detector to the bubble chamber, and to the absence of a downstream sweeping magnet, hadrons from the primary or secondary interactions provide a serious background for electromagnetic shower detection. A subroutine, EXTRK, is called by PROCES to extrapolate charged tracks in the downstream PWC system to the x-coordinate of the forward gamma detector. If a track intersects the converter, track information is stored for later indicative print, and slopes and intercepts are rotated to the PWC coordinate system for extrapolation through the various components of the gamma detector. EXTRK calls subroutine FINGER to locate the fingers in the three hodoscope planes through which the track passes. This information is convenient for detailed checking of events

with questionable fits (i.e. high χ^2 for the hodoscope fit or final energy fit).

Subroutine PROJEC determines which lead glass blocks should contain an electromagnetic shower, if one is associated with the track. This information is needed to evaluate the signal contribution due to hadronic showers in the detector. A matrix N_{ij} is found for each block i and track j:

N_{ij} =	0	block i not used for shower j. i = 1, 14 elements j = 1, total tracks
	1	block i receives more energy from shower j than any other block in its layer.
	2	secondmost important block in layer for this shower.
	•	
	•	
	•	

The three layers considered are the converter layers (1,2) and the absorber blocks (3). A second array M_i stores the number of showers which overlap in a given block (i). The first three bits of a "nature" word for each shower indicate whether a shower is separable from all others in this layer.

The ADC data for all channels are unpacked mext, converted to picoCoulombs and pedestal counts are subtracted. Pedestals are determined for each roll of film by a separate program which reads the PWC data tape directly. An average pedestal count is computed for each ADC channel using the no-signal events

from the flash system calibration data taken between accelerator cycles. Coefficients for each lead glass element, determined from the positron calibration runs, are used to convert these signals to GeV. Data from the hodoscope fingers remain in picoCoulombs. These signals represent a negligible contribution to the shower energy, and are used only to determine the number of showers in the detector and the transverse coordinates (Y,Z) at the hodoscope X-coordinate for each shower center.

High voltage to each photomultiplier (PM) in the hodoscope was adjusted for uniform response to a given signal in each of the three hodoscope planes. However, relative gains were quite different for the three planes. These gains were normalized statistically from the positron calibration runs. The program also keeps running averages and errors of these gains.

Subroutine FISH ascertains the number of showers in the scintillator hodoscope and performs a fit for the (Y,Z) coordinates of each shower. This crucial process will be described in detail in the next section. The vertex coordinates for the event are used together with FISH results to calculate a trajectory for each shower. These trajectories are extrapolated through the detector by subroutine PROJEC to determine the relevant blocks and check for overlapping showers as done previously for charged tracks. Subroutine ESUM uses this information to get a minimum and maximum energy for each shower. A

rough estimate of the energy for shower i is taken to be:

$$(E_{est})_i = \sum_{j=1}^{14} \min(E_j, E_k) \cdot N_{ji} / |N_{ji}|$$

where E_k is the energy of the component k associated with shower i having maximum energy for a given layer, and N_{ji} is the matrix determined in PROJEC. The maximum energy is a sum of all contributing blocks for the shower; the minimum energy is the sum of all non-overlapping blocks contributing to the shower. These energy values will be inaccurate if hadrons deposit a significant amount of energy in the absorber blocks.

Subroutine PREF is called to set up a final fit for the energy of each shower. This is not always possible, since the absorber blocks provide only four independent measurements. This fit uses a transverse shower distribution function obtained from the positron calibration data together with shower position information from FISH to predict the energy distribution in the absorber blocks.

Each pair of showers is examined by subroutine PAIR, and determined to be separable or non-separable from all other showers in each of the three layers for a given event. A nature word is provided for each pair as well as each individual shower. Three bits are reserved to indicate overlap in the three layers of blocks. A maximum energy and a minimum energy are calculated for each pair analogously to the single shower calculation. In

addition the "opening angle" at the event vertex is computed for the pair. This may be compared with the minimum opening angle of two gammas from π^0 or η decay. Showers within a square of $\pm$ one finger width of a charged track are flagged as possible hadronic showers.

Showers entering an absorber block which is intersected by the trajectory of a non-showering charged track are also flagged. Some electron-positron pairs from gamma conversions in the bubble chamber exit window are identified as two charged tracks in the downstream PWC system having a common dip angle. Showers associated with such tracks are flagged appropriately. The nature word assigned to each pair of showers contains the logical-OR of the above words for the individual showers. Pairs consistent with a π^0 or η^0 hypothesis are flagged by setting respective bits in the pair nature word. At energies $E_{\pi^0} \gtrsim 50$ GeV/c^2, the showers from $\pi^0 \rightarrow 2\gamma$ decays are most often not resolved in the detector. When a shower has energy $\gtrsim$ 50 GeV/c^2, it is considered as a possible pair, and the π^0 bit may be set in the (single) shower nature word.

Finally, an expanded type 3 record containing fit results is written on the output tape following the type 1 and type 2 records for the event. Figure 20 shows the principal subroutines called for event processing.

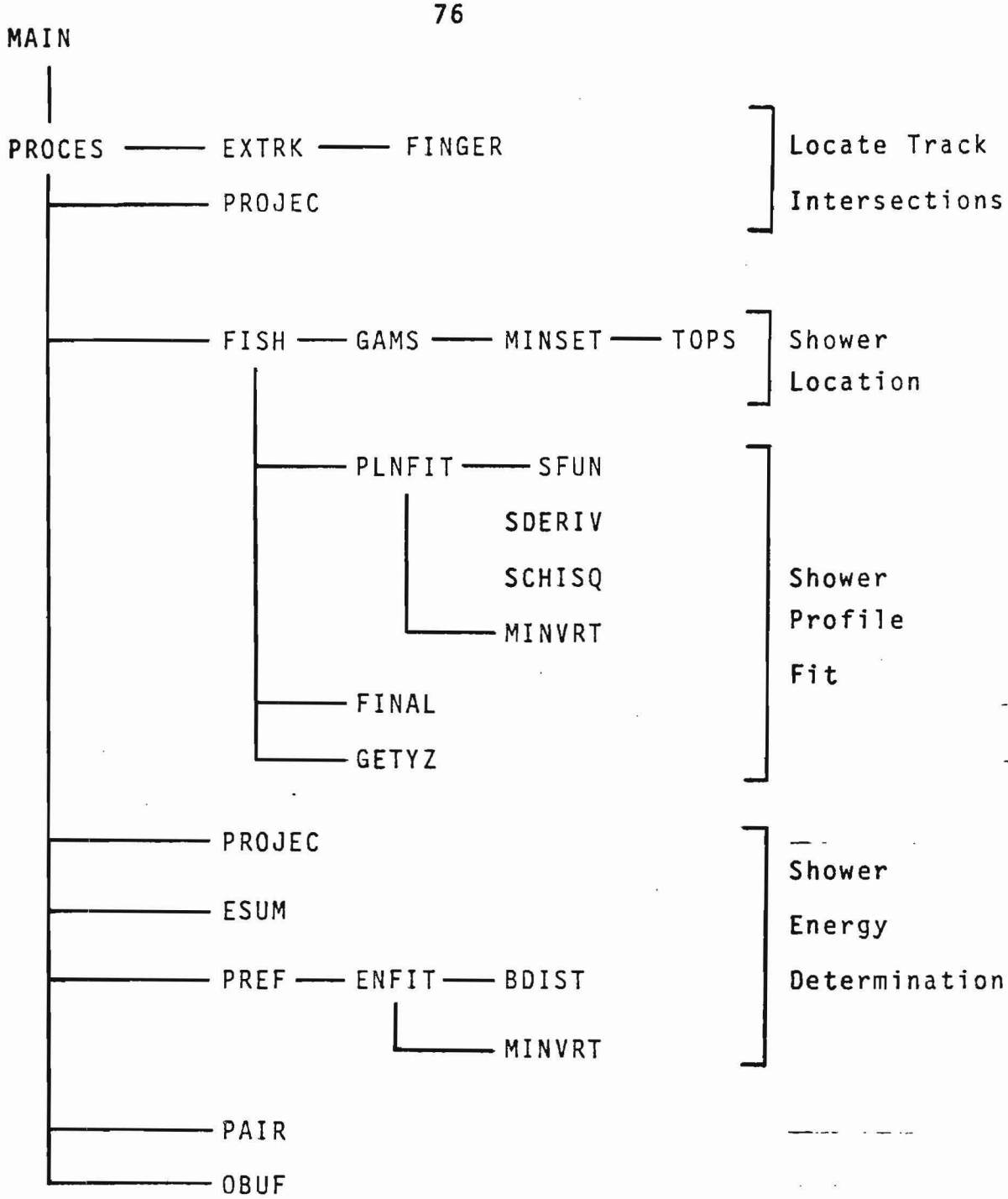

Fig. 20 GAMMA Event Processing Sequence

1. Shower Location

The number of showers in the scintillator hodoscope and their approximate locations are determined by subroutine GAMS. Each of the three hodoscope planes is examined for local maxima in the signal intensity from the finger photomultipliers. A threshold of 2-3 times the signal from a minimum-ionizing particle is used.

Each maximum (channel number) is stored along with its associated full width at half maximum (FWHM), the signal in the peak channel, and the approximate integrated signal intensity. The relevant signals are then averaged to determine more accurate coordinates for the center of each maximum in each of the three planes:

$$X_j^{(k)} = \left(\sum_i i\, S_{ij}\right) \Big/ \left(\sum_i S_{ij}\right)$$

where: k= plane number, i= finger number, j= number of maximum, S_{ij} = 0 if finger i does not contribute to shower j, otherwise S_{ij} = signal intensity (above pedestal) for finger i.

Each maximum has an associated set of triples. A triple is a set of 3 maxima, one from each plane. Each shower will be defined as a unique triple. The redundancy afforded by three scintillator planes is employed to eliminate triples which are physically impossible. The condition placed on the coordinates of a corresponding point in the three planes is:

$$D_j = X_j^{(2)} - X_j^{(1)} + 2(\cos\alpha)\cdot X_j^{(3)}\cdot f = 0$$

where α is the angle between plane 1 (or 2) and the vertical. The fraction, f, takes into account the different finger width in plane 3. Due to error in the knowledge of (X_1, X_2, X_3), D is calculated for $(X_1 \pm \Delta X_1, X_2 \pm \Delta X_2, X_3 \pm \Delta X_3)$ where ΔX_k is the width associated with a given maximum in plane k. If there exists no corresponding point in the above intervals, the triple is discarded. All physical triples are stored up to a certain limit (25). If a larger number is found, the threshold is increased in all planes and the maximum search repeated until the number of triples falls below this limit.

Subroutine MINSET enumerates all minimal sets of triples. A minimal set is a smallest set of triples which accounts for all maxima in all planes. The correct interpretation of the hodoscope data is assumed to be such a minimal set. If the fit performed by subroutine FISH is unsatisfactory, however, an additional shower may be added later.

Subroutine TOPS is called by MINSET to choose the "optimum" minimal set. A triple having an isolated maximum in one or more planes allows an estimate of the intensity of the (assumed) shower. When such estimates can be obtained for all triples, a set estimator can be calculated as the sum of the squared differences between the prediction and the integrated signal intensity of each maximum (also stored by GAMS). TOPS orders each minimal set so that the triple having largest intensity in each minimal set is stored first.

The final function of GAMS is to calculate (for each triple in the chosen minimal set) Y,Z coordinates at the X coordinate of the scintillator hodoscope.

2. Shower Profile Fit

When subroutine GAMS locates one or more showers from the scintillator hodoscope data, subroutine FISH attempts a joint fit to the signal intensities in the three planes. Each shower is parametrized as an exponential in each plane:

$$f_{ij} = g\, A_j e^{-b_j |x_i - x_{cj}|}$$

where:

i = channel number in this plane

j = shower number

g = overall normalization for given plane

x_i = center of finger i

x_{cj} = center of shower j

The initial values of the four parameters required for each shower fit are taken as:

1) Intensity - Signal in maximum finger for first plane.
2) Slope - 1.25 (taken from e^+ calibration fits).
3) U coordinate - distance from origin of plane 1 to maximum finger.
4) V coordinate - distance from origin of plane 2 to maximum finger.

The fit is done iteratively for ten iterations or until the change in all parameters is less than 1%.

If the final χ^2 of the fit is greater than a limit (1.25 at present), other minimal sets are used to attempt a fit. Up to five minimal sets are tried (best set estimators first) before the program exits. If any set meets the χ^2 criterion, it was usually found to be in the five "best" sets.

If χ^2 is still too high after the minimal sets are exhausted (or limit of 5), the program searches for triples among the residuals from the fit to the minimal set with lowest χ^2. If new triples are found, the largest of these is used as an additional shower in the fit. If none are found, the program adds a triple near the old triple with largest residuals.

Finally, the overall fit is examined. Shower fits with insufficient integrated intensity or with too small slope are discarded. Two showers with centers lying within one finger width in all planes are reduced to one shower. The χ^2 is computed for the reduced number of showers and, if too high, the fit is repeated using the reduced set of showers.

The output from FISH consists of the number of showers (possibly greater or lesser than the number from GAMS), and four parameters for each shower: intensity, slope, Y coordinate at hodoscope, Z coordinate at hodoscope. Associated errors on the four parameters are also calculated.

3. Energy Fit

Electromagnetic showers deposit the major portion of their energy in the absorber blocks of the detector for showers > 10 GeV. Four blocks impose a limit of four showers in the detector if individual shower energies are desired. Let the fraction of shower j contained in block i be denoted $f_i(x_j, y_j)$ where x_j, y_j are the coordinates of the shower center at the front face of the absorber blocks (with the center taken as origin). The signal in block i is given by:

$$S_i = \sum_{j=1}^{N} f_i(x_j, y_j)\, a_j \qquad \begin{array}{l} i = 1,4 \text{ blocks} \\ j = 1,N \text{ showers} \end{array}$$

where a_j is the intensity of shower j.

Let the measured signals in the absorber blocks be denoted Q_i and we minimize:

$$\chi^2 = \sum_{i=1} (Q_i - S_i)^2 = \sum_{i=1}^{4} \left[Q_i - \sum_{j=1}^{N} a_j\, f_i\,(x_j, y_j) \right]^2$$

This gives:

$$\sum_{i=1}^{4} Q_i\, f_i\,(x_k, y_k) = \sum_{j=1}^{N} a_j \left[\sum_{i=1}^{4} f_i(x_k, y_k)\, f_i(x_j, y_j) \right]$$

Defining:

$$F_k \equiv \sum_{j=1}^{N} a_j\, A_{kj}$$

we obtain:

$$a_j = \sum_{k=1}^{N} (A^{-1})_{jk} F_k$$

This is the solution for the energy deposited by shower j in the detector. The fit will be meaningful only if there are $\leq$ 4 showers and if the showers are well-separated enough so that each block does not completely contain two or more of the showers.

In order to proceed, the transverse shower profile integrated over depth in the absorber must be known. The scintillator hodoscope provides a measure of this at the front absorber face, but the longitudinal development is not sampled. We assume a reasonable form for $f_j(x,y)$ is:

$$f_i(x,y) = \int_{\text{block } i} Ae^{-\tilde{b}|\, r(x,y)\,|} da$$

where x,y are coordinates of the shower center at the absorber face and r indicates the transverse profile is purely radial (neglecting fluctuations). The exponential form is consistent with our hodoscope data and with other results (Bushnin et al. 1973, 1974). In addition, detailed Monte Carlo calculations have given exponential transverse shapes with longitudinal dependence $\sim te^{-ct}$ where t is depth in the absorber. Our calibration data at 50 GeV/c was used to determine $\tilde{b} \approx 0.9\ \text{cm}^{-1}$.

The most serious difficulty in analyzing the gamma detector data proved to be the background due to hadron interactions in the lead glass. The energy deposited in the detector by 147 GeV/c π^+ is shown in Figure 21. Approximately 20% of the

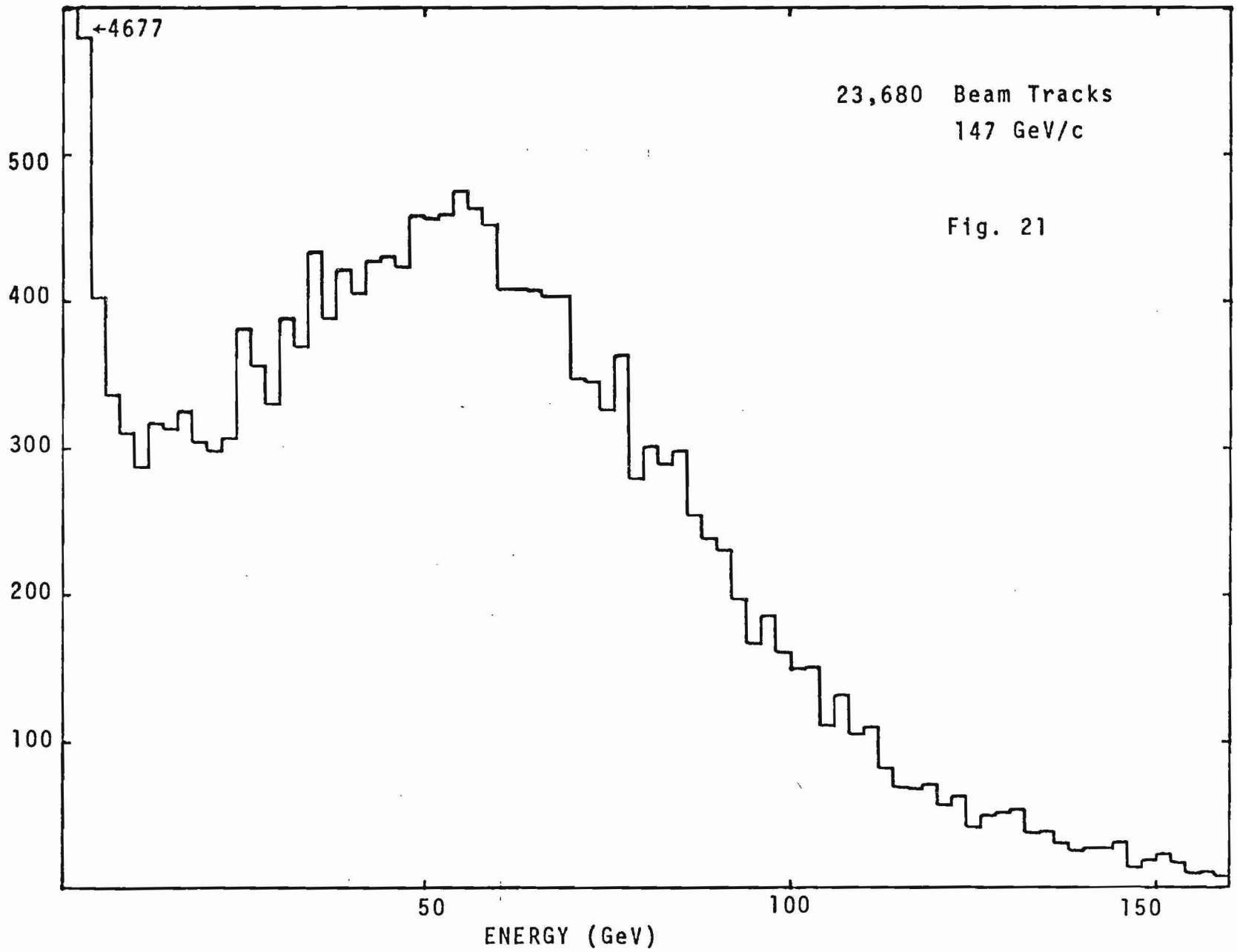
←4677
23,680 Beam Tracks
147 GeV/c
500
400
300
200
100
50
100
150
ENERGY (GeV)

Fig. 21

beam particles deposit less than 2 GeV; 27% deposit less than 10 GeV. Figure 22 shows the charged track distribution from pion-proton events at the last downstream PWC before the gamma detector. The net results are: 1) 90% of events have charged hadrons which hit the gamma detector and 2) 80% of these charged hadrons deposit a substantial amount of their energy. Neutron showers contribute a serious background in proton-proton events.

Examination of shower profiles from non-interacting beam tracks, and from the fast tracks in elastic events, demonstrated that hadronic showers are typically much more erratic, and spread over a larger area, than electromagnetic showers. In order to study shower characteristics carefully, event by event. an interactive version of the GAMMA program was written. The precision CRT of the M.I.T. PEPR system was used to display event information at various stages of processing. The operator could elect to examine and modify, via teletype or sense switches, all crucial steps in the pattern recognition and fitting of the gamma detector data. Most useful features included 1) maxima could be added or deleted from each hodoscope plane before the triple search, 2) each minimal set of triples could be examined and the operator's choice could be compared with the GAMMA selection, 3) triples could be deleted from the final fit to the hodoscope data, and replaced with others to obtain a better overall fit, 4) hadrons could be included in the final energy fit using trajectories determined from PWC data.

Figure 23 shows the CRT display of a three-shower π^+-proton

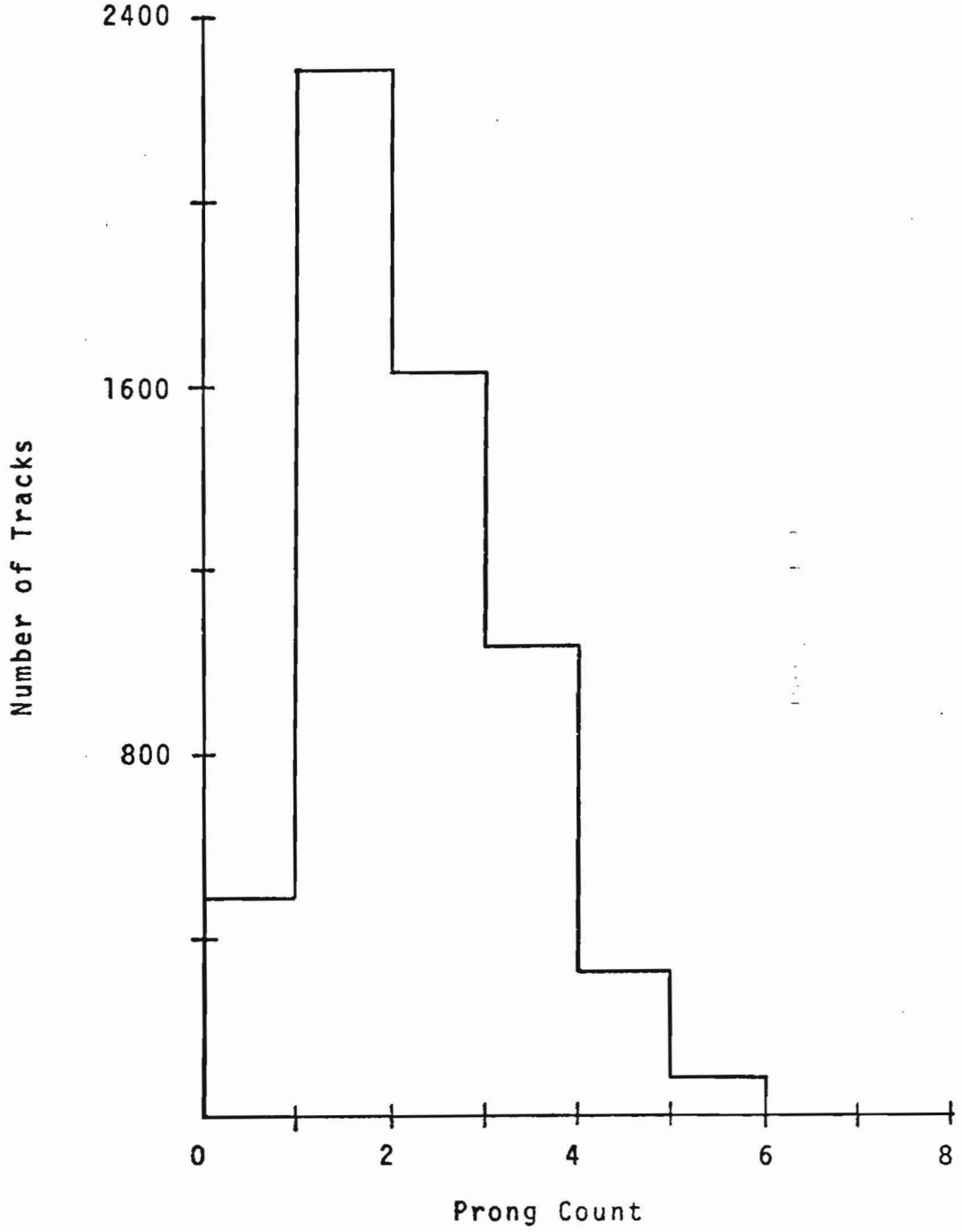

Fig. 22 - Number of Charged Tracks which Strike the Absorber.

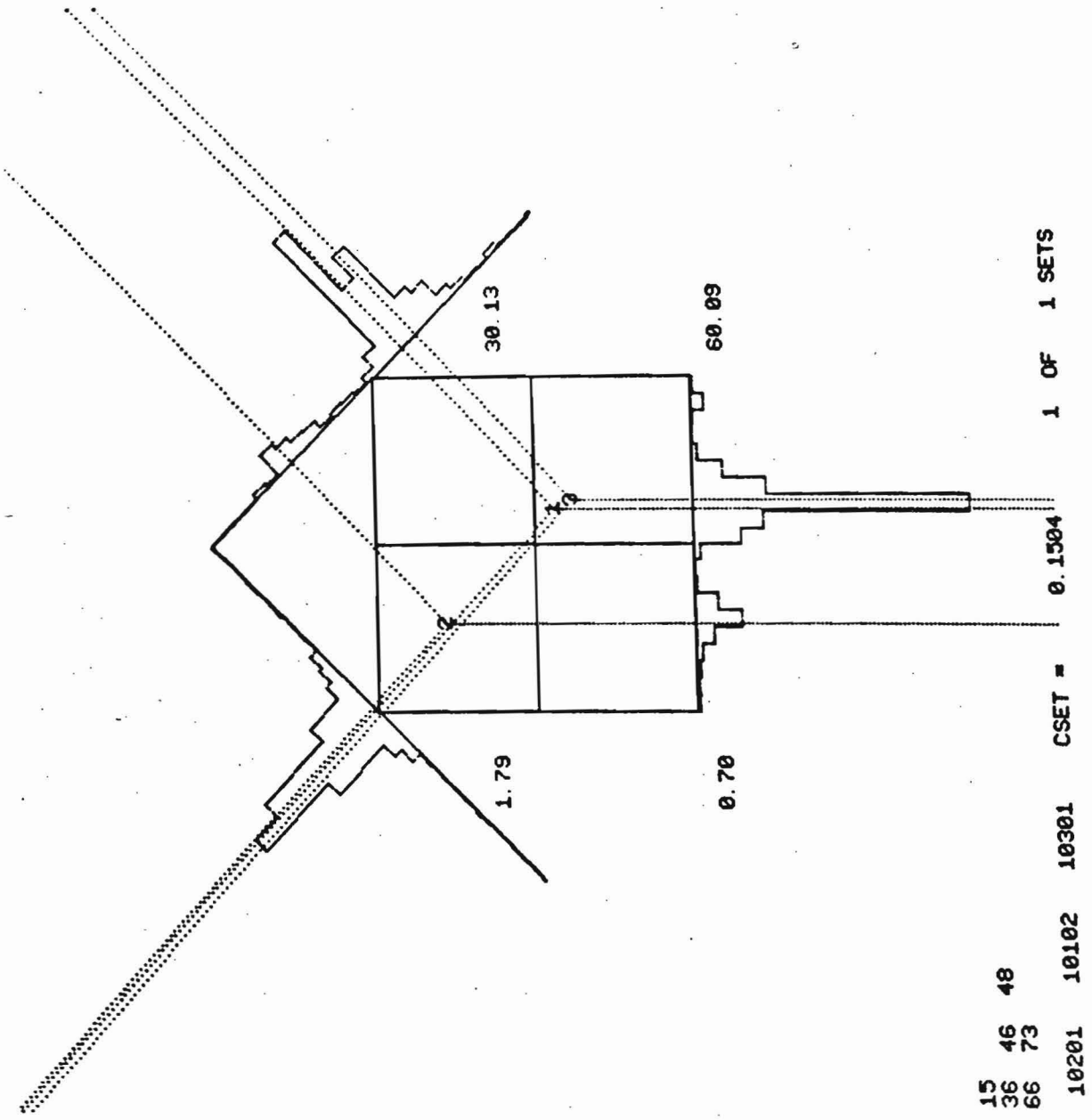
30.13
60.09
1.79
0.70
1 OF 1 SETS
0.1504
CSET =
10301
10102
48
46
73
10201
15
36
66

Fig. 23

event, where the two high energy showers are assumed to result from the two-gamma decay of a π^0. The detector appears as (schematically) viewed by a incoming particle. The three histograms represent signal intensities from the scintillator-hodoscope planes, and the program-selected triples of the best minimal set are indicated by dotted lines connecting the associated maxima. The four large squares represent the absorber blocks; nearby numbers are the energy (GeV) deposited in each absorber block. Hodoscope maxima and selected set information are given beneath the detector display. Figure 24 shows a histogram display after the triple selection and Figure 25 displays the final fit result to the hodoscope data. An energy distribution fit is shown in Figure 26. Shower #1 was deleted from the fit by the operator resulting in a poor χ^2 (bottom) and an unacceptable fit to the absorber energy distribution. The combined energy of showers 1 and 2 can be easily determined since shower 3 occurs in separate blocks. Note that energy deposited in each converter bar is given in addition to the energy for each absorber block. This information is not used in the automatic shower location procedure, but it is very useful for checking that the energy distribution in the lead glass blocks agrees with calculated shower centroids.

Figure 27 shows two well-resolved showers resulting from a $\gamma \rightarrow e^+e^-$ conversion, probably in the bubble chamber window. Both charged particle trajectories were reconstructed in the

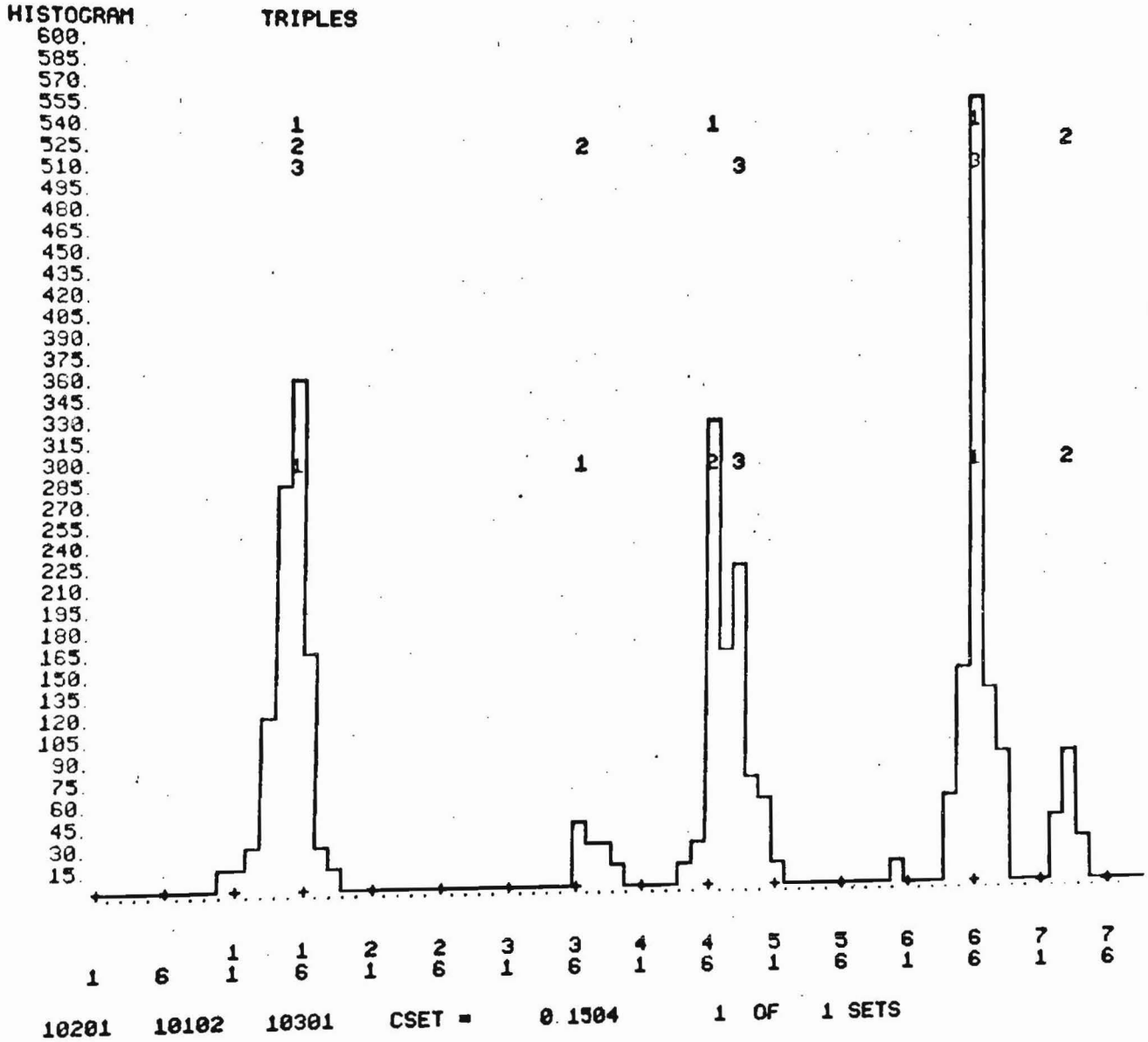
HISTOGRAM
TRIPLES
600.
585.
570.
555.
540.
525.
510.
495.
480.
465.
450.
435.
420.
405.
390.
375.
360.
345.
330.
315.
300.
285.
270.
255.
240.
225.
210.
195.
180.
165.
150.
135.
120.
105.
90.
75.
60.
45.
30.
15.
1 6 11 16 21 26 31 36 41 46 51 56 61 66 71 76
10201 10102 10301 CSET = 0.1504 1 OF 1 SETS

Fig. 24

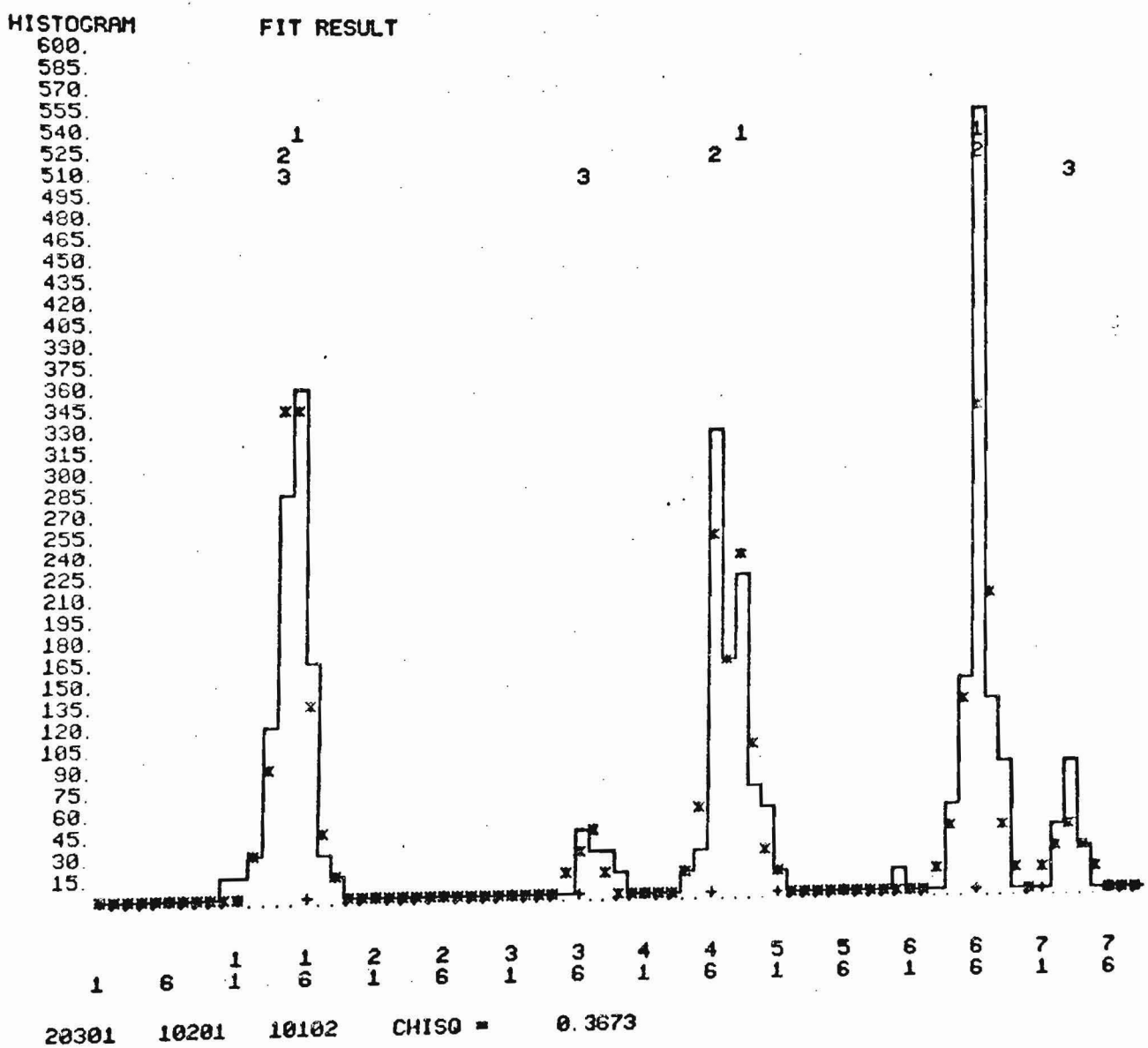
HISTOGRAM
FIT RESULT
600.
585.
570.
555.
540.
525.
510.
495.
480.
465.
450.
435.
420.
405.
390.
375.
360.
345.
330.
315.
300.
285.
270.
255.
240.
225.
210.
195.
180.
165.
150.
135.
120.
105.
90.
75.
60.
45.
30.
15.
1 2 3
3
1 2
10
3
1 6 11 16 21 26 31 36 41 46 51 56 61 66 71 76
20301 10201 10102 CHISQ = 0.3673

Fig. 25

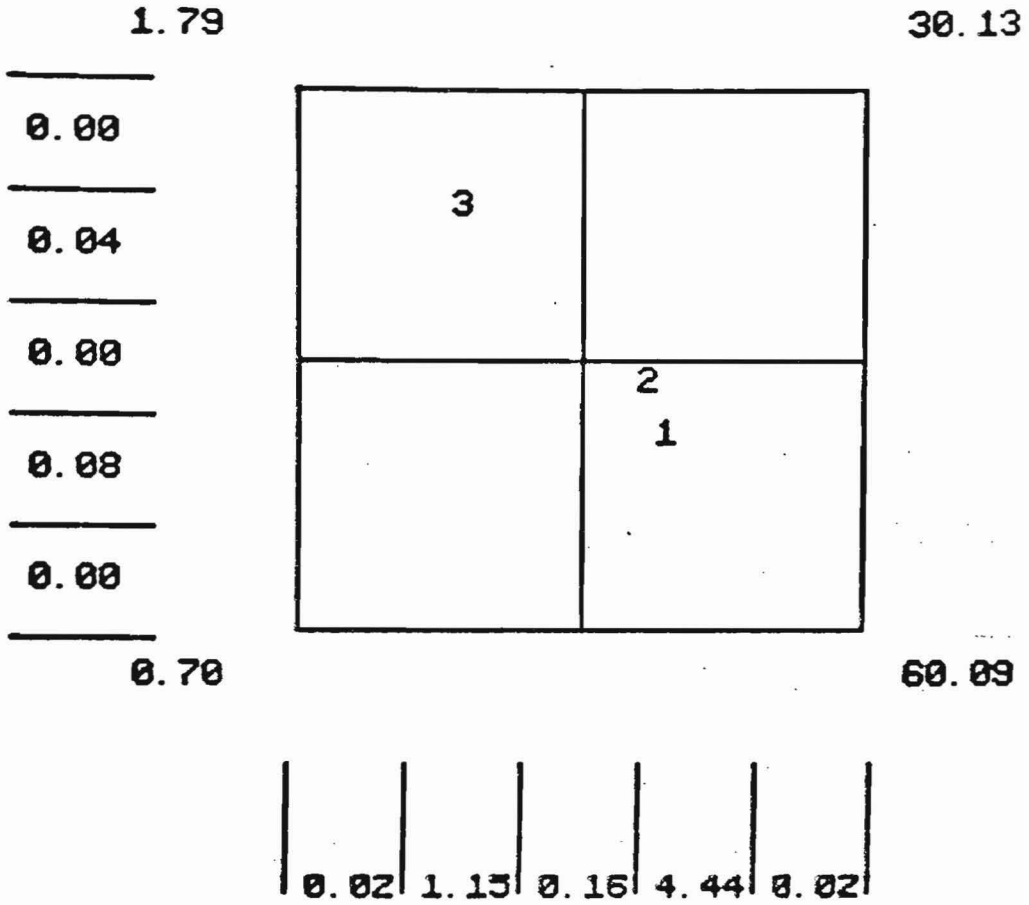

SHOWER	7	7	4
EMIN	0.000	0.000	1.199
ERES	0.000	0.000	1.199
EMAX	95.598	97.384	2.985
EFIT	0.000	78.400	0.852
DE	0.000	8.908	1.347

TRACKS --- CERENKOV = 6

CHI2 = 14.91 EABS = 1.79 12.21 2.73 62.52

Fig. 26

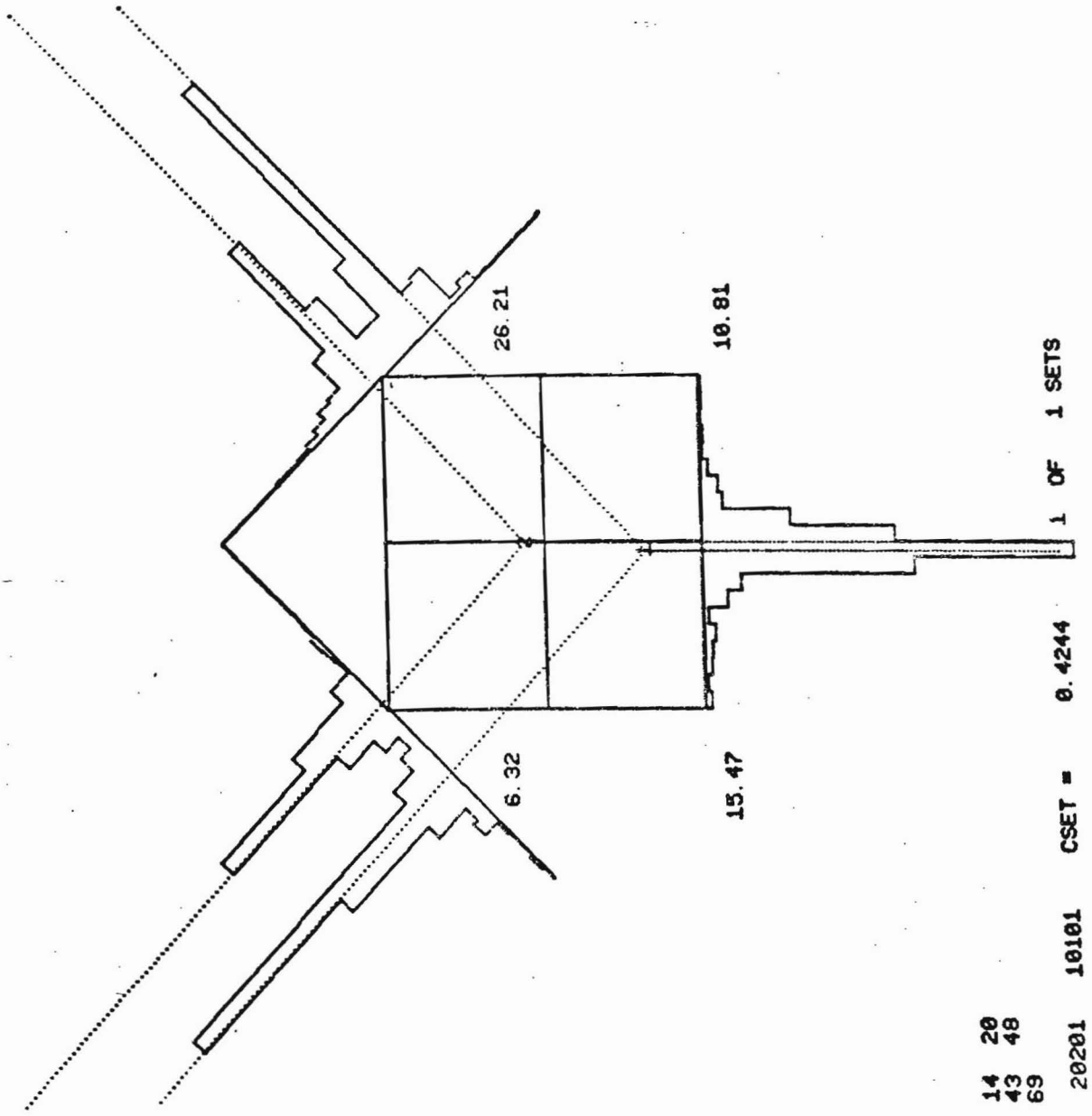
26.21
10.81
6.32
15.47
1 OF 1 SETS
0.4244
CSET =
10101
20201
14 20
43 48
69

Fig. 27

downstream PWC system and coincide with the observed showers in the hodoscope planes. The separation is due to the residual magnetic field outside the chamber.

The entire two-prong event sample was processed using the interactive program. Hadron showers detected in the hodoscope generally produced multiple peaks of an erratic nature and relatively low intensity, as compared to electron showers. The shower location algorithm did not successfully handle the majority of these events, and even operator intervention produced little improvement in many cases. The automatic version of GAMMA attempted to assign gamma interpretations to spikes resulting from hadron showers. This was first suspected from the large number of "gammas" observed in elastic events, and confirmed by the CRT event displays. To circumvent operator assisted reprocessing of all events, a hadron shower reject category was established for the ADC data. Generally, in events judged to have hadron showers, GAMMA did automatically locate at least one shower very near the hadron trajectory. This allowed rejection of nearly all such events (~ 21-23% of the final sample).

C. Gamma Detector Acceptance

The gamma detector acceptance was determined by a Monte Carlo program written for this purpose. Fake π^0's of fixed total energy and limited transverse momentum with respect to beam direction were generated within the fiducial volume of the bubble chamber. These were allowed to decay into two gammas according to a probability distribution isotropic in the π^0 rest frame. The decay point was chosen from a uniform random distribution along the beam (x) direction, and the transverse beam profile was approximated with separate Gaussian distributions in y and z. The beam dip angle, λ , was fixed at the average value for beam tracks as determined from the PWC system. The second beam angle, $\emptyset$, decreases linearly with x; this average $\emptyset(x)$ was also determined from PWC beam tracks. The gammas are extrapolated through the remaining bubble chamber liquid, stainless steel window, and aluminum vacuum jacket. An average gamma must traverse ~.24 radiation lengths to escape the chamber. Air, mylar, and PWC gas in the downstream system add .024 radiation lengths. However, once a gamma enters the no-field region beyond the first proportional wire chamber, the electron and positron resulting from gamma conversion do not separate, and a single shower appears in the gamma detector.

Figure 28 displays the probability of detecting two, one, or zero gammas from π^0 decay as a function of π^0 energy. Transverse momentum of the π^0 was assigned according to Gaussian

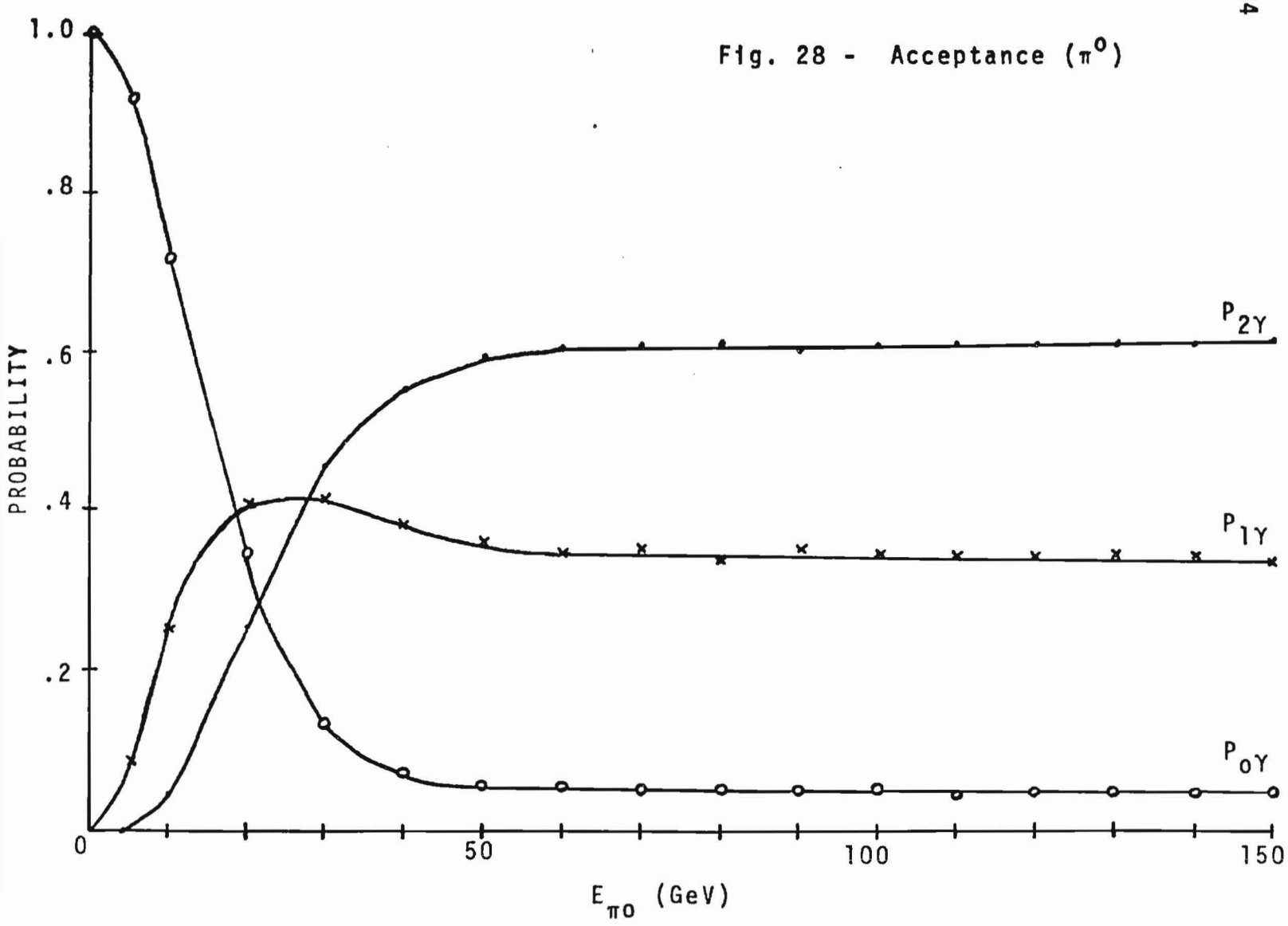

Fig. 28 - Acceptance (π^o)

distributions in p_y and p_z with standard deviations of 350 MeV/c.

Figure 29 contains the corresponding curves for two gamma decays of the $\eta^0(549)$.

Monte Carlo runs at several average values of transverse momentum in the range 0 - 500 MeV/c confirm that these acceptance curves are pratically flat for π^0 energies above 50 GeV.

The shower energy spectrum observed in the detector is not equivalent to the gamma energy spectrum. Two showers with centers separated by a distance comparable to the width of a hodoscope scintillator finger will not be resolved. This effect is also quite pronounced for asymmetric π^0 decays due to the tendency for the lower energy gamma to be lost in the "tail" of the higher energy gamma shower.

The fake gammas which strike the detector are allowed to "shower" in the scintillator hodoscope with exponential distributions in each scintillator plane. Data from the electron calibration runs were used to parametrize probability distributions for shower amplitude and exponential slope as a function of total shower energy. The algorithm for shower detection in the GAMMA program is then used to determine the number and positions of the fake gamma showers. This allows determination of the probability of resolving both gammas from a π^0 as a function of π^0 energy. Figure 30 gives the result. Figure 31 displays the average number of detected showers for a π^0 of given energy.

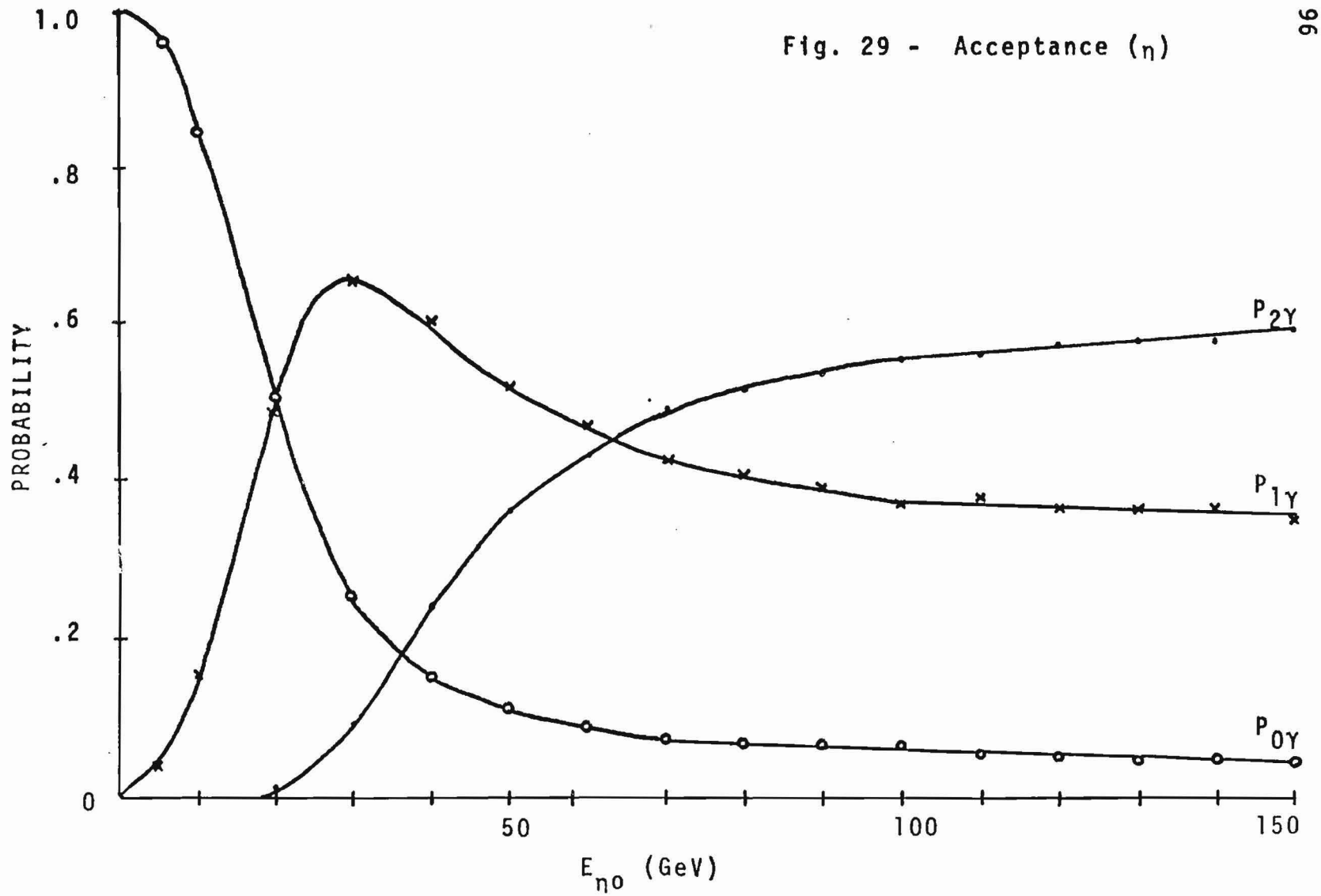

Fig. 29 - Acceptance (η)

Fig. 30 - Probability of Resolving Both γ's from π^0 Decay

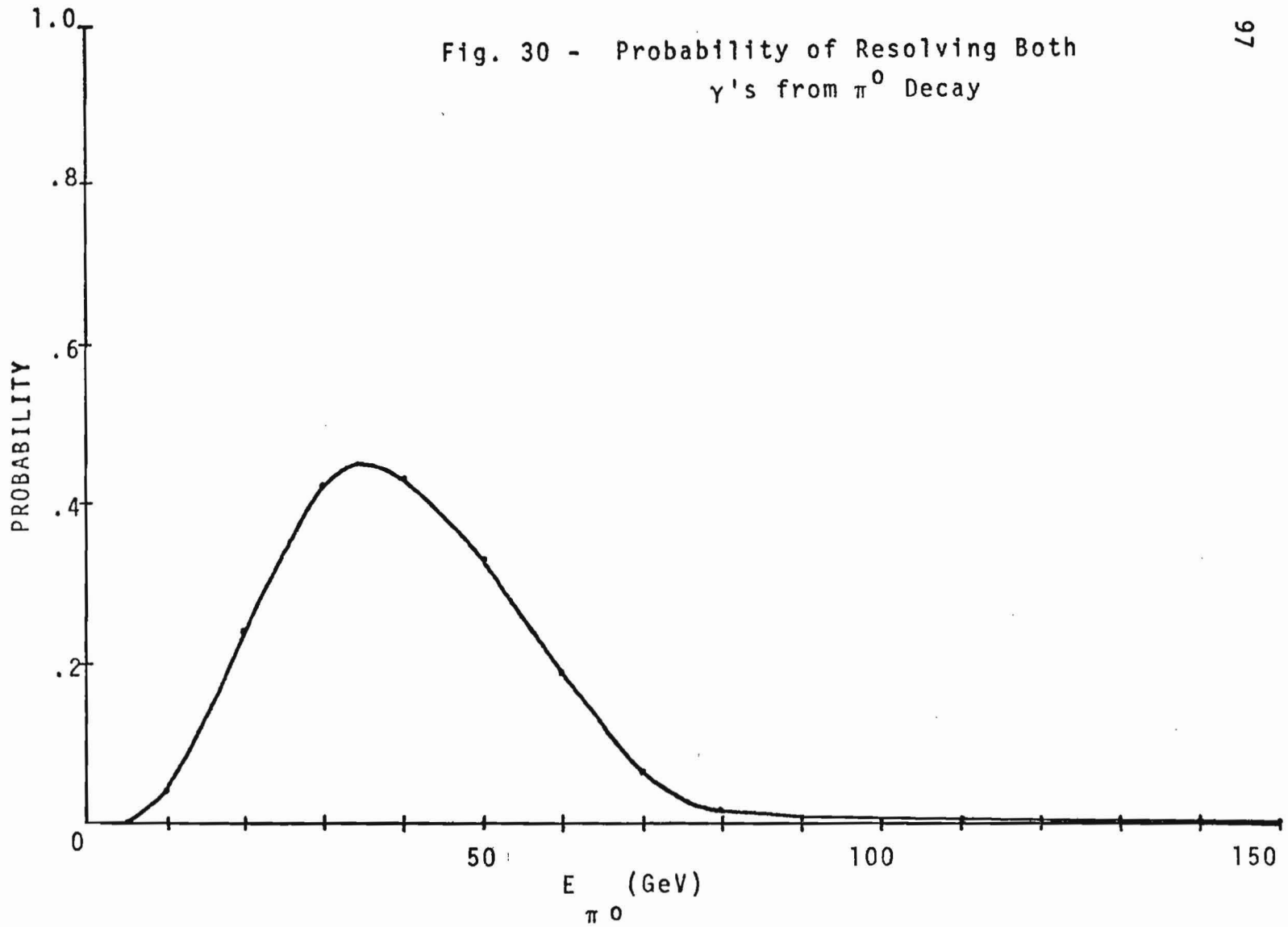

Fig. 31

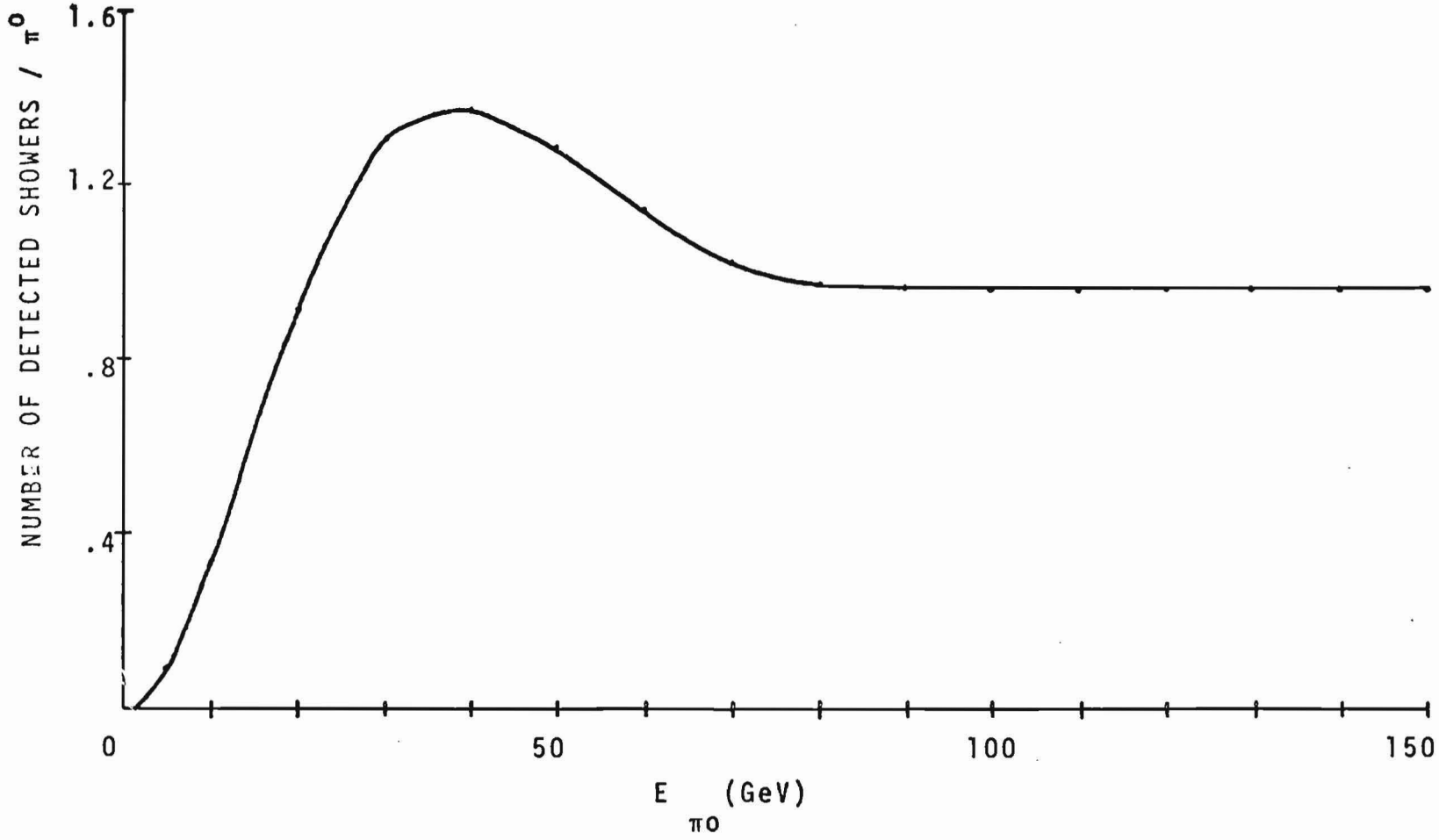

D. Forward Gamma Data and Results

The data sample with associated forward gamma information was found to have a total of 7507 events, which included 41 PWC data rejects and 71 ADC rejects due to multiple beam particles during the ADC gate. The remaining data contained 747 events identified as elastic by program PWGEL (Ludlam, 1977). The inelastic data was distributed as follows:

TABLE VI

		proton-proton	π^+ - proton
Total even prongs		2727	3204
Complete, charge balanced		2029	2252
Rejects:	Type 2Ø	102	108
	Type BC	147	138
	Hadron Shower	366	460
Final Sample		1404	1546

The rejects above remove bad, or questionable, events from the sample. Reject type 2Ø removes those events which contain a secondary vertex in the bubble chamber when the incident track has undetermined momentum. Reject type BC removes events having one or more tracks reconstructed in the bubble chamber (only) with momentum of 50 GeV/c or greater. Tables VII and VIII summarize the observed shower distributions from π^+ -

TABLE VII

Inclusive π^+p

Prong Count	Complete Charge-Balanced Events	Selected Events	No Shower	$\geq$ 1 Shower
2	275	242	123	119
4	530	482	200	282
6	552	497	152	345
8	443	395	110	285
10	277	246	54	192
12	117	94	30	64
14	44	38	10	28
16	11	11	2	9
18	3	1	0	1
	2252	2006	681	1321

TABLE VIII

Inclusive pp

Prong Count	CCB Events	Selected Events	No Shower	$\geq$ 1 Shower
2	337	264	140	124
4	490	434	194	240
6	485	435	186	249
8	335	300	113	187
10	217	191	58	133
12	111	95	31	64
14	40	38	11	27
16	12	11	2	8
18	2	2	1	1
	2029	1770	736	1033

-proton and proton-proton events, The hadron shower reject removes events having one or more charged tracks within one hodoscope finger-width of a shower, as discussed in Section I. Weights were assigned to each successful event based on the reject criteria. For example, each event which passed the hadron reject test was assigned a weight according to the number of charged particles which hit the gamma detector. A fixed probability was assumed for the hadron to produce a shower. The weights were:

Reject Class	Weight	Characteristics
2Ø	$(1.02)^{N_1}$	Track within .05 radian cone around beam track.
BC	$(1.16)^{N_2}$	Track with BC momentum $\geq$ 50 GeV, and within .05 radian cone
Hadron Shower	$(1.26)^{N_3}$	Track hits gamma detector

where N_1, N_2, N_3 are the number of tracks in the event which satisfy the characteristics of a reject class. A topology dependent weight was assigned to each event also, in order to give the correct topological cross sections.

No showers were observed in 585 π^+ - proton events, leaving 961 events with gammas and no detected hadron showers. A total of 648 proton-proton events had no shower, leaving 756 events with gammas and no detected hadron showers.

A search for π^0 production was performed by examining the 2-γ invariant mass distributions for both π^+-proton and proton-proton interactions. Combinations were not included if one, or both, of the showers was associated with a charged hadron, electron, or positron track. Events were removed from the sample when the energy distribution fit (section V) failed for the absorber blocks. In addition, events were not included when the total fit energy exceeded the measured energy by 5 GeV or more. A total of 538 π^+-proton events and 446 proton-proton events were left. Corresponding invariant mass distributions are sown in Figures 32 and 33. No clear π^0 signal is seen, only a very broad peak centered below the π^0 mass (135 MeV/c^2). The acceptance calculations had indicated that the number of π^0 decays for which both gammas are resolved, is quite small. In addition, errors in transverse shower location near the edge of the absorber blocks tend to produce large errors in the energy distribution fit, and the largest gamma flux occurs near the intersection of the four absorber blocks. It appears that reliable separation of π^0's from a cut in the 2-γ invariant mass plot is not possible. The energy resolution of a single shower is certainly well measured ($\frac{\Delta E}{E} = \frac{27}{\sqrt{E}}$ % FWHM), however, and from the acceptance calculations we know that two gammas from π^0 decay will overlap in the detector at high energy and appear as a single shower. The criteria in Table IX will be used to select a π^0 sample (perhaps a blatant assumption,

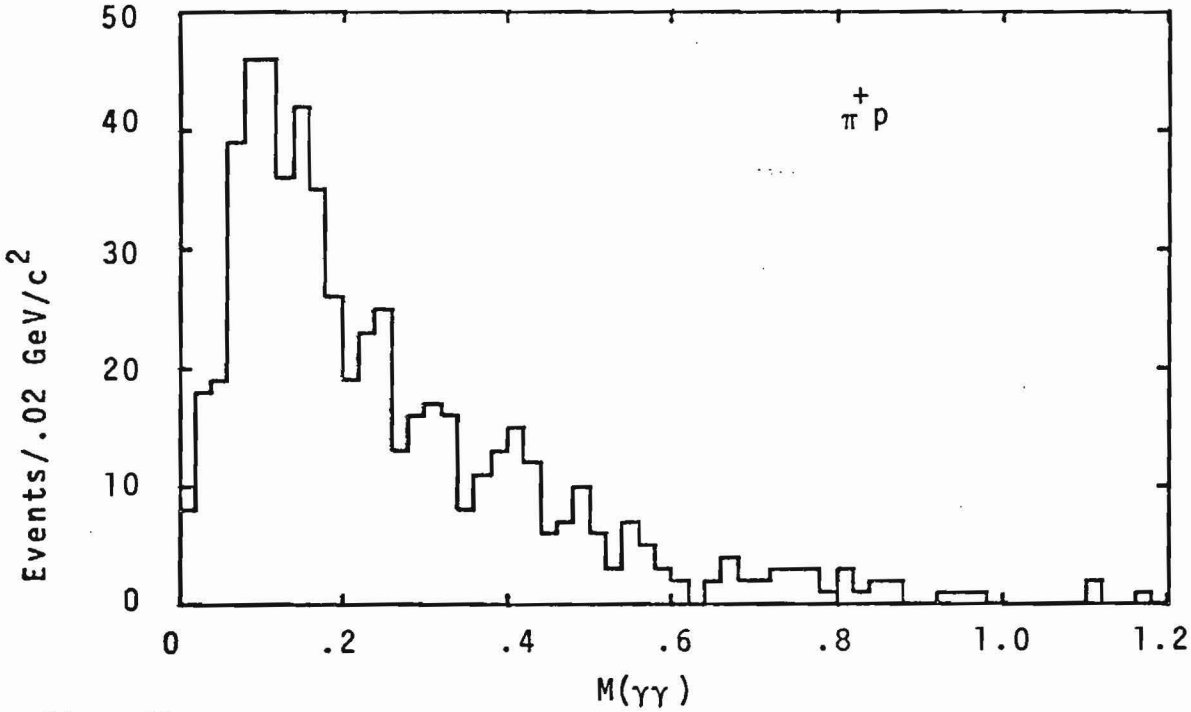
50
40
30
20
10
0
Events/.02 GeV/c^2
$\pi^+ p$
0
.2
.4
.6
.8
1.0
1.2
M(γγ)

Fig. 32

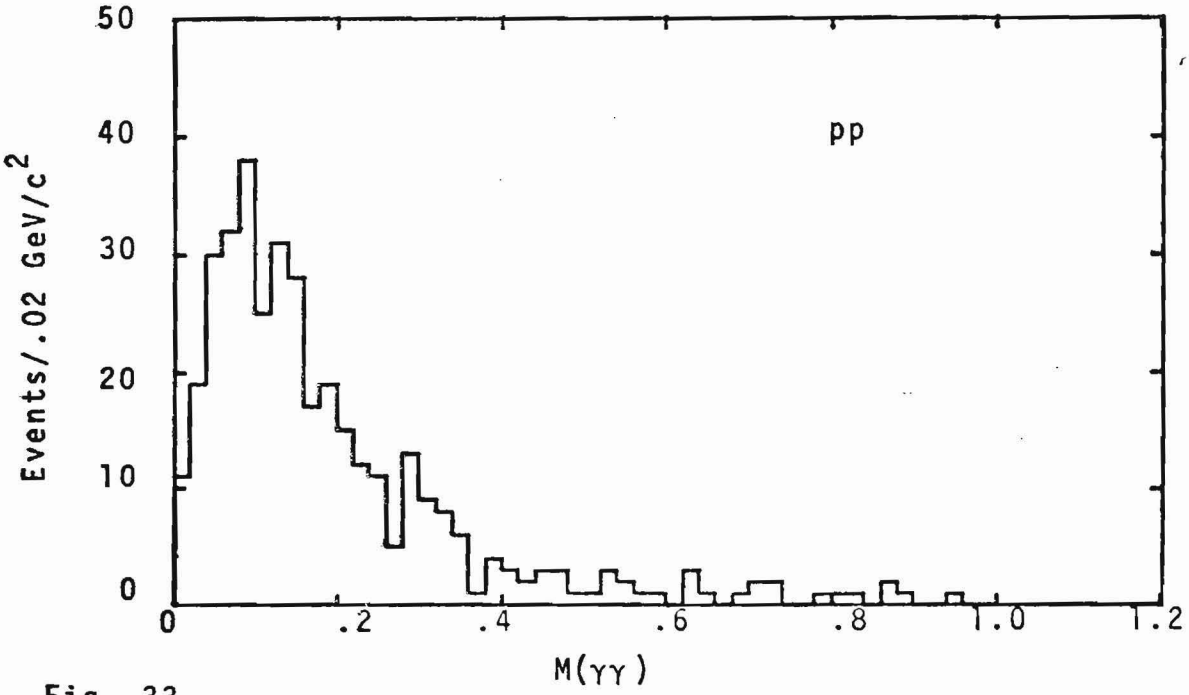
50
40
30
20
10
0
Events/.02 GeV/c^2
pp
0
.2
.4
.6
.8
1.0
1.2
M(γγ)

Fig. 33

considering the width of the 2-γ mass distribution!). The following Figures 34 - 41 give the resulting single-particle π^0 distributions in Feynman x, rapidity, transverse momentum, and total laboratory energy for π^+-proton and proton-proton interactions. Reject weights and topological cross section weights were applied. Acceptance corrections were not used; these are applied in Section VI-C.

TABLE IX

Selection criteria for π^0's:

1) Hodoscope fit has acceptable χ^2.

2) Energy distribution fit has acceptable χ^2. Calculate the invariant mass for all pairs of gammas. Examine $(.04)^2 \leq M^2 \leq (.29)^2$ to select π^0's. If a single shower occurs in more than one combination, take the one with $M^2_{\gamma\gamma}$ nearest $M^2_{\pi 0}$.

3) Check remaining pairs and pairs from events for which the energy fit failed. If a pair is resolvable in the second converter layer and in the absorber (at least), compute the minimum opening angle for a π^0 of energy equal to that of the (resolved) pair of showers. If this angle is less than the measured angle, and the measured angle is less than three times the minimum angle, assume the pair is a π^0.

4) Check unused single showers. If energy $\gtrsim$ 60 GeV, and the energy fit was successful, use the fit result. If the energy fit failed, ubt the shower is resolvable, use the resolved value.

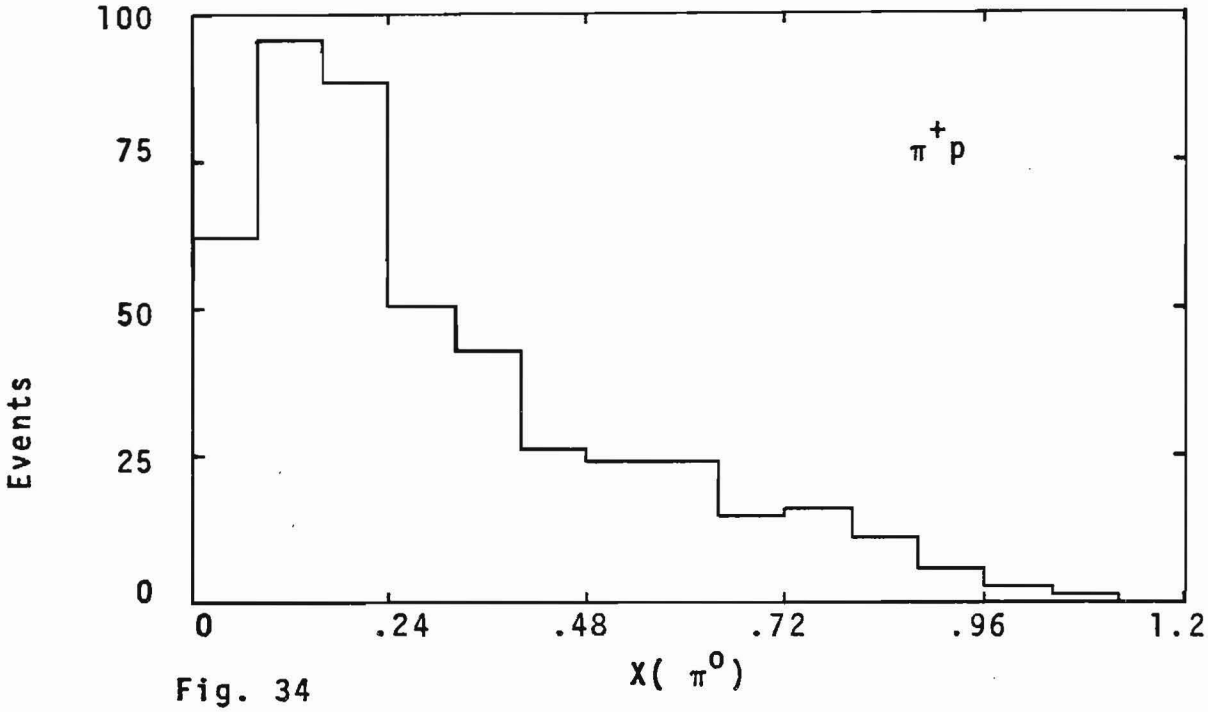
100
75
50
25
0
Events
$\pi^+ p$
0
.24
.48
.72
.96
1.2
X(π^o)

Fig. 34

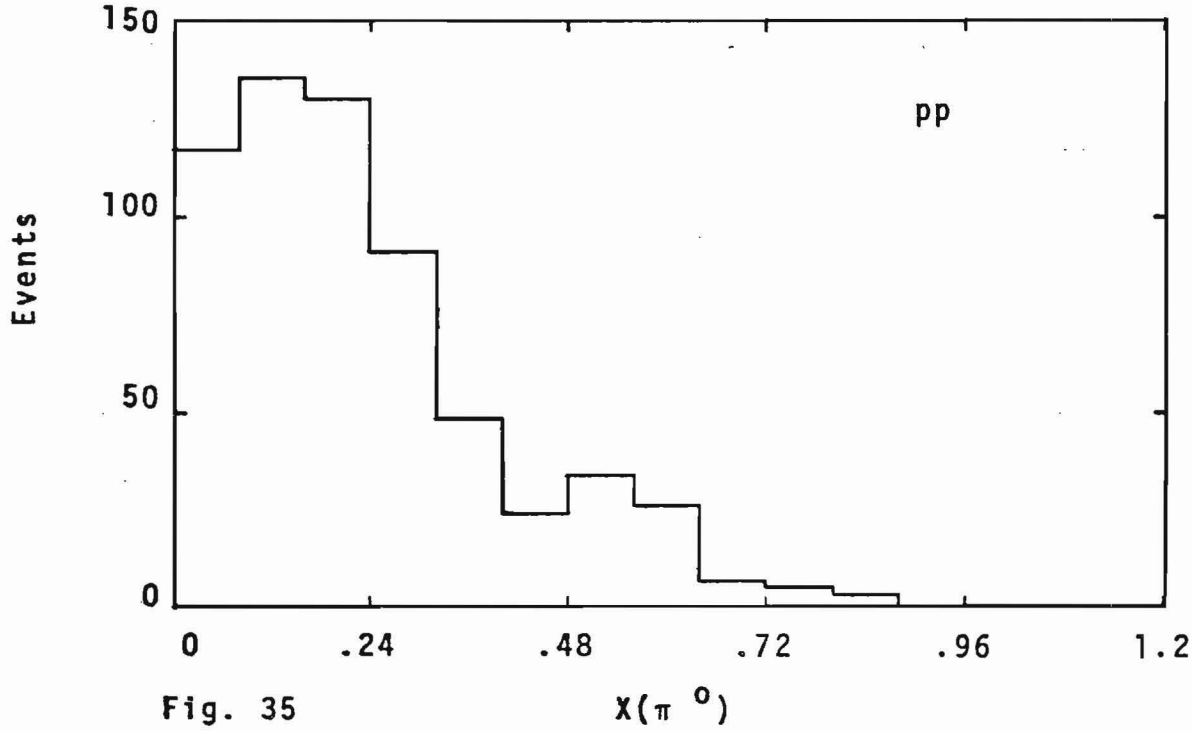
150
100
50
0
Events
pp
0
.24
.48
.72
.96
1.2
X(π^o)

Fig. 35

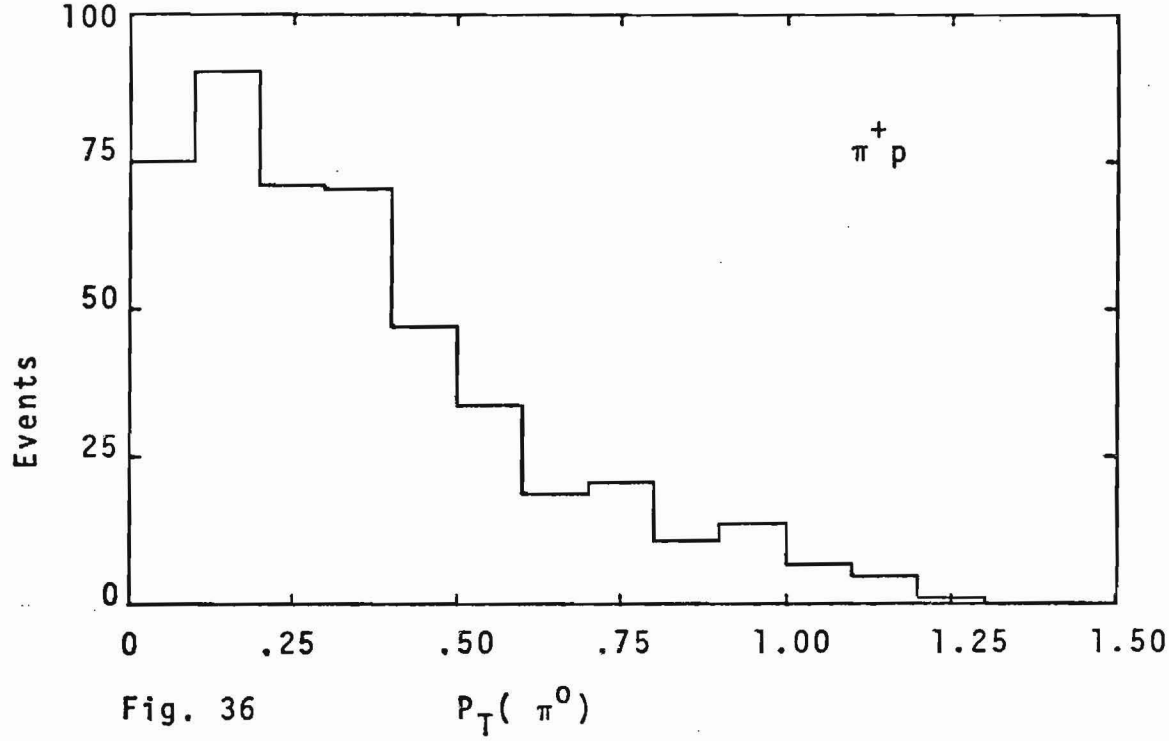
100
75
50
25
0
Events
$\pi^+ p$
0
.25
.50
.75
1.00
1.25
1.50
$P_T(\pi^0)$

Fig. 36

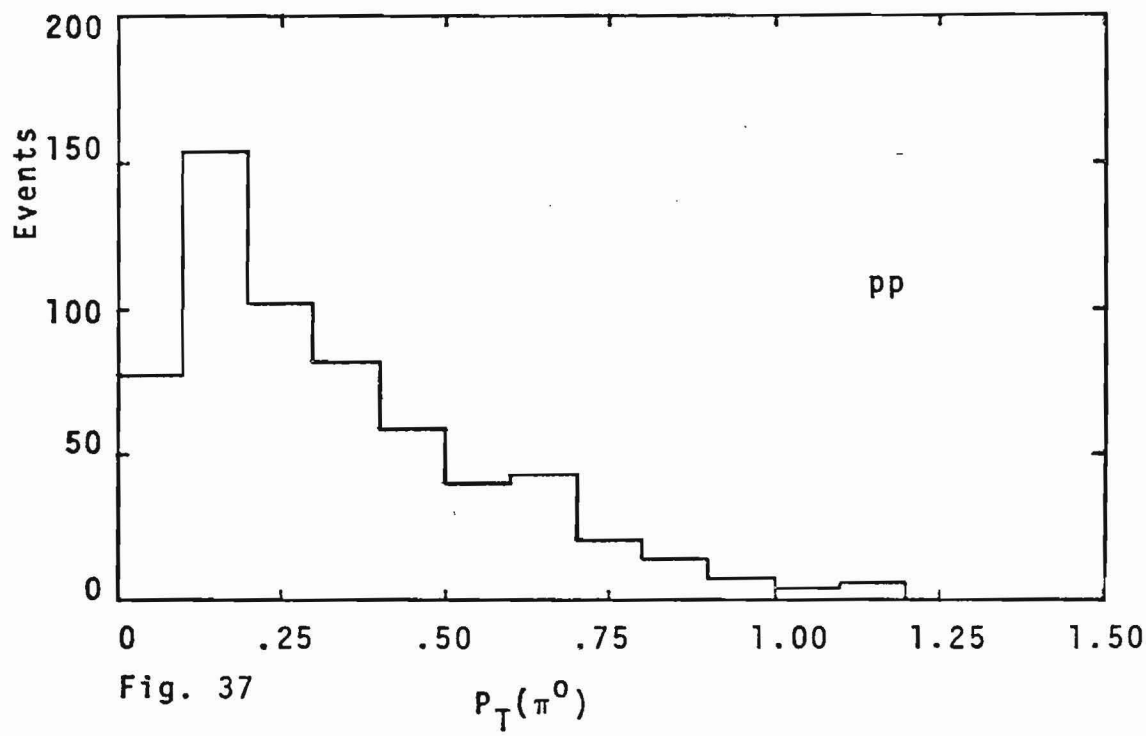
200
150
100
50
0
Events
pp
0
.25
.50
.75
1.00
1.25
1.50
$P_T(\pi^0)$

Fig. 37

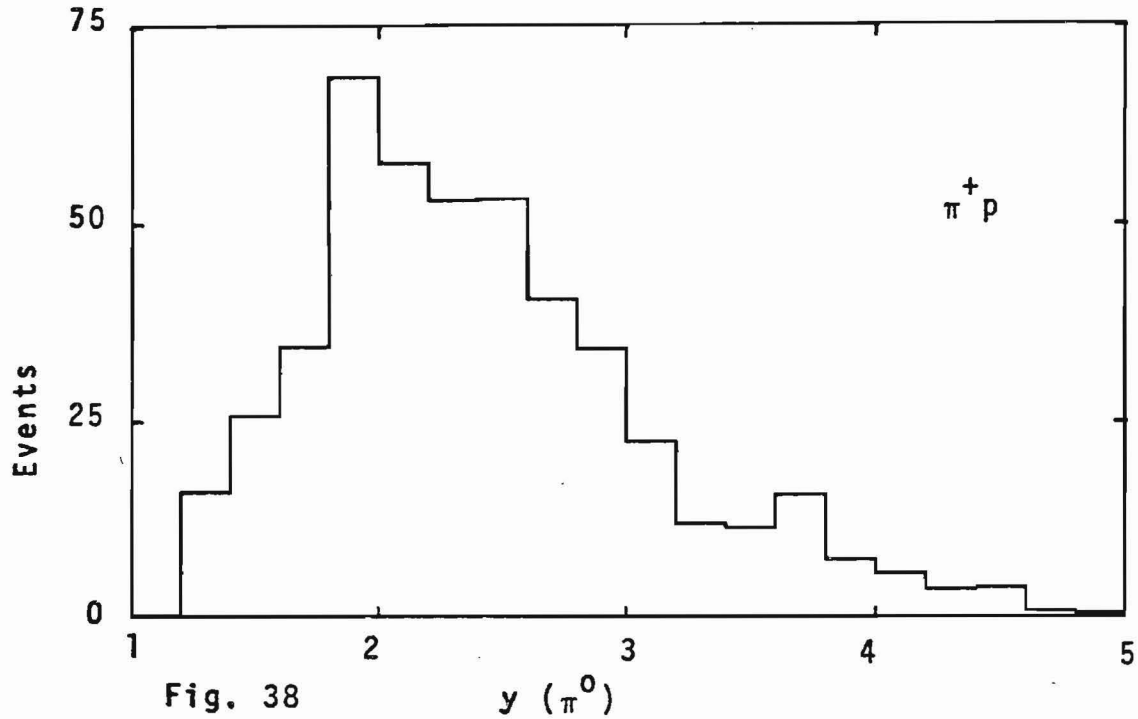
75
50
25
0
Events
$\pi^+ p$
1
2
3
4
5
y (π^0)

Fig. 38

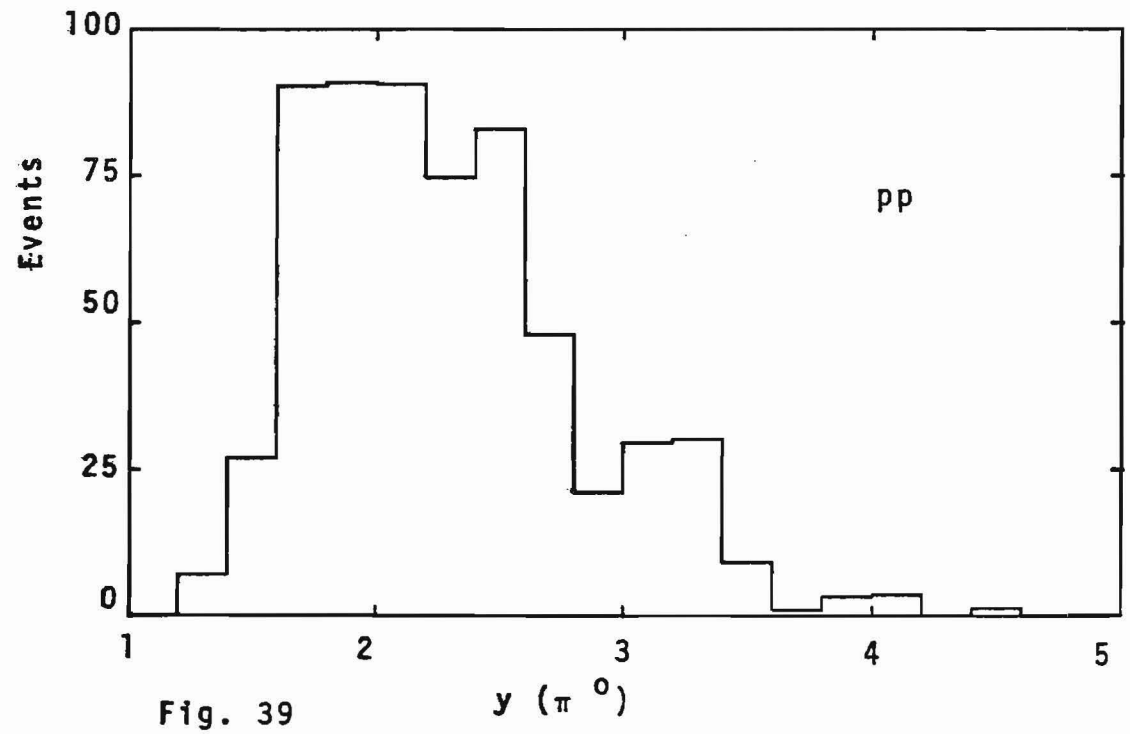
100
75
50
25
0
Events
pp
1
2
3
4
5
y (π^0)

Fig. 39

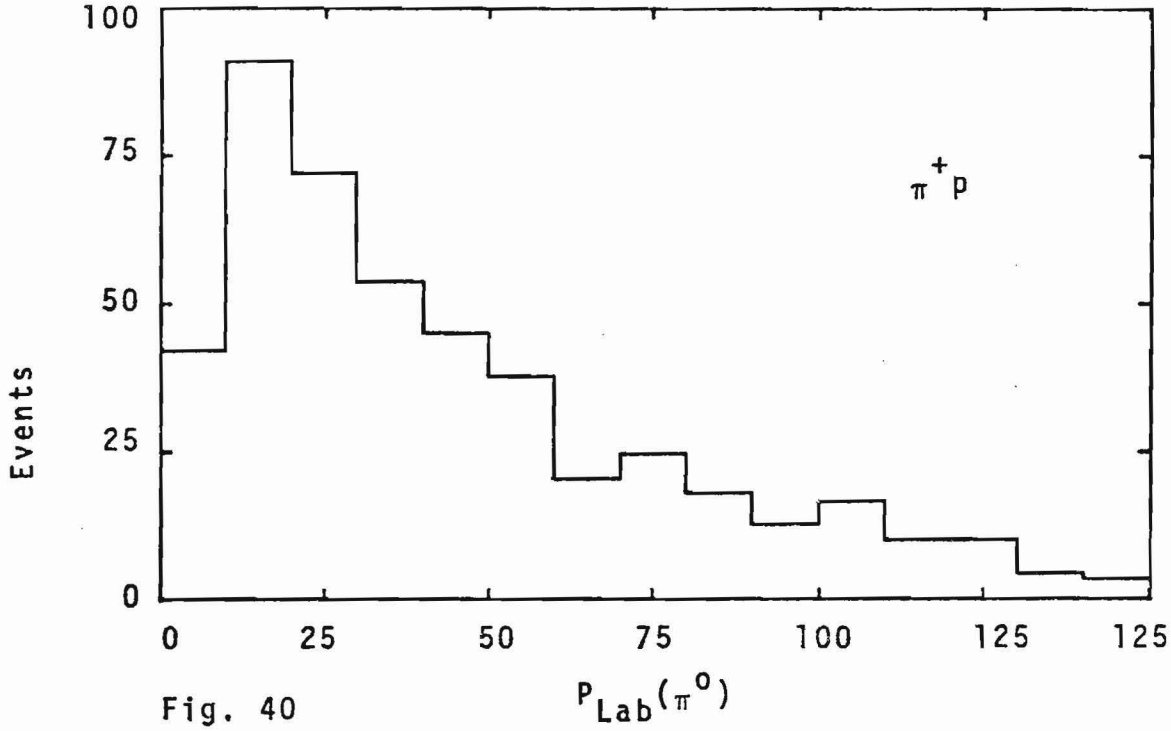
100
75
50
25
0
Events
$\pi^+ p$
0
25
50
75
100
125
125
$P_{Lab}(\pi^o)$

Fig. 40

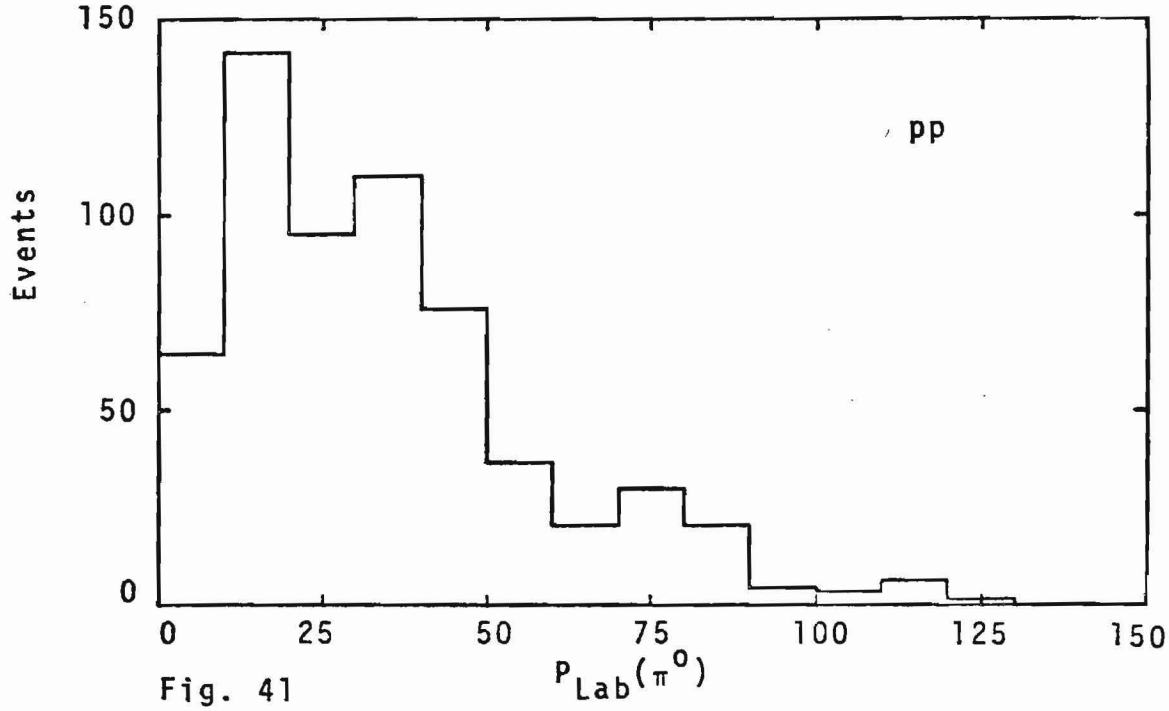
150
100
50
0
Events
pp
0
25
50
75
100
125
150
$P_{Lab}(\pi^o)$

Fig. 41

VI. Evidence for Diffraction Dissociation of Hadrons

This section will review various attempts to separate diffractive contributions from the charged particle multiplicity distributions in hadron-hadron interactions. Our data for π^+p, K^+p,pp at 147 GeV/c have been fit to a "two component" model, as well as published data for π^-p at 147 GeV/c. (D. Fong, et al. 1976a). A method is presented for accomplishing such a separation on an event-to-event basis. Results for π^+p and pp are compared with the inclusive two component fits. This method is then used to select an enhanced sample of diffractive events for study of the dissociation process.

A. Two Component Models

It was suggested several years ago (Erwin et al., 1974) that the multiplicity distribution of produced particles in hadron-hadron collisions should obey a Poisson distribution. The multiperipheral model produces this result and predicts the average multiplicity should grow as $\ln s$. Bubble chamber experiments from 50 - 400 GeV have found that the inelastic charged particle multiplicity distribution for $N \gtrsim N_{average}$ is well described by a Poisson distribution in the number of produced negatives:

$$P_{N_-} = \frac{\langle N_- \rangle^{N_-}}{N_-!} e^{-\langle N_- \rangle}$$

Table $\overline{X}$ displays results of the fits to the multiplicity distributions for pp, K^+p, and π^+p interactions at 147 GeV/c. In all cases, an excellent fit is achieved for $N \geq 10$ prongs.

TABLE $\overline{X}$

Reaction	Prong Count	$< N_- >$	$A^{(mb)}$	χ^2/D.F.
pp	10 - 20	3.14 ± .06	23.86 ± .97	.72
π^+p	10 - 20	3.06 ± .04	17.17 ± .41	.26
K^+p	10 - 18	3.16 ± .04	13.24 ± .32	.039

Figure 42 displays $\ell n\ (N_-!\ \sigma_{N_-})$ versus N_-. The straight lines have a common slope of 3.10.

Extrapolation of the Poisson fit reveals an excess of events in the low multiplicity final states.

TABLE XI

Reaction	σ inelastic	fit σ poisson	σ difference
pp	31.62 ± .35	23.86 ± .97	7.76 ± .97
π^+p	19.84 ± .23	17.17 ± .41	2.67 ± .41
K^+p	16.95 ± .49	13.24 ± .32	3.71 ± .49

The value of σ diff. for π^+p is surprisingly low compared to leading particle cross secitons, however, the errors are quite large. The value for pp is somewhat higher than the published

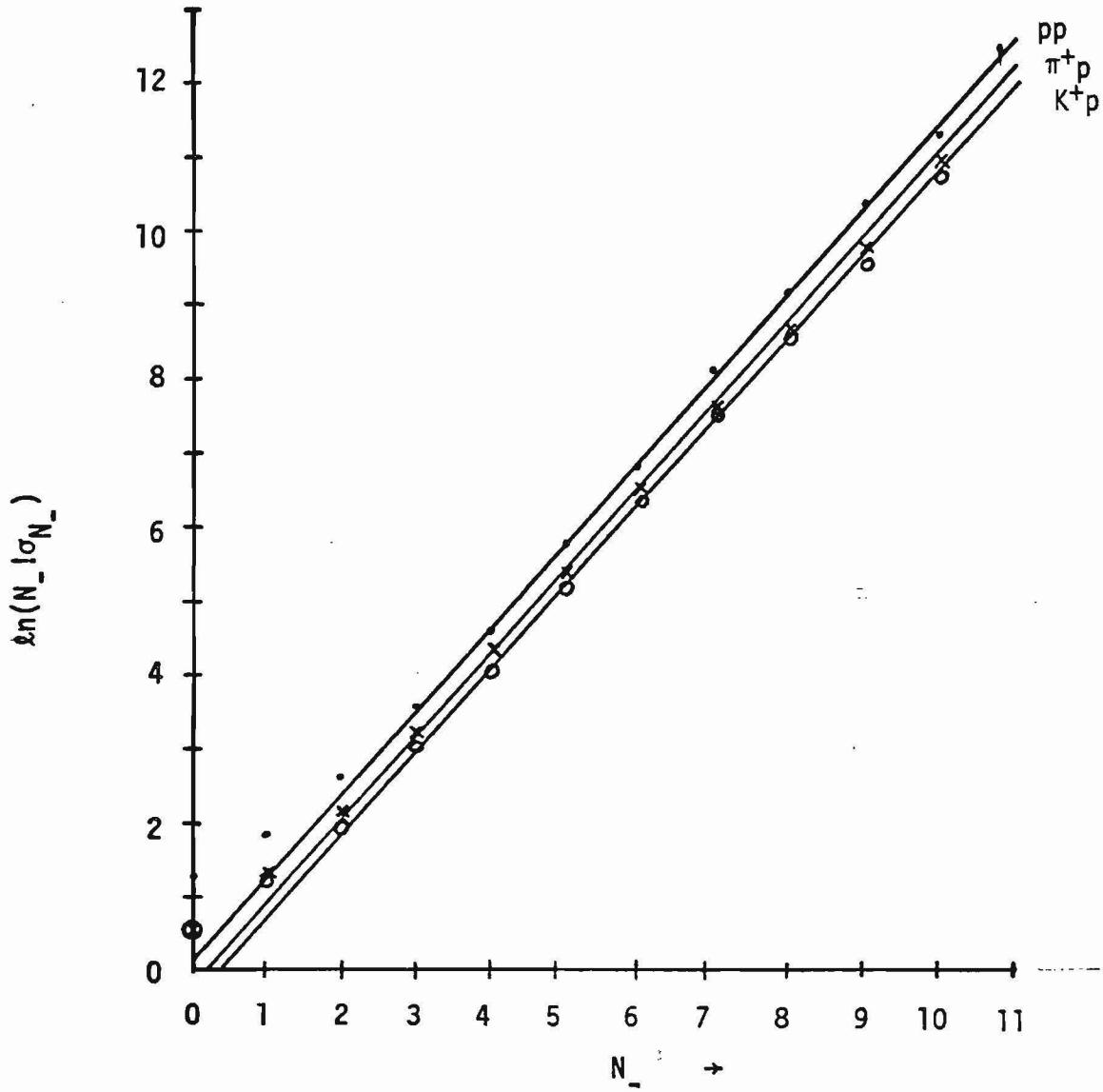

Fig. 42 - π^+p, K^+p, pp at 147 GeV/c compared with Poisson, $\langle N_- \rangle = 3.1$.

leading particle cross sections (Whitmore, 1974).

Fiałkowski and Miettinen (1973) fit the inelastic pp data from 15-300 GeV/c to a two component model, assuming a constant diffractive term plus a Poisson term with $N_- \propto \ln s$. They obtained diffractive cross sections of 2.26 $\pm$ .50, 3.08 $\pm$ .40, 1.69 $\pm$ .70, and 0.58 $\pm$ .30 mb for the 2, 4, 6, and 8 prongs respectively.

Harari and Rabinovici (1973) also performed a two component fit assuming diffractive contributions in the 2, 4, and 6 prong events. They fit the energy dependence of the average multiplicity, $\langle N \rangle$, and the moment $f_2 = \langle N(N-1) \rangle - \langle N \rangle^2$ using a non-diffractive component proportional to $\ln s$. Their fit to inelastic pp data from 50-300 GeV/c gave diffractive cross sections of 2.0, 2.2, and 0.9 mb for 2, 4, and 6 prongs respectively.

Lach and Malamud (1973) found the inelastic pp cross section at Fermilab energies well described by the sum of two Poisson distributions. In this two-component model, one Poisson is assumed to describe the diffractive part and the other describes the non-diffractive part. This model has been reexamined recently (d'Innocenzo et al., 1978) using a larger data sample. It is noted that below 50 GeV/c even a single Poisson is too broad to describe the pp cross section, and the fits are apparently becoming worse at higher energies (405 GeV/c) as well. D'Innocenzo et al. propose a new two component

model in which the two Poisson distributions are replaced by an exponential multiplicity distribution, for a two fireball component including the elastic cross section, and a Gaussian distribution describing a second, three fireball, component. This model yields superior fits over a wider range of energy than do the two Poissons; however, additional parameters are introduced. We note also that this model would interpret the two-prong final state as part of the three-fireball component, rather than the two-fireball component as one would expect of a channel dominated by diffractive contributions.

The results of fitting our data to the sum of two Poissons is given in the following table:

TABLE XII

Reaction	fit σ diff	fit σ non-diff	fit σ inel	meas σ inel	diff. $\langle N_- \rangle$	non-diff. $\langle N_- \rangle$
pp	10.48±1.37	21.13±1.44	31.61	31.62±.35	1.38±.13	3.23 ± .07
π^+p	3.62± .82	16.22± .84	19.84	19.84±.23	1.26±.18	3.12 ± .06
K^+p	5.08±1.14	11.91±1.14	16.99	16.95±.49	1.38±.18	3.26 ± .12
π^-p	4.30±1.70	16.74±1.78	21.04	21.00±.29	1.33±.33	3.05 ± .11

χ^2 / degrees of freedom were .79, .91, .36, and 1.34 respectively for pp, π^+p, K^+p, and π^-p. The resultant multiplicity distributions for the diffractive component are shown in Figure 43. It should be noted that the average number of produced negatives is the same, within errors, for all reactions, $\cong$ 1.34 for the for the diffractive component and $\cong$ 3.17 for the non-diffrac-

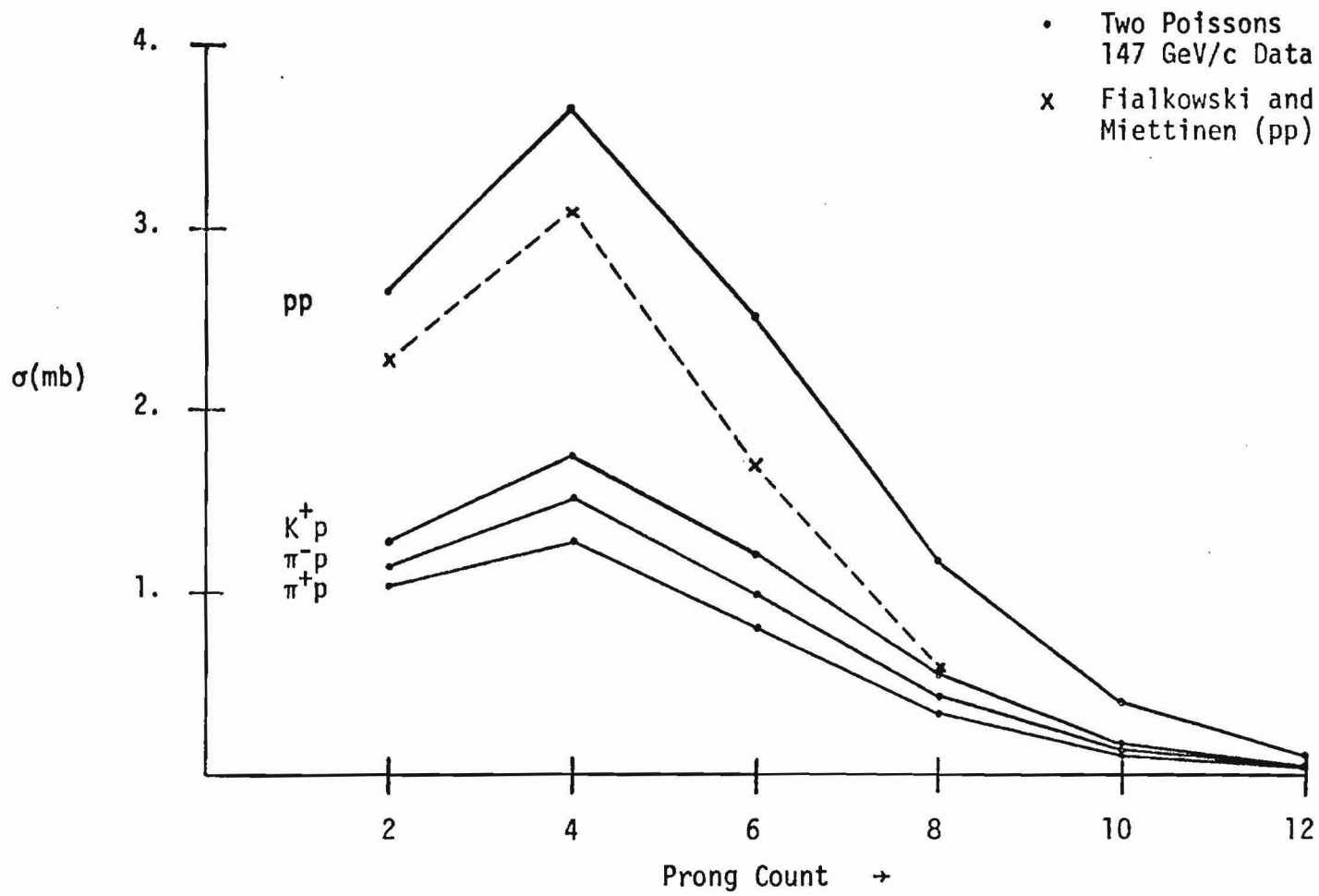

Fig. 43 - Low Multiplicity Component from Two Component Fits.

tive component.

All of these two component models made use of the assumption that diffractive cross sections are energy independent. Frazer and Snider (1973) pointed out that diffraction dissociation into high mass states (in the region dominated by the triple-pomeron diagram) would lead to logarithmically rising diffractive cross sections in the Fermilab-ISR energy range. They assumed that the diffractive multiplicity distribution at fixed M is given by a Poisson of average multiplicity $\langle N \rangle_{SRC} = A \ln M^2 + B$. The diffractive cross section $\frac{d\sigma}{dM^2}$ is known from the triple-pomeron diagram. Integrating over a diffractive mass range, $M_0^2 < M^2 < rs$, they found the high-mass diffractive multiplicity distribution was described by an incomplete gamma function. The average diffractive multiplicity was:

$$\langle N \rangle_{diff} = \tfrac{1}{2} \langle N \rangle_{SRC} + A \ln r$$

Using the averages from the two Poisson fits to the 147 GeV/c data:

$$A \ln r = -0.49$$

and, if $r \simeq .25$, one finds $A = .35$ for negative particles giving $A = 1.70$ for all charged particles. This is a reasonable result, especially since the effects of low mass diffraction were not explicitly taken into account in the Frazer and Snider formula.

B. Rapidity Gap Analysis

Diffractive final states in hadron-hadron or hadron-nucleus collisions are identified at high energy by striking kinematical differences from other inelastic processes. A quasi-elastically scattered target particle (beam particle) is accompanied by breakup of the beam particle (target particle).

When a single particle of mass M dissociates into several particles, they will have rapidities clustered about $y_c \cong \pm \frac{1}{2} \ln (s/M^2)$. The quasi-elastically scattered (recoil) particle has $y \cong \pm \frac{1}{2} \ln(s/m^2)$, and the rapidity gap between the cluster and the recoil particle will be

$$\Delta y = \frac{1}{2} \left(\ln \frac{s}{M^2} + \ln \frac{s}{m^2}\right) = \ln \left(\frac{s}{Mm}\right)$$

For $E = 147$ GeV, $s \cong 2ME = 276$, producing a gap of more than 4.6 units for $pp \to p\underline{X}$ for masses $M_{\underline{X}} \lesssim 3$ GeV. The gap between beam and target is $\Delta y \sim 5.7$ units for pp and $\Delta y \sim 7.7$ units for π^+p. The particles from the cluster will spread over a region in rapidity with a width dependent upon invariant mass. For a baryon cluster of $M \sim 3$ GeV/c^2, the spread can be up to 3 units and for a pion cluster $M \sim 3$ GeV/c^2 up to 5 units. The expected gap is $\gtrsim 4.6 - 1.5 \cong 3$ units for pp and $\gtrsim 6.5 - 2.5 = 4.0$ units for π^+p. For double diffraction (beam and target breakup) expected gaps are $\geq 4.6 - 3 \cong 1.6$ for pp and $\geq 6.5 - 5 \cong 1.5$ for π^+p.

The true identity of most final state particles in the hybrid system is unknown, and unidentified particles are assigned a pion mass. PEPR's ionization measurement allows separation of protons and pions with laboratory momenta less than 1.4 GeV/c. The number of fast protons is expected to be small with an incident pion beam. For proton beam, most of the fast positives with $x \geq .3$ are protons, since the x and y distributions must be symmetric in the CM frame. Mistaken identity implies:

$$y^{lab}_{p_{slow}} = \tfrac{1}{2}\ln\left(\frac{E+p_{11}}{E-p_{11}}\right) = \ln\left(\frac{E+p_{11}}{m_T}\right) \sim \emptyset$$ No shift (neglecting p_{11})

$$y^{lab}_{p_{fast}} = \ln\left(\frac{E+p_{11}}{m_T}\right) \sim \ln\left(\frac{2E}{m_T}\right)$$ May shift by 2 units

$$x^{CM}_{p_{slow}} = \frac{p^*_{11}}{\sqrt{s}} \sim -\frac{\gamma\beta E}{\sqrt{s}}$$ Shifts dramatically

$$x^{CM}_{p_{fast}} = \frac{p^*_{11}}{\sqrt{s}} \sim +\frac{\gamma\beta E}{\sqrt{s}}$$ No shift

For slow particles, clearly a large rapidity gap will remain large regardless of particle mass. For fast particles, a large gap in x will remain large.

Figures 44-49 show the single particle distributions in

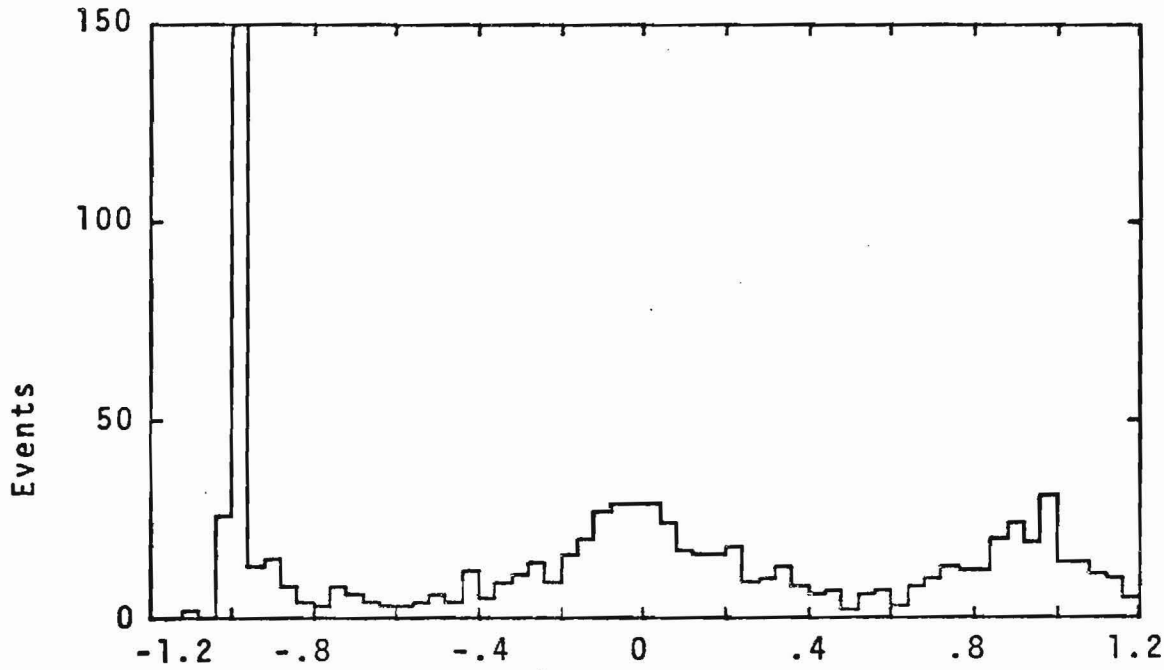

Fig. 44 2-Prong π^+p Events x →

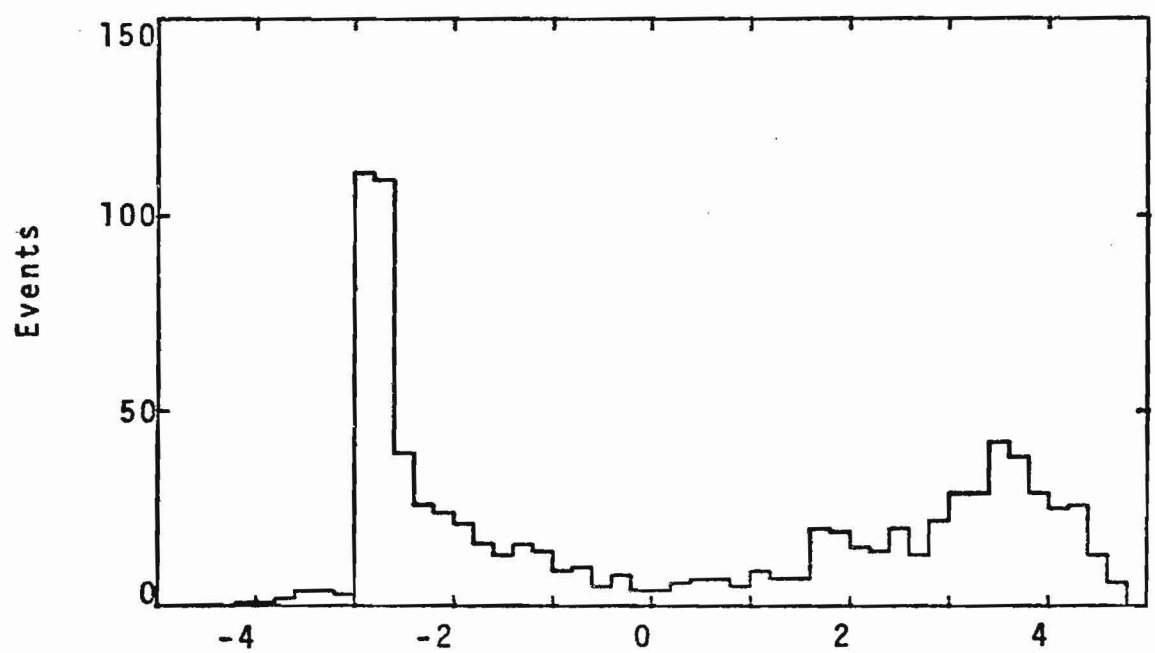

Fig. 45 2 -Prong π^+p Events y →

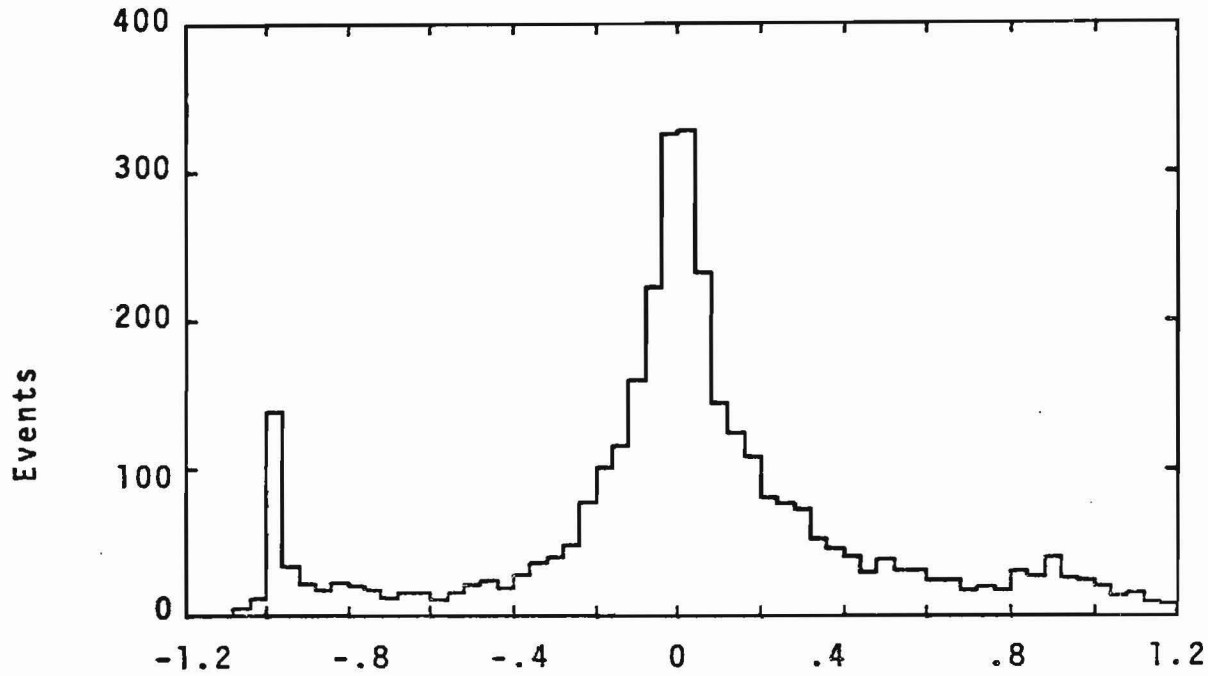

Fig. 46 4-Prong π^+p Events

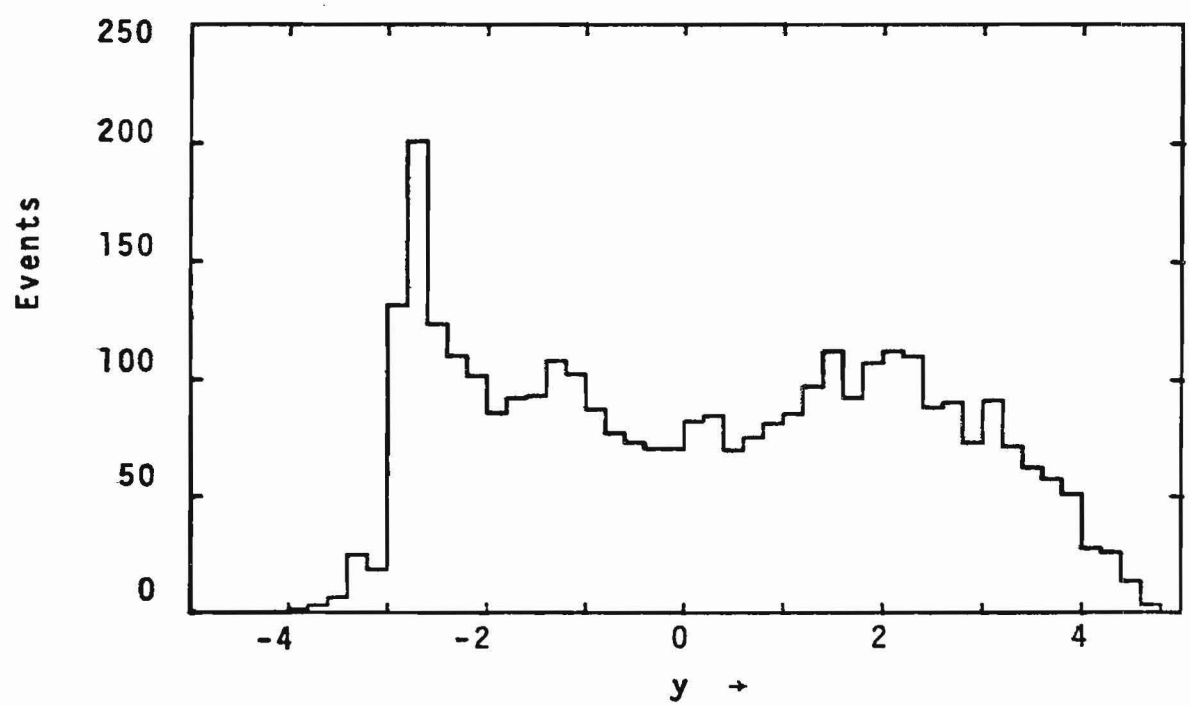

Fig. 47 4-Prong π^+p Events

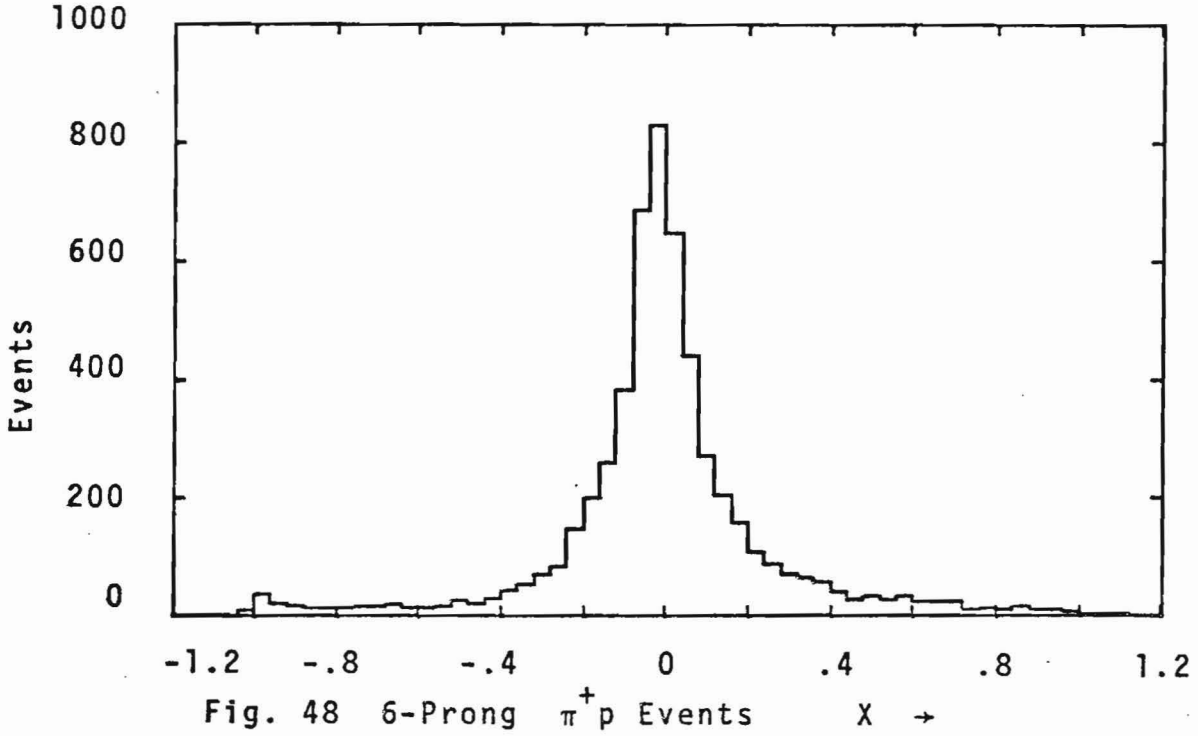

Fig. 48 6-Prong π^+p Events

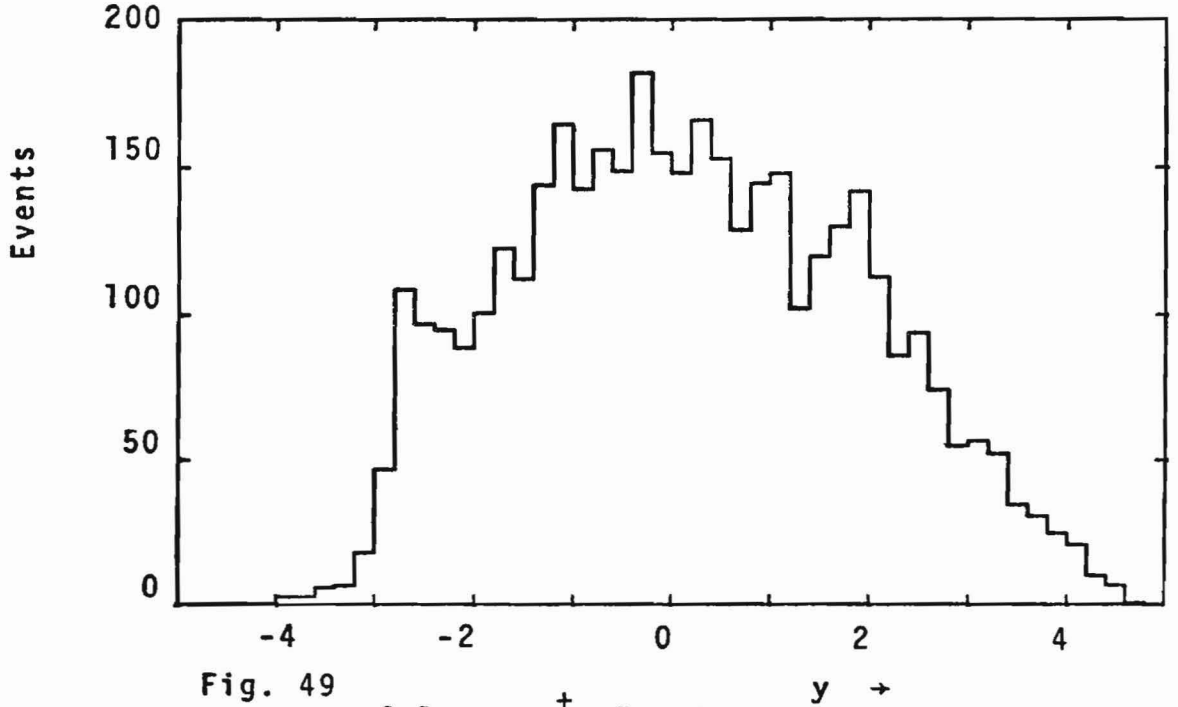

Fig. 49 6-Prong π^+p Events

x and y for charged particles in 2, 4, and 6 prong events. Clear leading particle peaks are seen in the 2-prong and 4-prong events, but not in the events with ≥ 6 prongs.

The following discussion is restricted to rapidity gaps between charged particles. The 2-prongs have a single gap for which the distribution is shown in Figure 50. The average gap is very large, suggesting the dominant role of diffractive processes. In the 4-prongs, the shape of the largest-gap distribution resembles that of the 2-prongs, although the average is considerably smaller (Fig. 51).

The multiperipheral model predicted (DeTar, 1971) that at high energies:

1) a uniform single particle distribution of constant height in rapidity develops, which expands $\propto \ln s$.
2) the number of produced pions is given by a Poisson distribution.

However, when Fermilab energies were reached, the single-particle inelastic rapidity distributions showed no evidence of a central plateau. Indeed, ISR data indicated that the cross sections at $y = 0$ were actually rising slowly with s. As we have seen, however, the bulk of the high multiplicity events do seem to follow a Poisson distribution in the number of produced negatives with the average rising as $\ln s$. Such reasoning opened the way for the two-component models which combined a

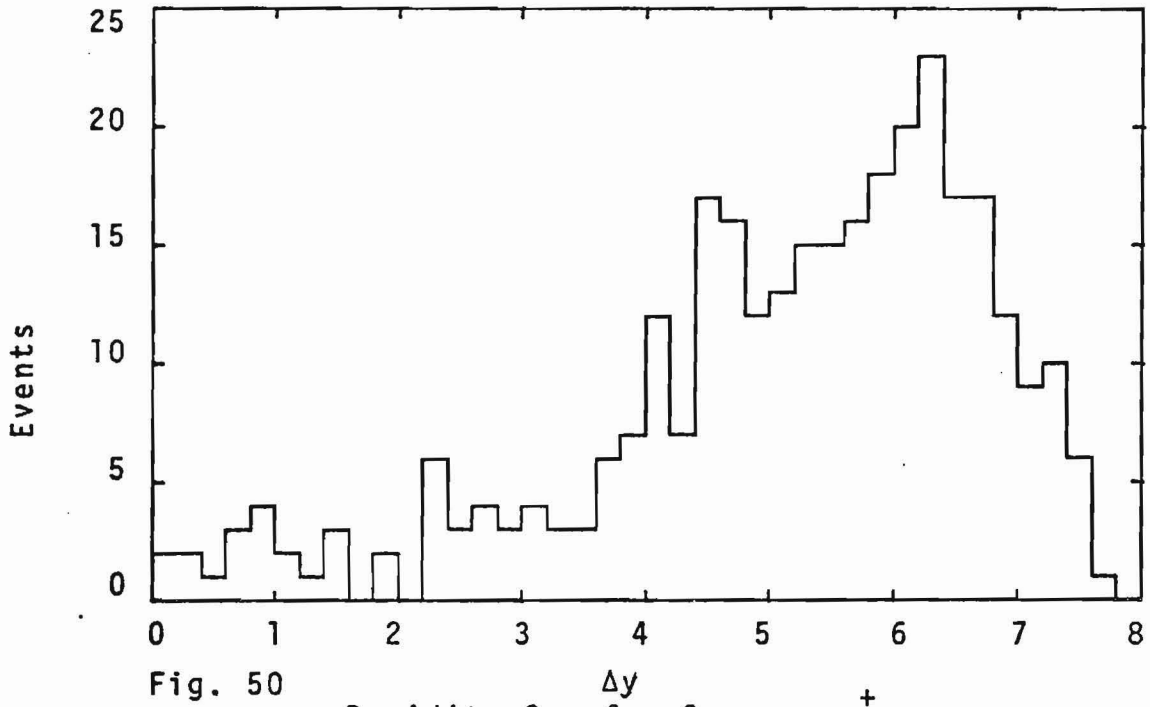

Fig. 50 Rapidity Gap for 2-prong π^+p

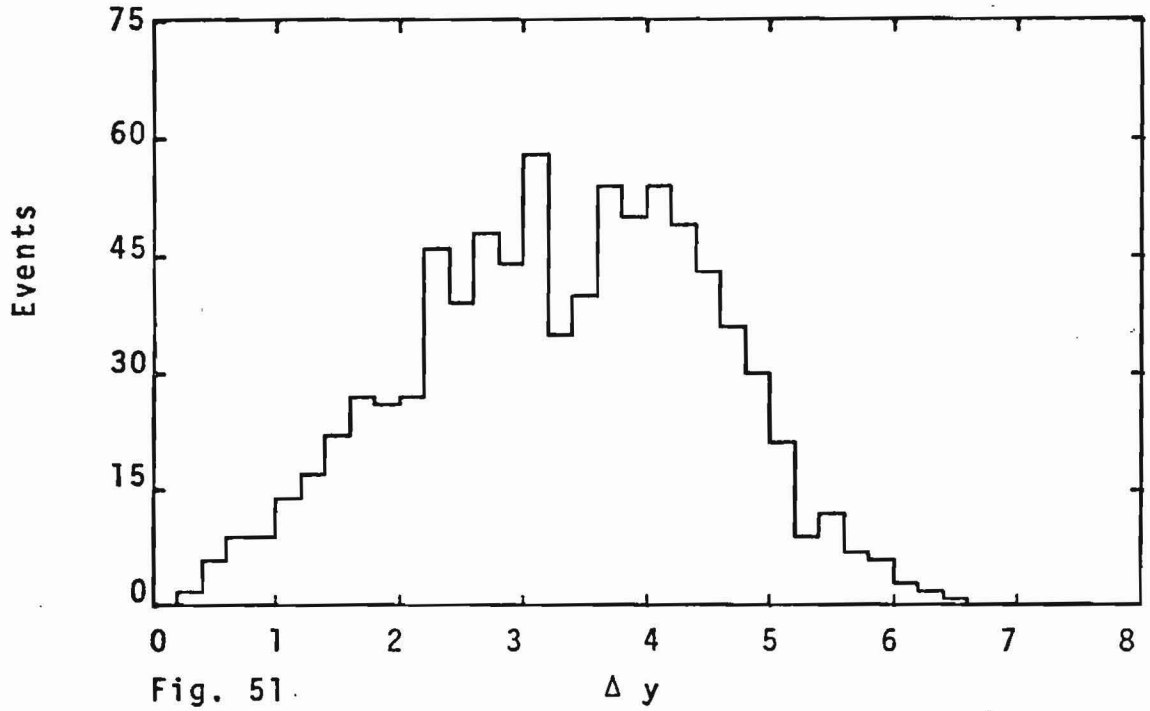

Fig. 51 Largest Rapidity Gap for 4-prong π^+p

diffractive low multiplicity component and a multiperipheral process for the higher multiplicity component. Perhaps the absence of a rapidity plateau is due only to energy-momentum conservation effects, i.e. non-zero p_T , and still higher energies are needed to observe plateaus. The gap in rapidity between two charged particles should be distributed uniformly also, if the particles follow a uniform distribution in y. Diffractive events, on the other hand, are expected to contain a large rapidity gap between the beam and target clusters. The leading particle peaks in the low multiplicity events are interpreted as diffractive events in which the beam, or target, remains intact.

Gap distributions may be investigated in the following manner:

1) order the particles in rapidity (y_i , i = 1, N)
2) calculate the gap between adjacent particles ($\Delta y_i = y_i - y_{i+1}$, $^{i=1,\ N-1}$)
3) order the gaps according to size of the gap.

One can then histogram the position of the largest gap as a function of gap location.

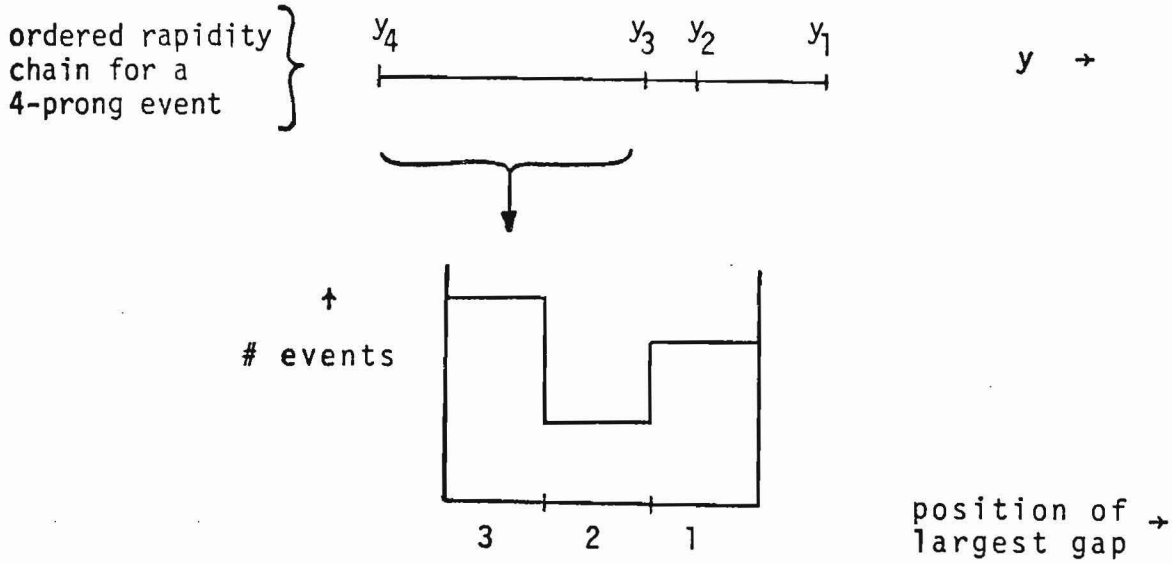

Figures 52 and 53 show the results of this procedure for 4-12 prong events.

Most frequently, one finds an end gap in the rapidity chain is the largest gap in the event. In this case, the charge of the end particle is most frequently the same as the incident charge. If we accept the premise that, at very high energies, Pomeron exchange dominates, it is tempting to assign at least part of this "leading particle" effect to high mass diffraction. The size of the gaps may also be examined. Figure 54 shows the average size of the largest gap, second-largest gap, ..., fifth-largest gap as a function of prong count. These

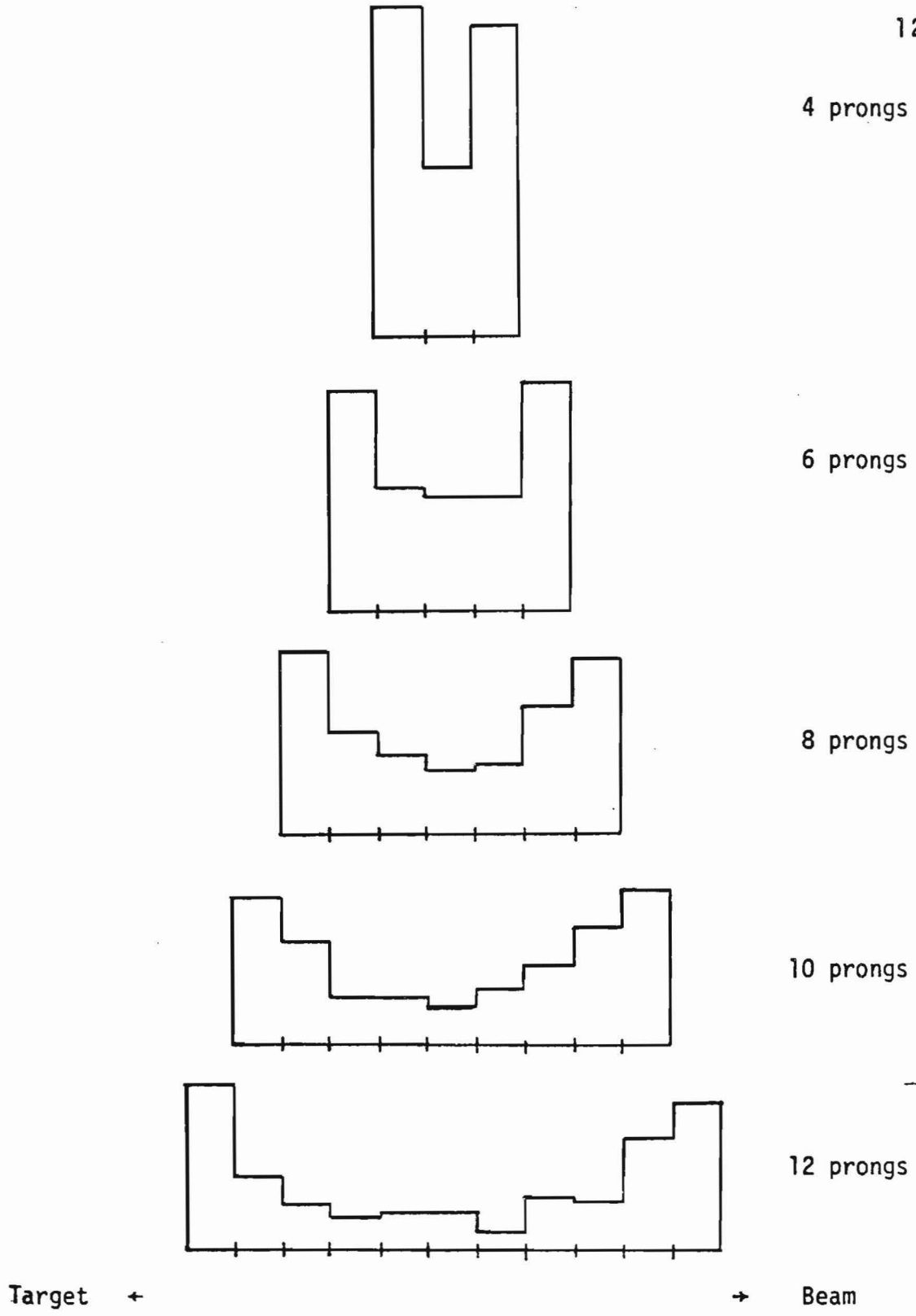

Fig. 52 - Location of largest Rapidity Gap in pp events.

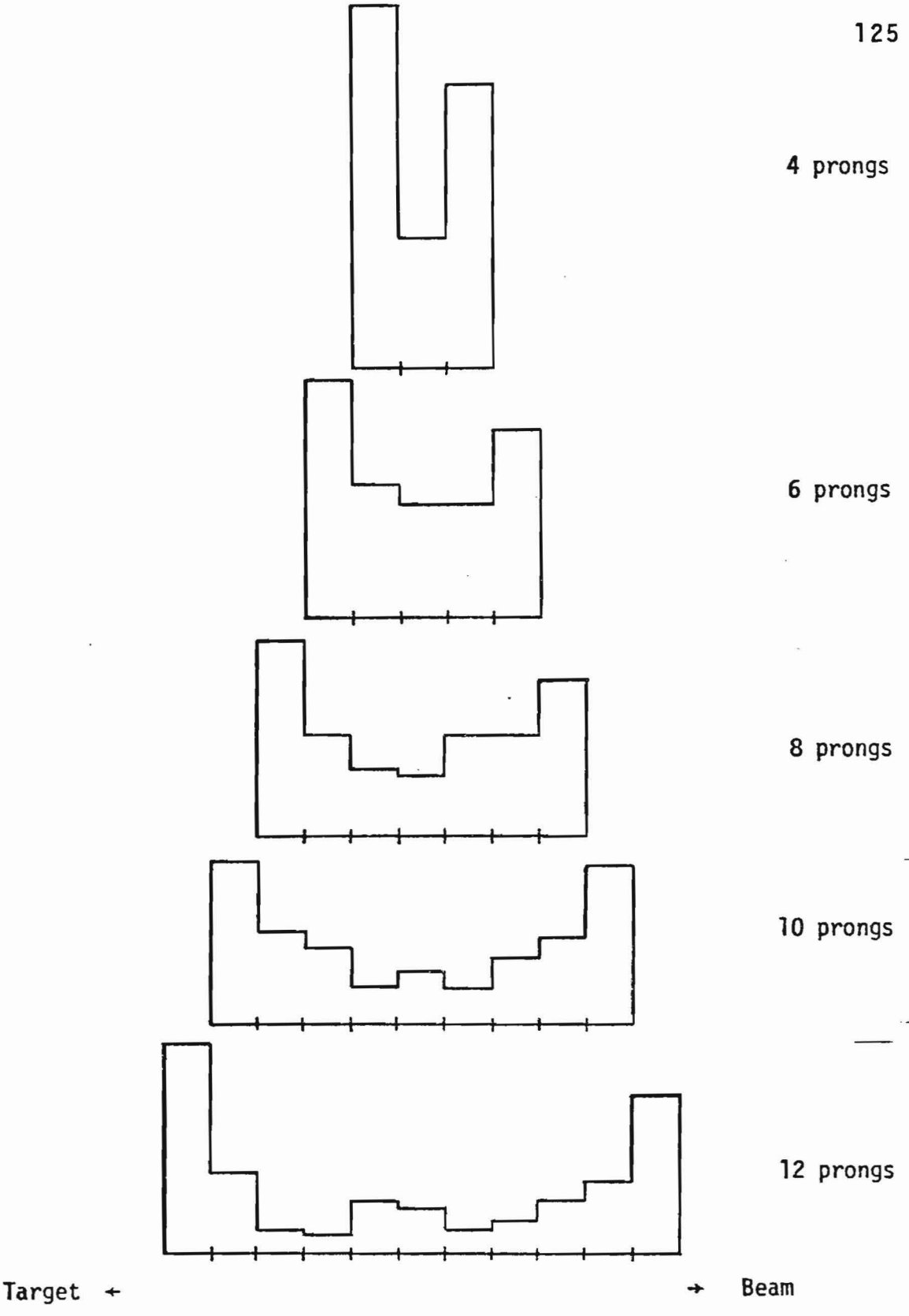

Fig. 53 - Location of largest Rapidity Gap in π^+p events.

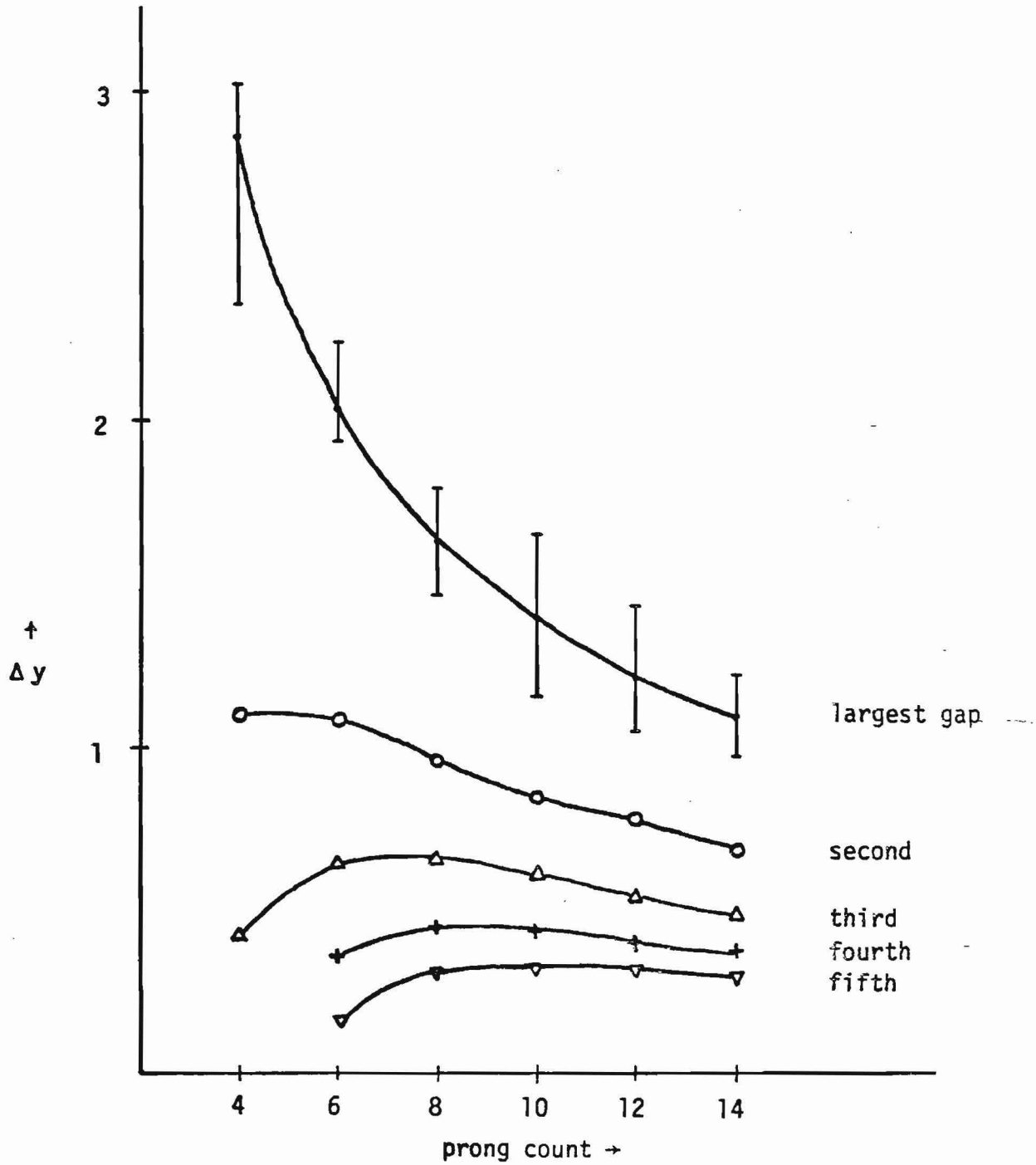

Fig. 54 - Average Rapidity Gap Size for Proton-Proton Events.

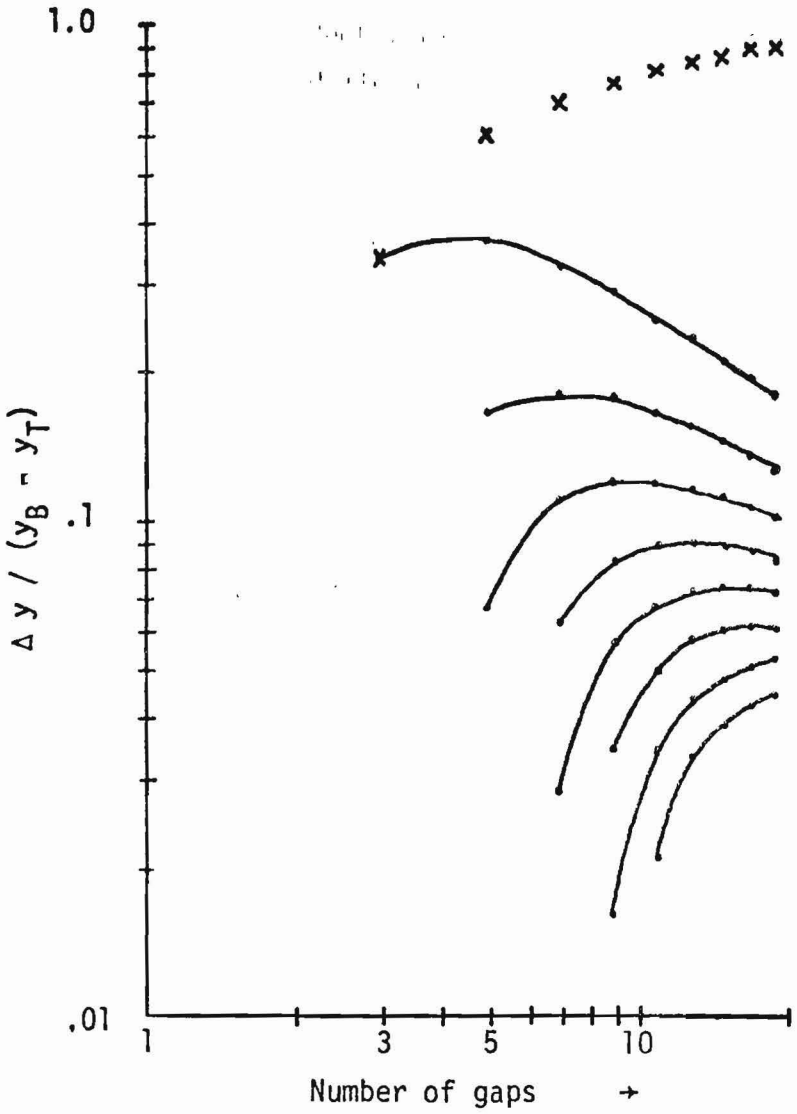

Fig. 55 - Uniform Distribution

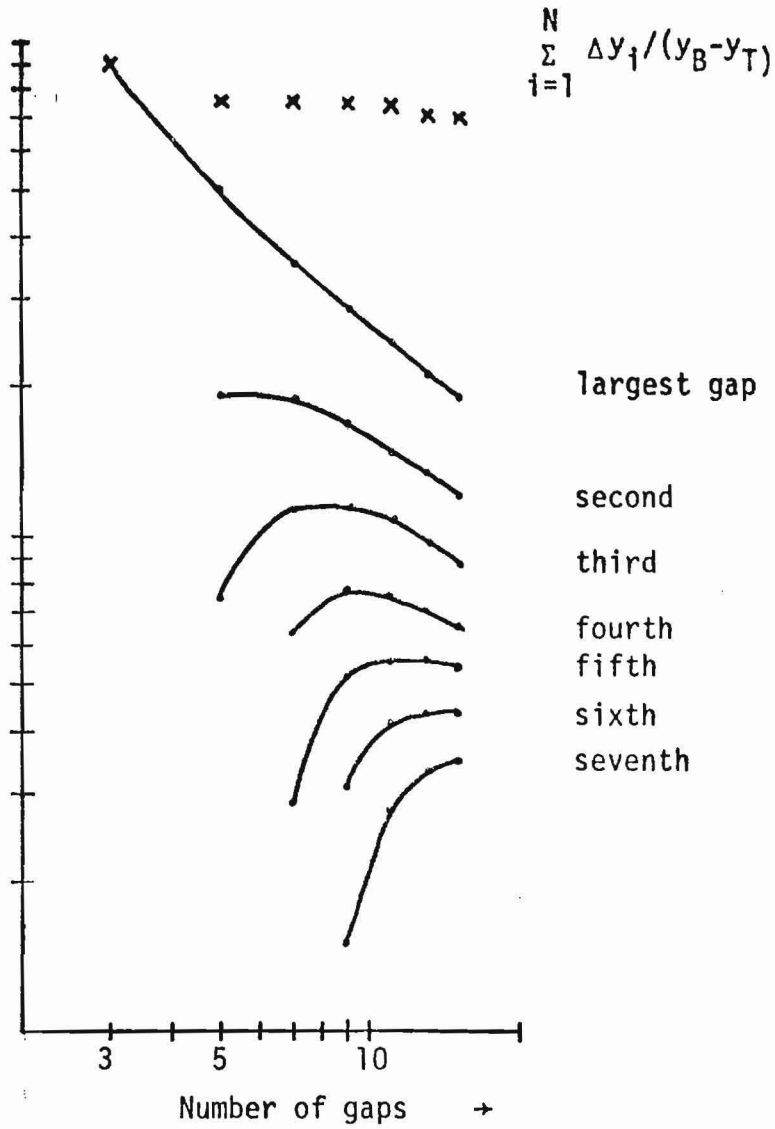

Fig. 56 - Proton-proton Events

(Amaldi, Jacob, and Matthiae, 1976):

$$P_{lab} \gtrsim 2.5 \quad (M^2 - m^2)$$

At P_{lab} = 147 GeV/c, the maximum value of M is 7.7 GeV/c^2. This corresponds to a Feynman $x \gtrsim .78$. An event was classified as diffractive if:

1) the largest rapidity gap occurred next to the first or last particle on the ordered rapidity chain,
2) $|x| \geq .75$ for the end particle next to the largest rapidity gap.

Figure 57 compares the results obtained by this rapidity gap selection procedure with normalized Poisson distribution of the same average N_- .

Table XIII contains the topological cross sections for the selected diffractive component for π^+p and pp reactions. When the proton identification criteria used in this experiment were applied to the 147 GeV/c π^-p data (which had complete ionization information for tracks with momenta $\leq$ 1.4 GeV/c), the number of leading protons near x= -1 increased substantially. A correction factor was applied to the π^+p data for each topology to account for this effect. When the same factors were applied to the pp data, the number of beam breakup events was found to be 10% less than the number of target breakup events.

Figures 58 and 59 show a comparison of this component with the total inelastic distribution for pp and π^+p, and to the distribution of events with largest rapidity gaps at the ends of the ordered y-chain.

The cross sections for π^+ breakup and proton breakup may be compared:

$$\frac{\sigma(\pi^+p \rightarrow \pi^+X)}{\sigma(pp \rightarrow pX)} = .52$$

$$\frac{\sigma(\pi^+p \rightarrow Xp)}{\sigma(pp \rightarrow Xp)} = .59$$

The first ratio is predicted by factorization to be equal to the ratio of the π^+p and pp elastic cross sections ($\approx$ .49). The second ratio was found to be .61 before the ionization correction was done. These values are quite close to the ratio of the π^+p and pp total cross sections ($\approx$.60).

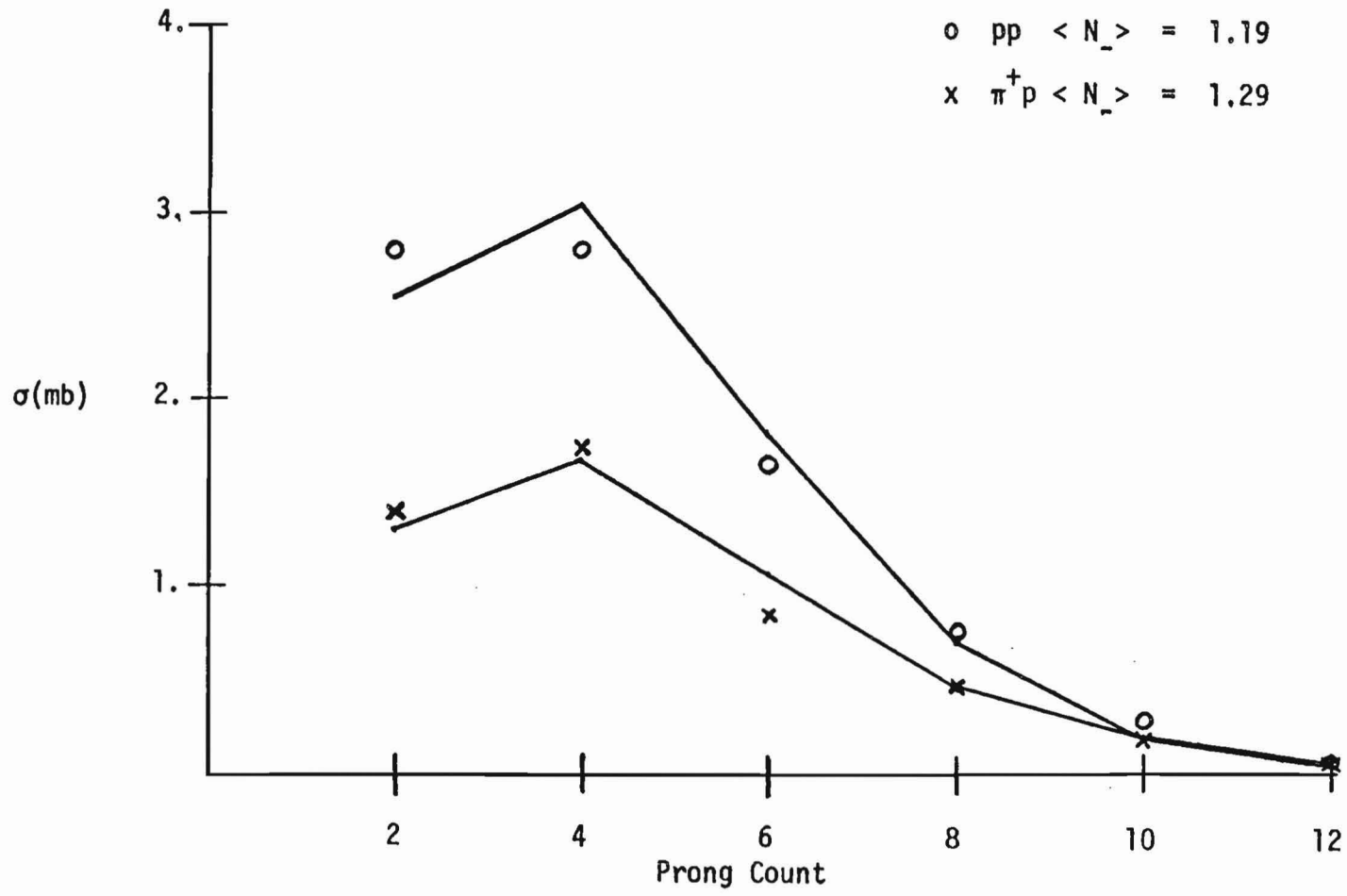

Fig. 57 - Topological cross sections for the diffractive π^+p and pp events.

TABLE XIII

DIFFRACTIVE CROSS SECTIONS (END GAP LARGEST, $|X|>.75$)

π^+p Topology	Target Breakup	Corrected Beam Breakup	Sum
2	.674	.726	1.40
4	.830	.889	1.719
6	.377	.476	.853
8	.273	.210	.483
10	.109	.093	.202
12	.054	.010	.064
14	.024	----	.024
	2.341	2.404	4.745

$\langle N_- \rangle = 1.29$

$= .76$ if elastics are included

pp Topology	Target Breakup	Corrected Beam Breakup	Sum
2	1.346	1.454	2.80
4	1.441	1.360	2.801
6	.924	.719	1.643
8	.439	.324	.763
10	.206	.094	.300
12	.056	.015	.071
	4.412	3.966	8.378

$\langle N_- \rangle = 1.19$

$= .65$ if elastics are included

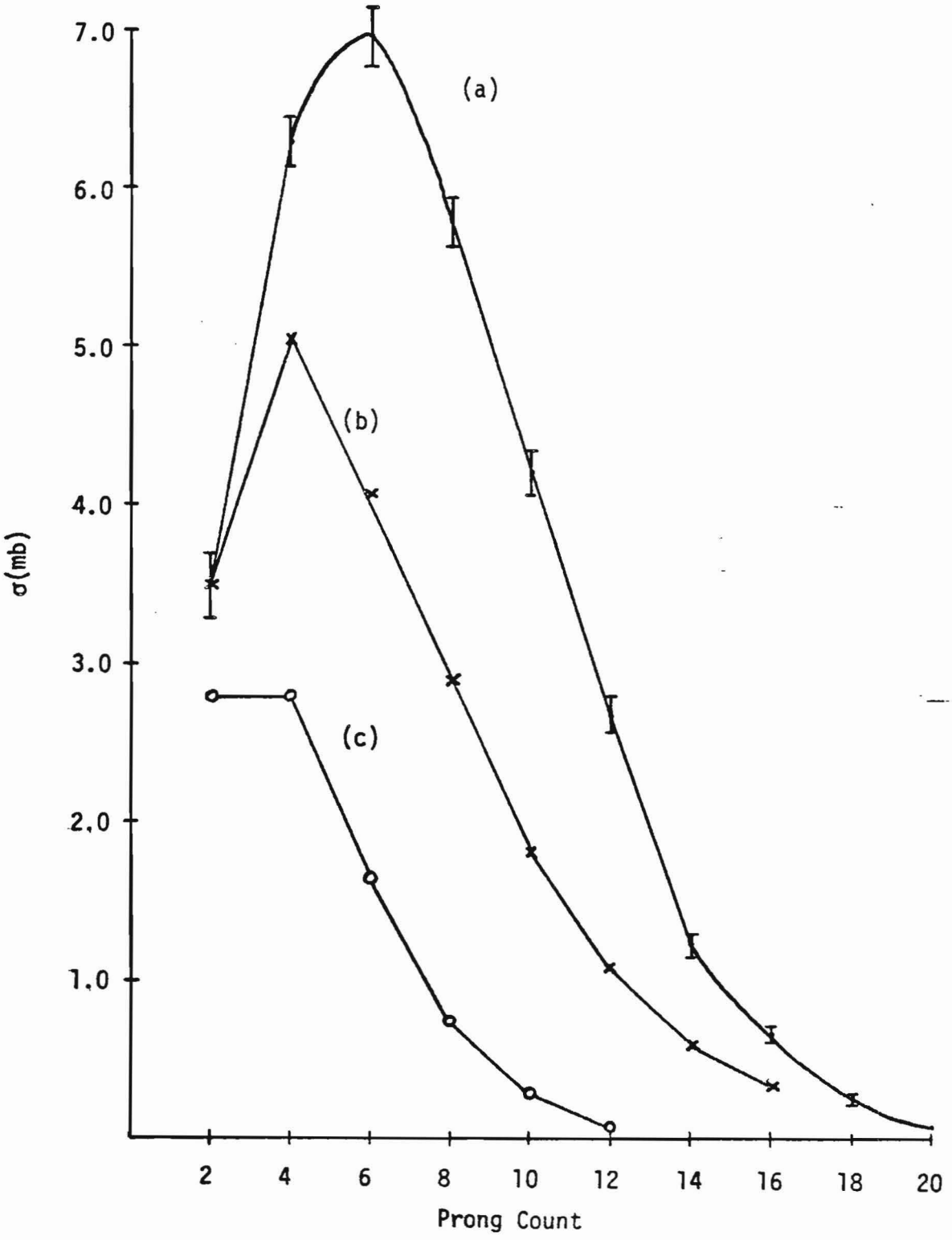

Fig. 58 - Multiplicity Distributions for proton-proton events.

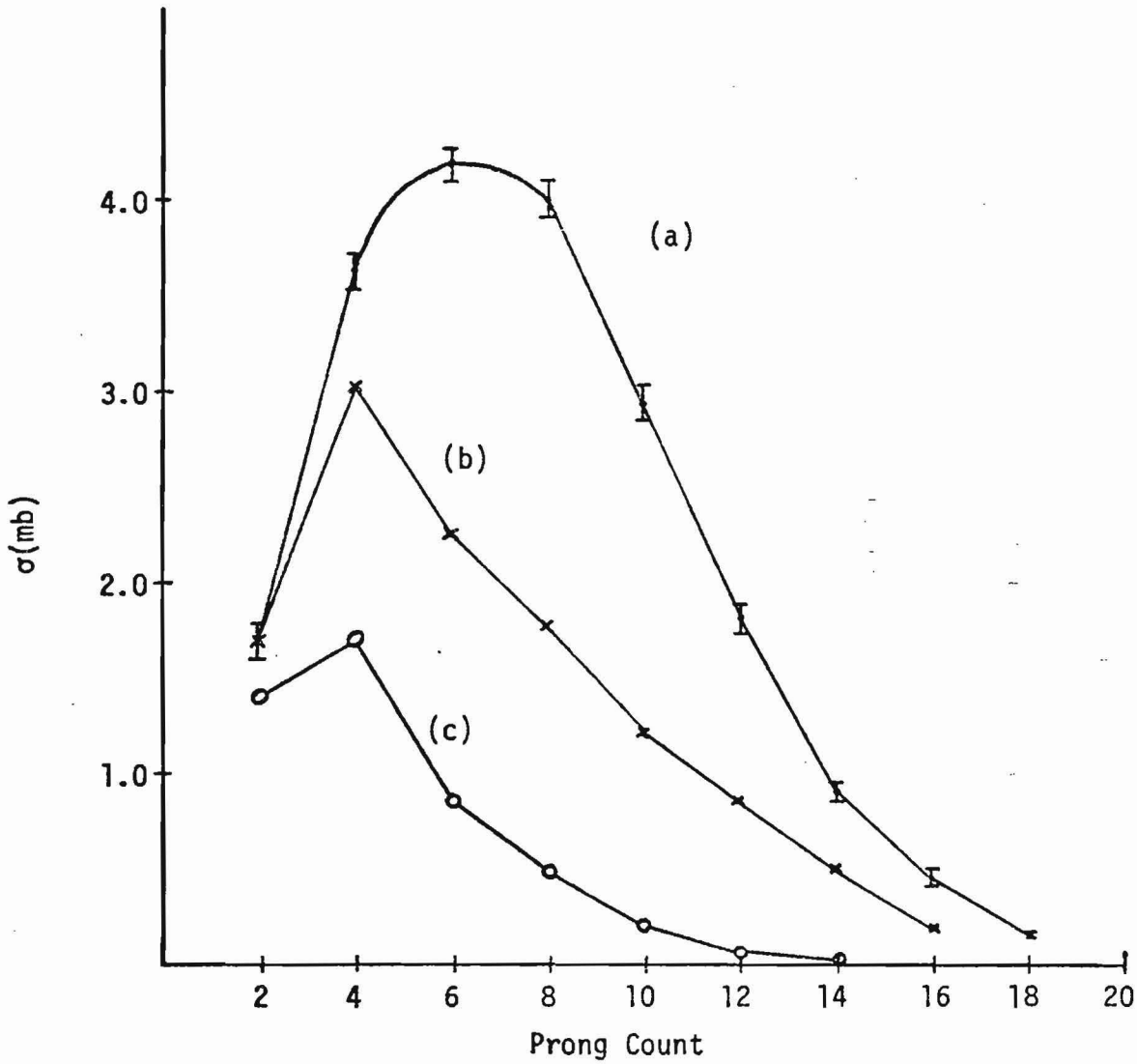

Fig. 59 - Multiplicity Distributions for π^+p events.

C. Inclusive Charged Particle Spectra

1) Charged particle distributions

Figures 60 - 62 present weighted, inclusive $\frac{d\sigma}{dx}$ distributions for all positive particles, all negative particles, and identified protons from inelastic proton-proton events. Protons were identified by ionization, when available, or else through use of the criteria previously discussed. All other particles were assigned a pion mass, unless scanning information indicated otherwise. The figures have not been corrected for experimental resolution; the forward leading particle peak appears to extend considerably beyond the physical limit at $x = 1$. Assignment of a proton mass to positive particles with $x > .5$ causes a negligible change in x. Figures 63-65 present the corresponding $\frac{d\sigma}{dx}$ distributions for π^+ - protons events. A small left-right asymmetry near $x = 0$ is evident in $\frac{d\sigma}{dx}$ for proton-proton events. This is due to limited hybrid spectrometer acceptance for tracks of relatively low momentum which are, however, fast enough to make charge identification difficult in the bubble chamber. The result is biased loss of events having secondary tracks of momentum ~ 8-20 GeV (see figures 6 and 9). The x-distribution of negatives from proton-proton events shows a rapid increase in the degree of asymmetry as a function of prong count.

The most striking feature of the x-distributions of positive particles is the sharp peak near $x = -1$. The corresponding forward peak near $x = +1$ has been smeared by the spectro-

meter resolution, however, a distinct shoulder is still evident. These leading particle peaks have been interpreted as clear signals of diffractive scattering.

A convenient comparison of π^+- proton and proton-proton events can be made by normalizing the x-distributions to the respective total inelastic cross sections, $\frac{1}{\sigma_{inel}} \cdot \frac{d\sigma}{dx}$. Figure 66 gives the result for negative particles. Considerably more fast negatives with $x > 0$ are seen in the π^+ -proton events. Figure 67 presents the positive particle comparison. It is interesting to note that the good agreement of the π^+p and pp data in the region $-.9 \lesssim x \lesssim -.1$. Mueller-Regge analysis (1970) predicts such limiting fragmentation at high energy. In the forward direction near $x = +1$, we see the π^+ leading particle peak is smaller than the proton peak. This may be expected from factorization (refer to introduction), which requires that the quasi-elastic cross section ratio for π^+- proton and proton-proton events should be equal to the ratio of the elastic cross sections ($\simeq .49$) rather than the inelastic cross section ratio ($\simeq .63$). The apparent equality of the leading proton peaks near $x = -1$ is unexpected. This disagrees with the ratio (~ 1.3) for π^--proton and proton-proton data at 205 GeV/c (Winkelmann, 1974). The size of the leading proton peak at $x = -1$ is sensitive to errors in proton identification. The peak might also be spuriously large if some elastic events were mistakenly included in the inelastic

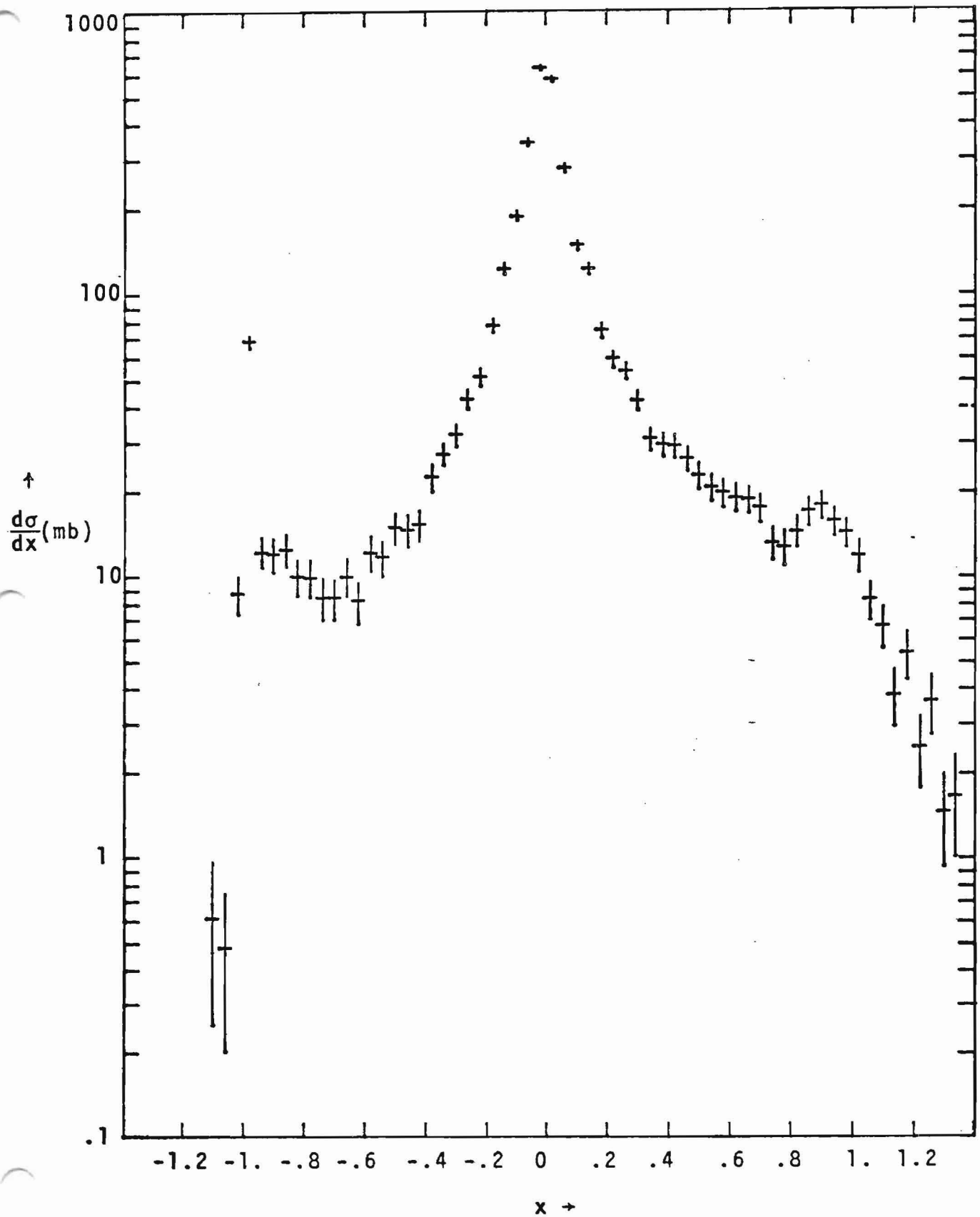

Fig. 60 - Positives from proton-proton inelastic events

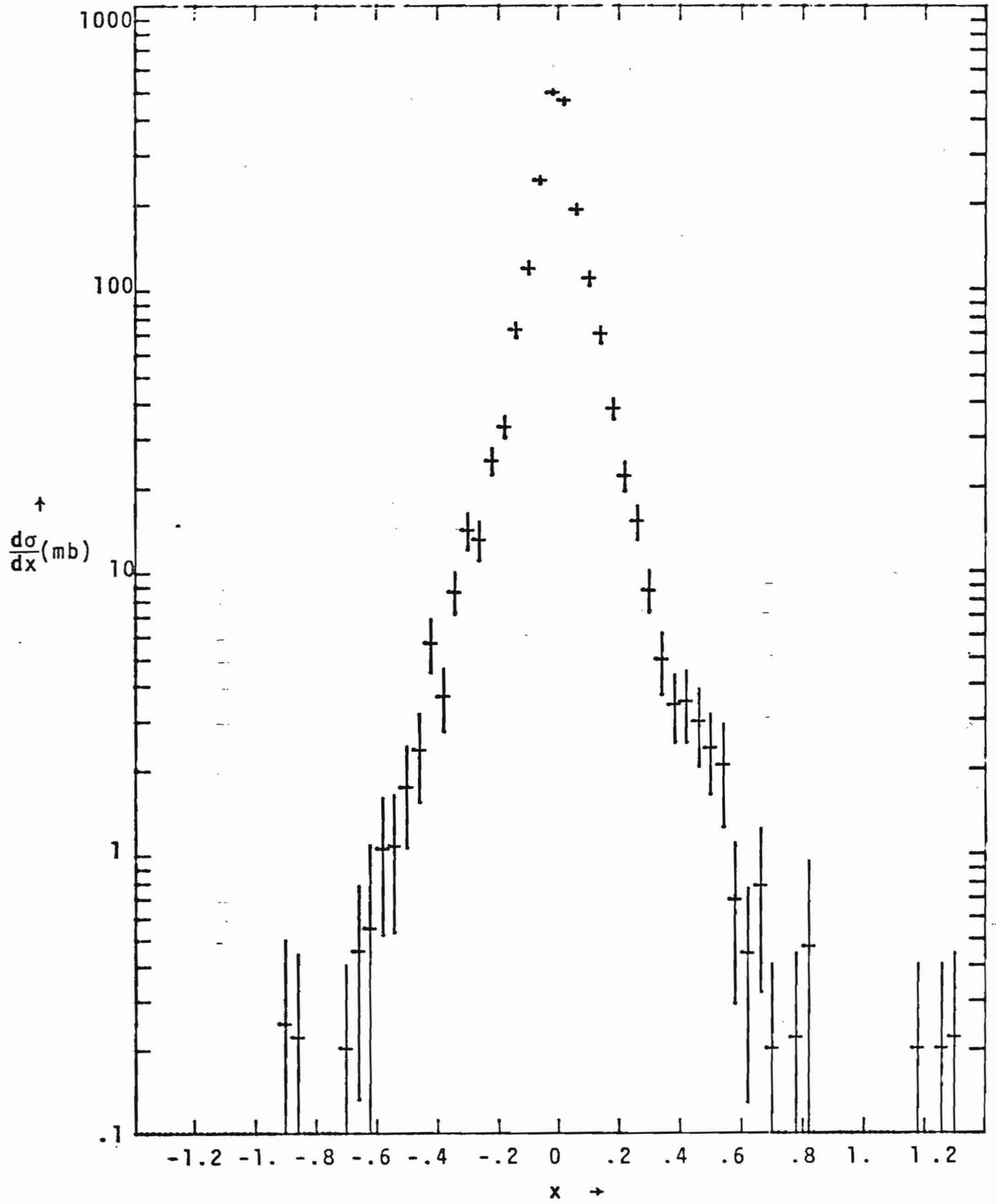

Fig. 61 - Negatives from proton-proton inelastic events.

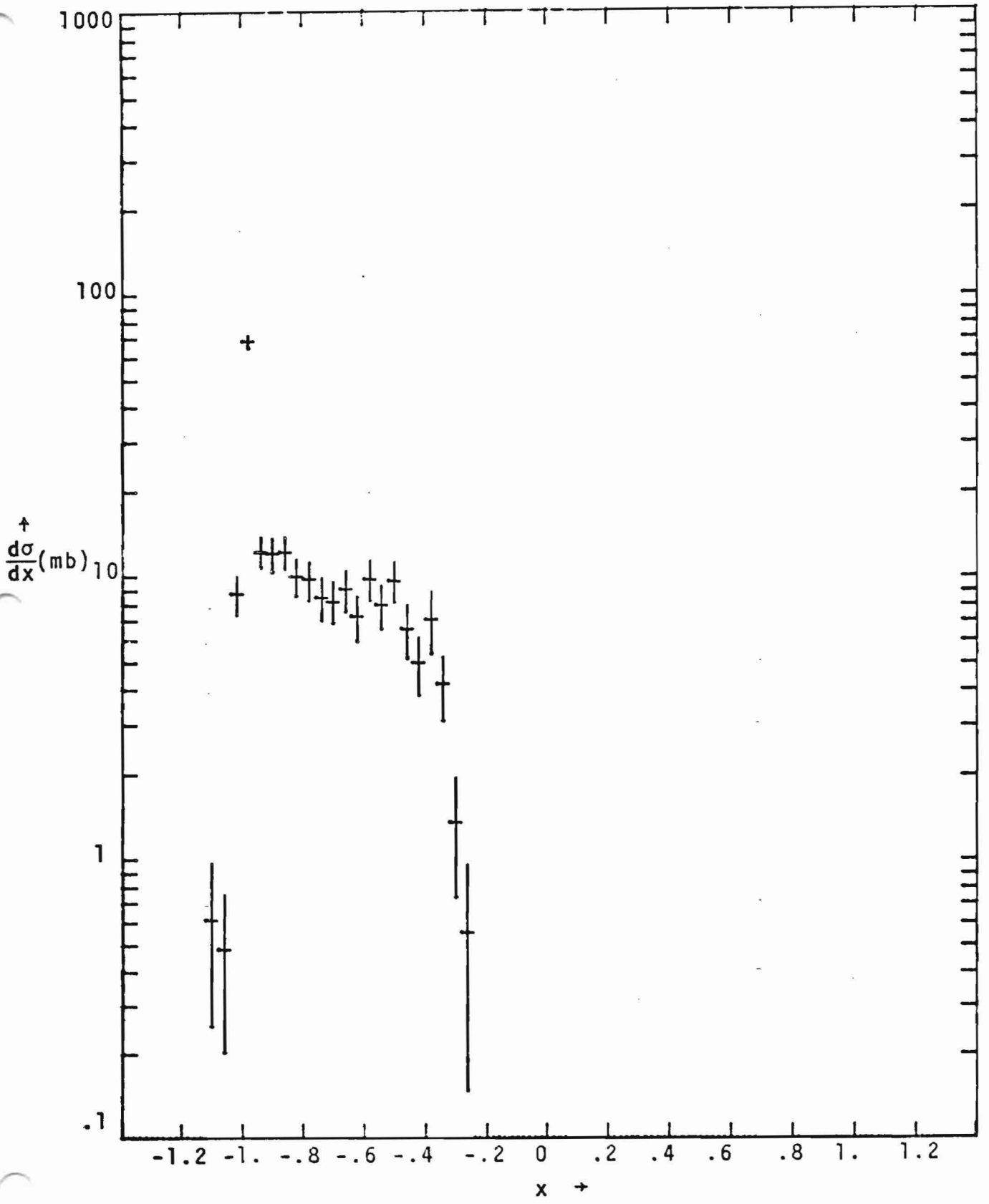

Fig. 62 - Identified protons from proton-proton inelastic events

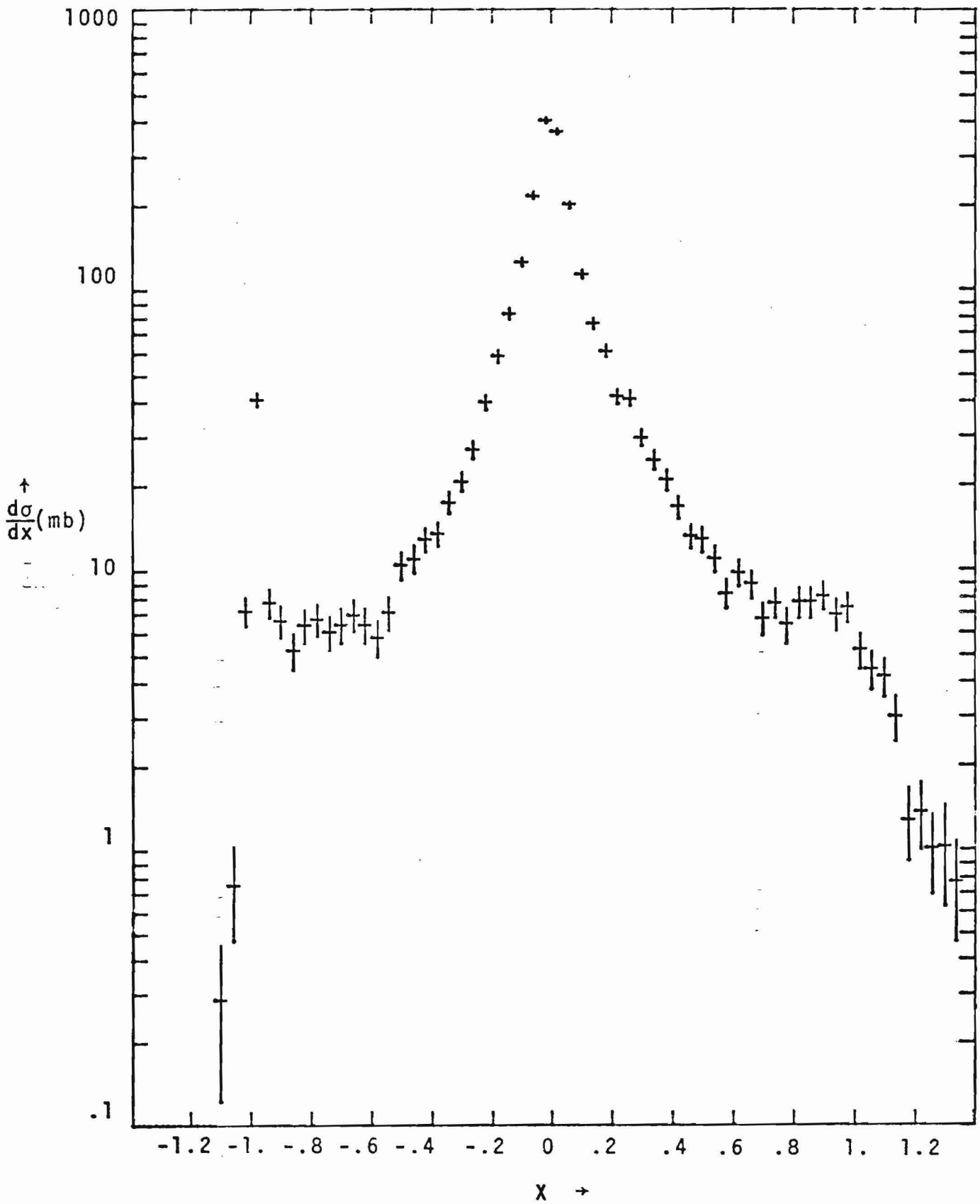

Fig. 63 - Positives from π^+ - proton inelastic events

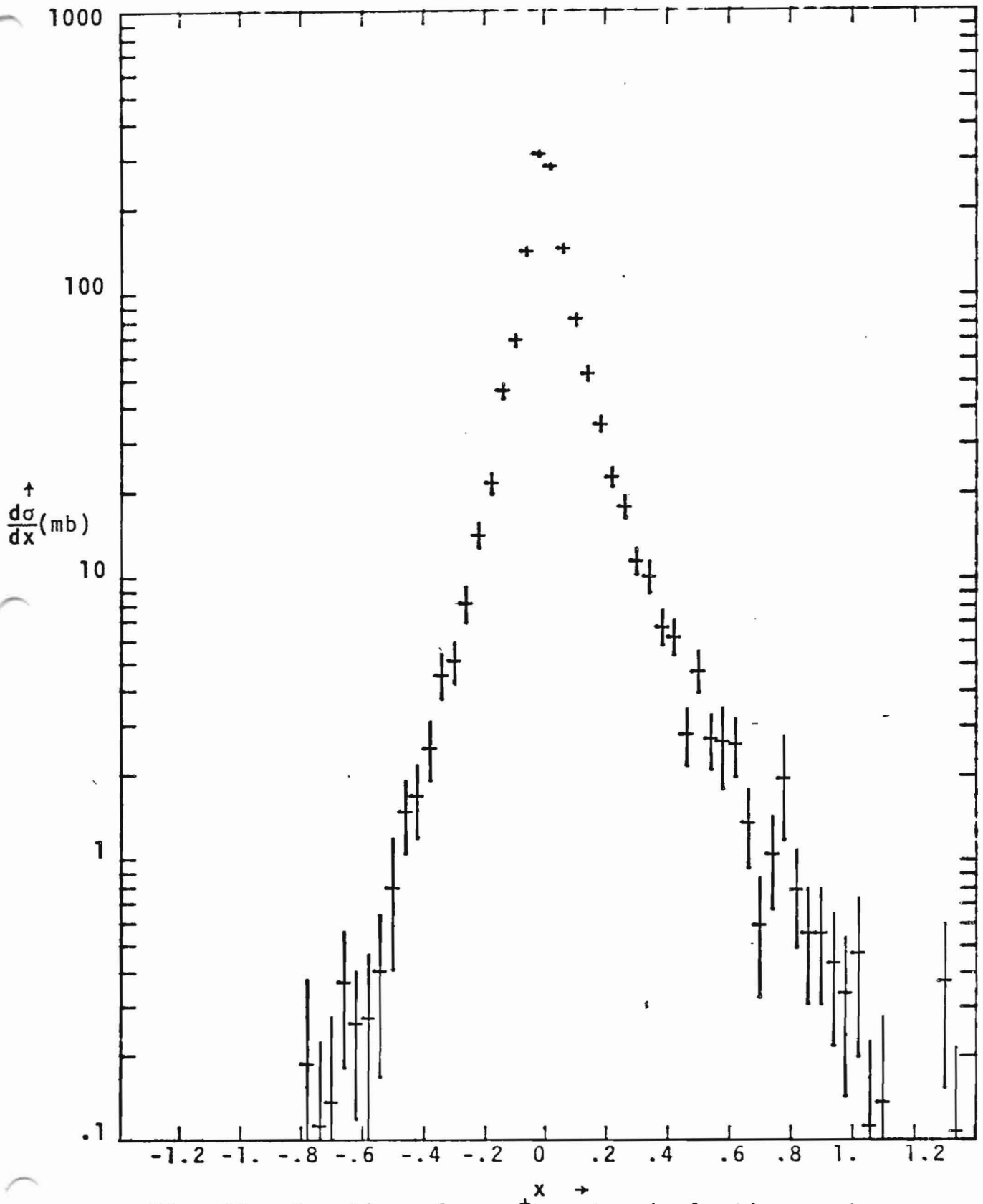

Fig. 64 - Negatives from π^+-proton inelastic events

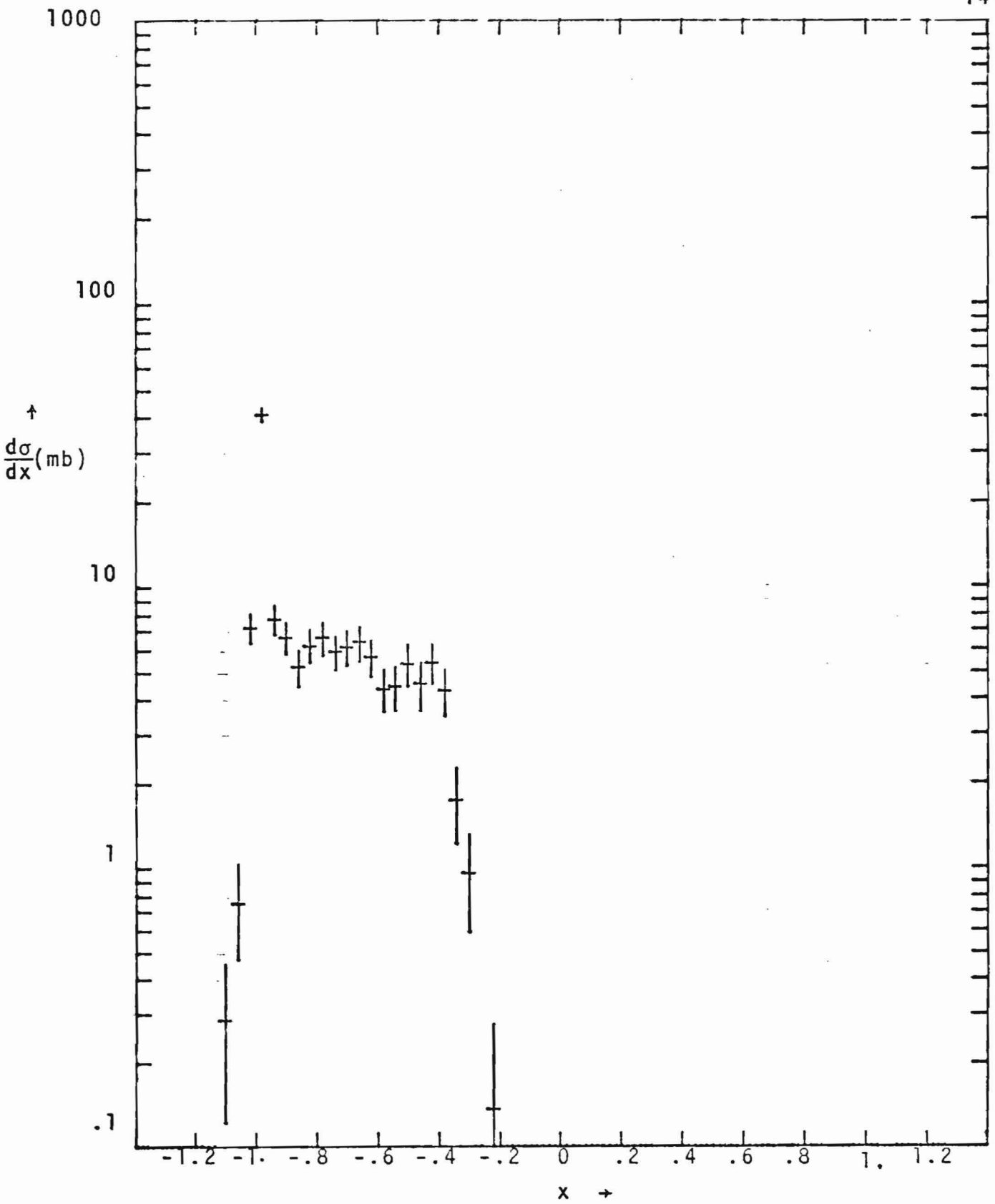

Fig. 65 - Identified protons from π^+-proton inelastic events

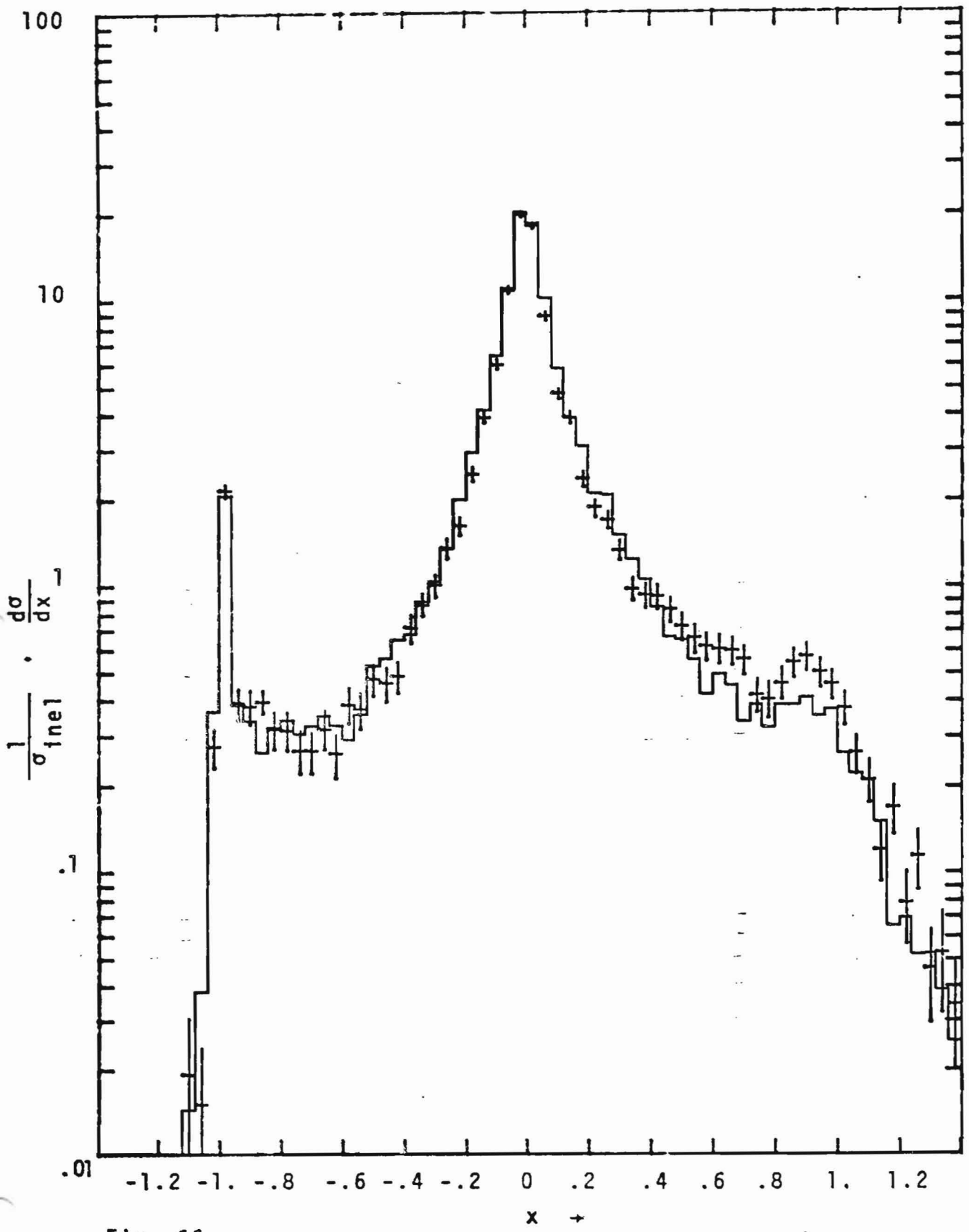

Fig. 66 - Comparison of positives from pp and π^+p events.

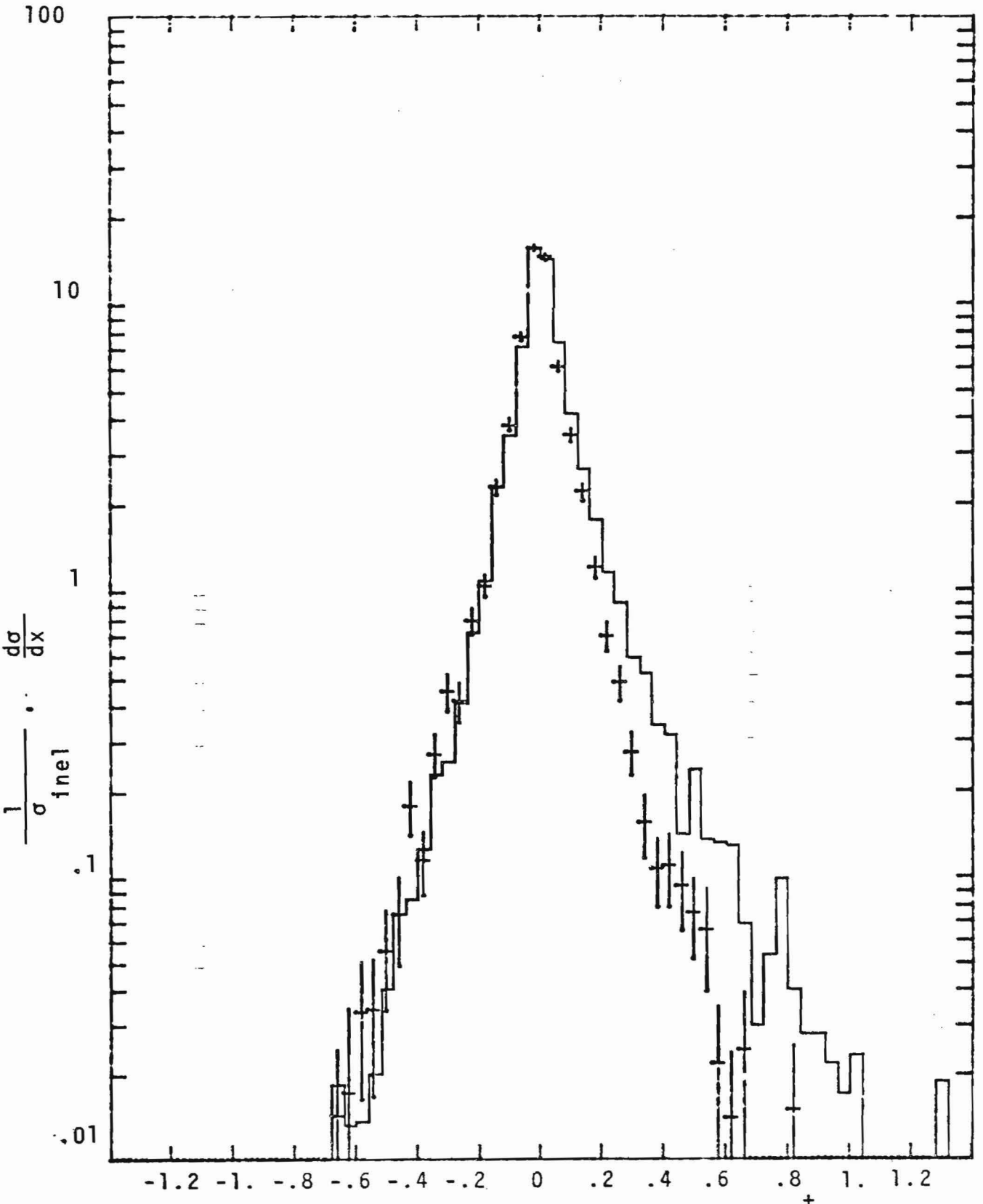

Fig. 67 - Comparison of negatives from pp and π^+p events.

sample. Each of these errors is estimated to be of the order of 10%; refer to the discussion in section VI-A. It should be noted that both the π^+-proton and proton-proton data were taken at the same time during this experiment, and that the processing, proton identification, and elastic separation were performed identically for the two reactions.

Figures 68 -73 present x and y distributions for charged particles in 4-prong proton-proton events using the rapidity gap separation technique. In this case, there are three gaps between charged particles: Figures 68 and 69 contain events with the largest y-gap next to the target; figures 70 and 71 have the largest y-gap in the center; and figures 72 and 73 have the largest y-gap next to the beam. Figures 74 - 79 are the corresponding ones when the additional requirement that $|X|>.75$ is imposed for leading particles. The distributions for 6 and 8 prong events are quite similar except for smaller leading particle peaks and somewhat more compact fragmentation distributions.

2) Neutral pion distributions

If one assumes that the majority of gammas come from π^0 decays, as the $2-\gamma$ invariant mass distributions indicate, the π^0 distribution $\frac{dN}{dx}$, or $\frac{dN}{dE}$, may be obtained from the observed shower x-distribution. The observed x-distribution of showers from π^0 decay, g(x), may be written:

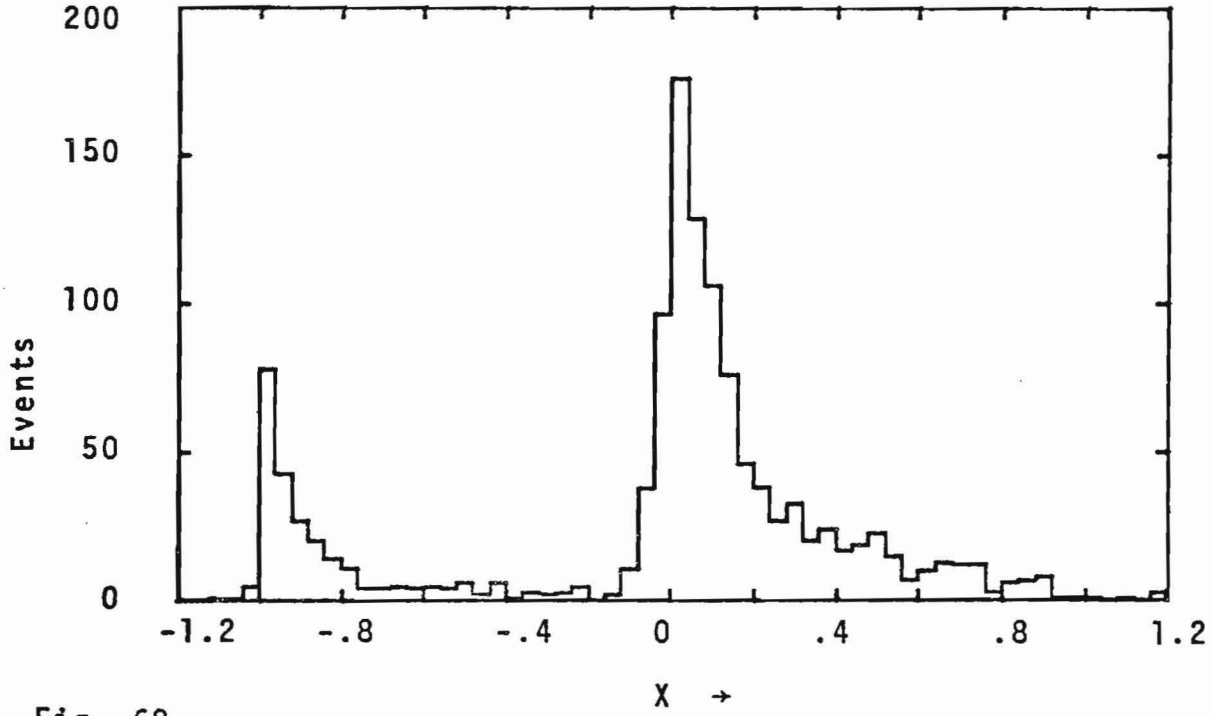

Fig. 68

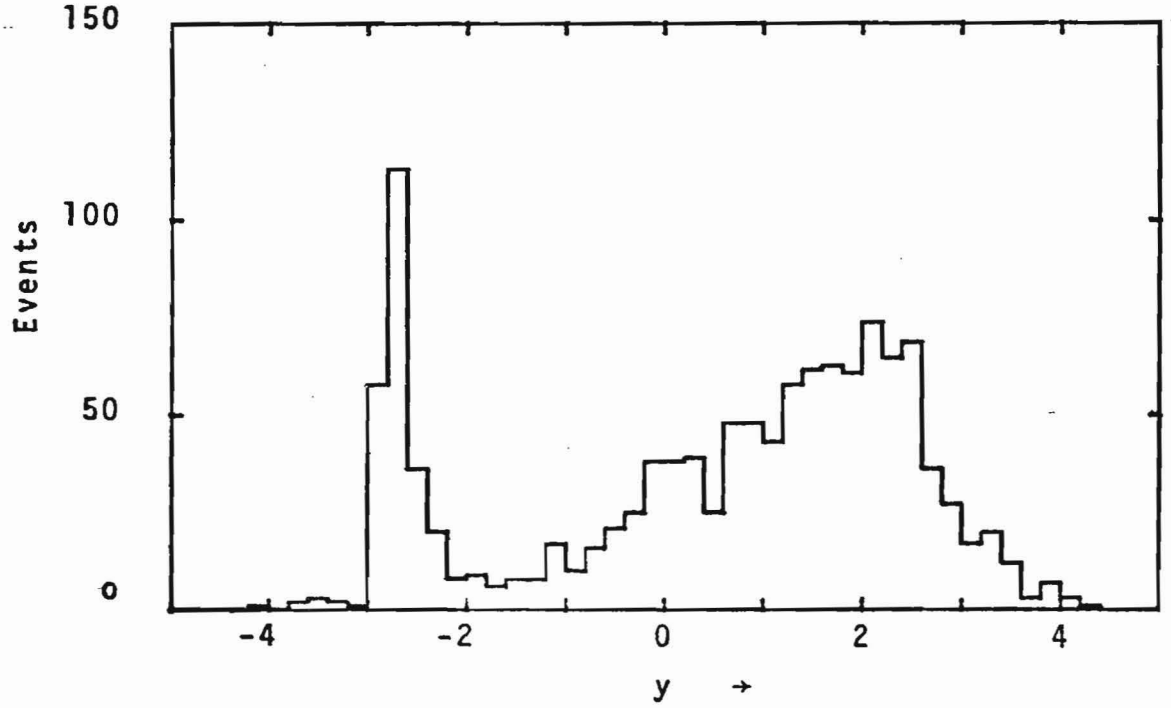

Fig. 69

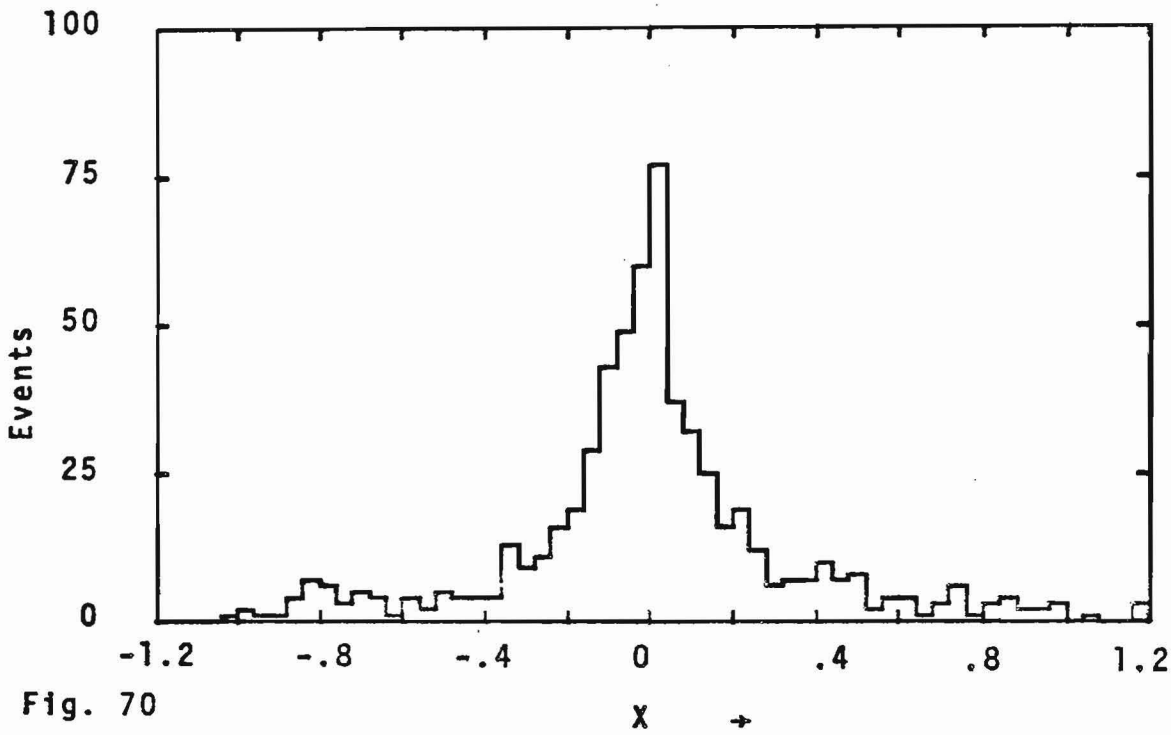

Fig. 70

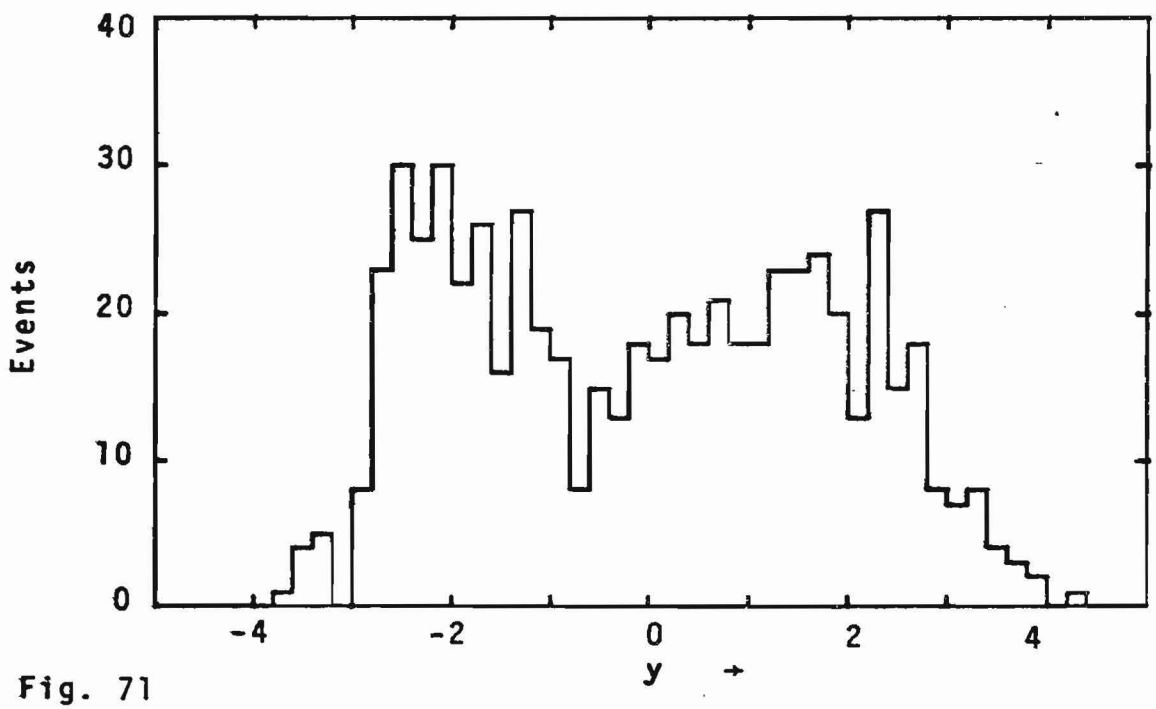

Fig. 71

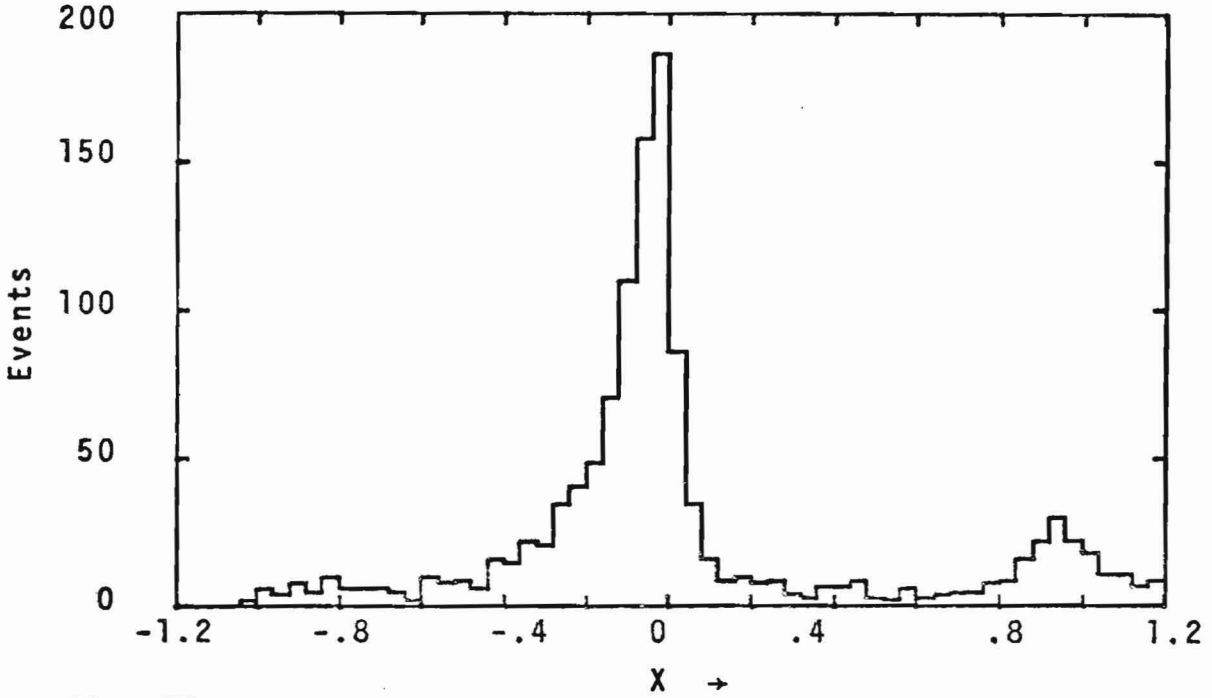
200
150
100
50
0
Events
-1.2
-.8
-.4
0
.4
.8
1.2
X →

Fig. 72

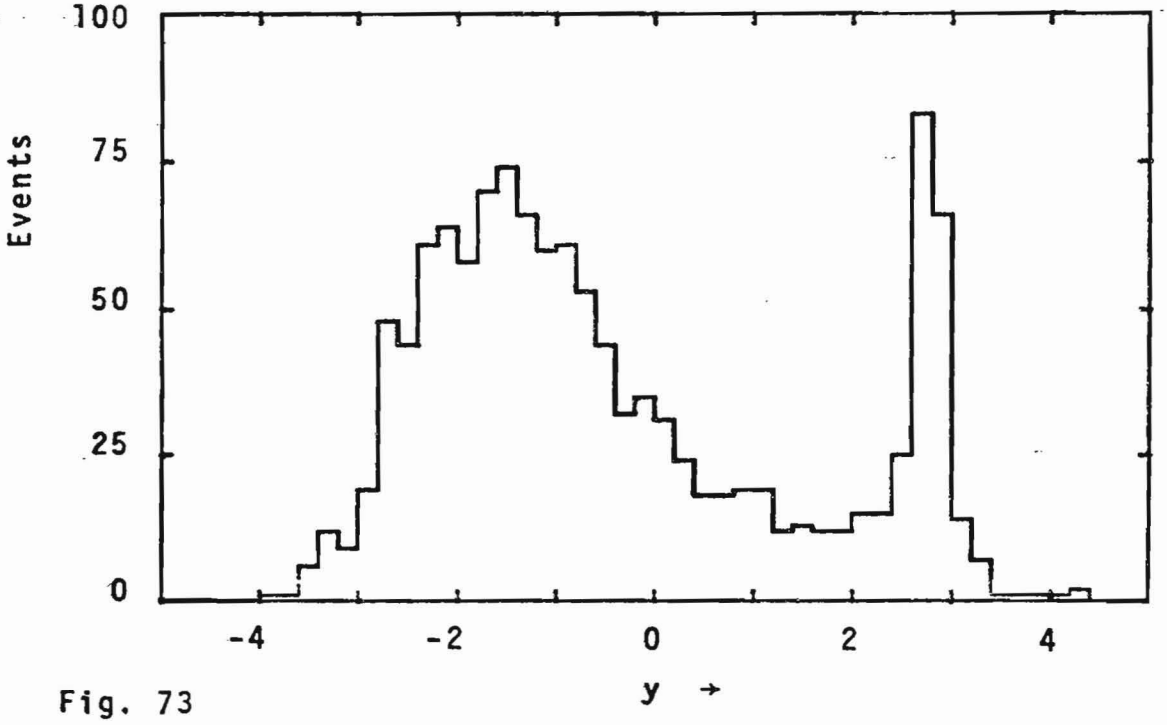
100
75
50
25
0
Events
-4
-2
0
2
4
y →

Fig. 73

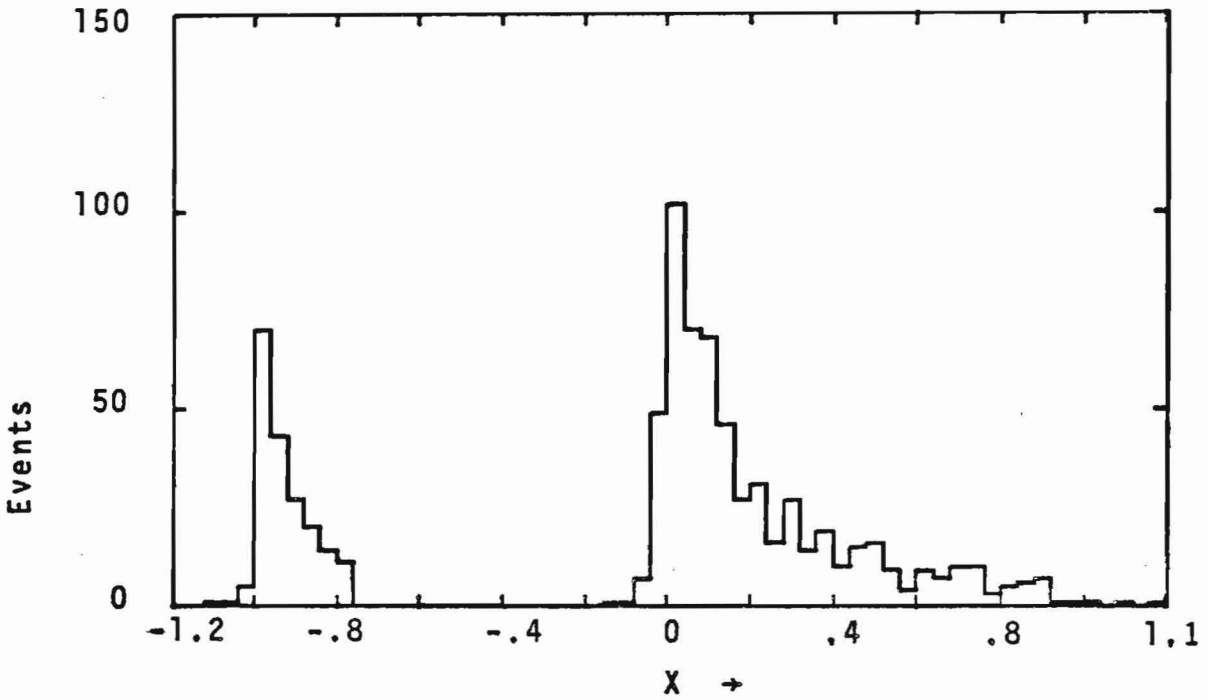

Fig. 74

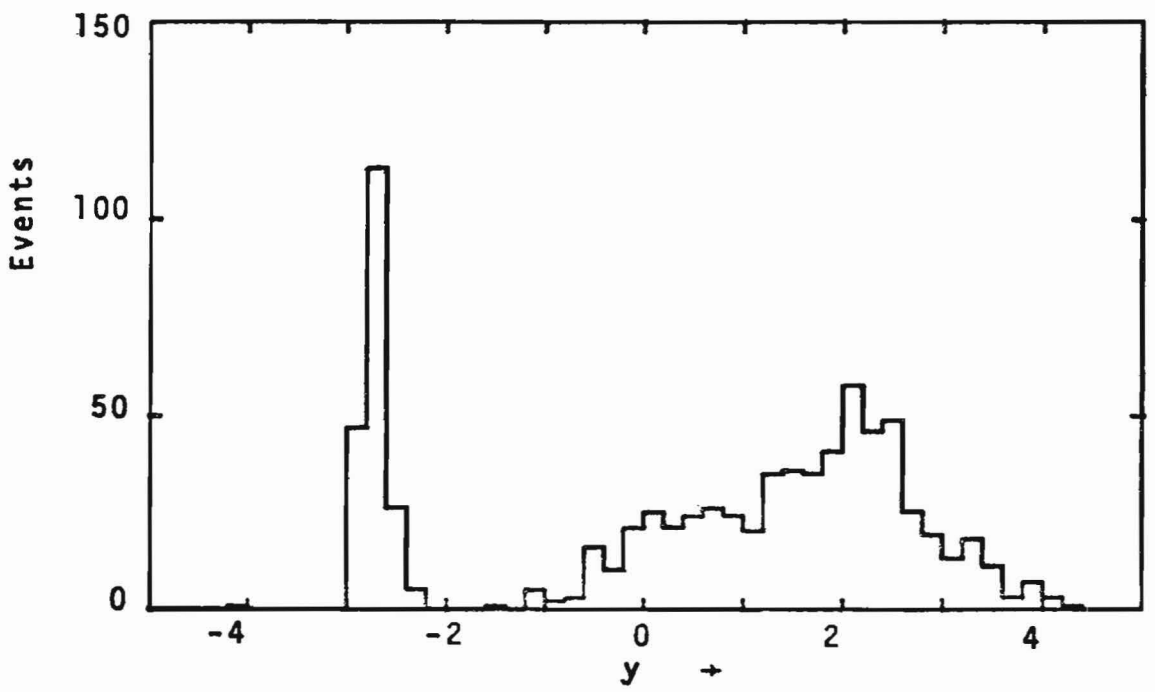

Fig. 75

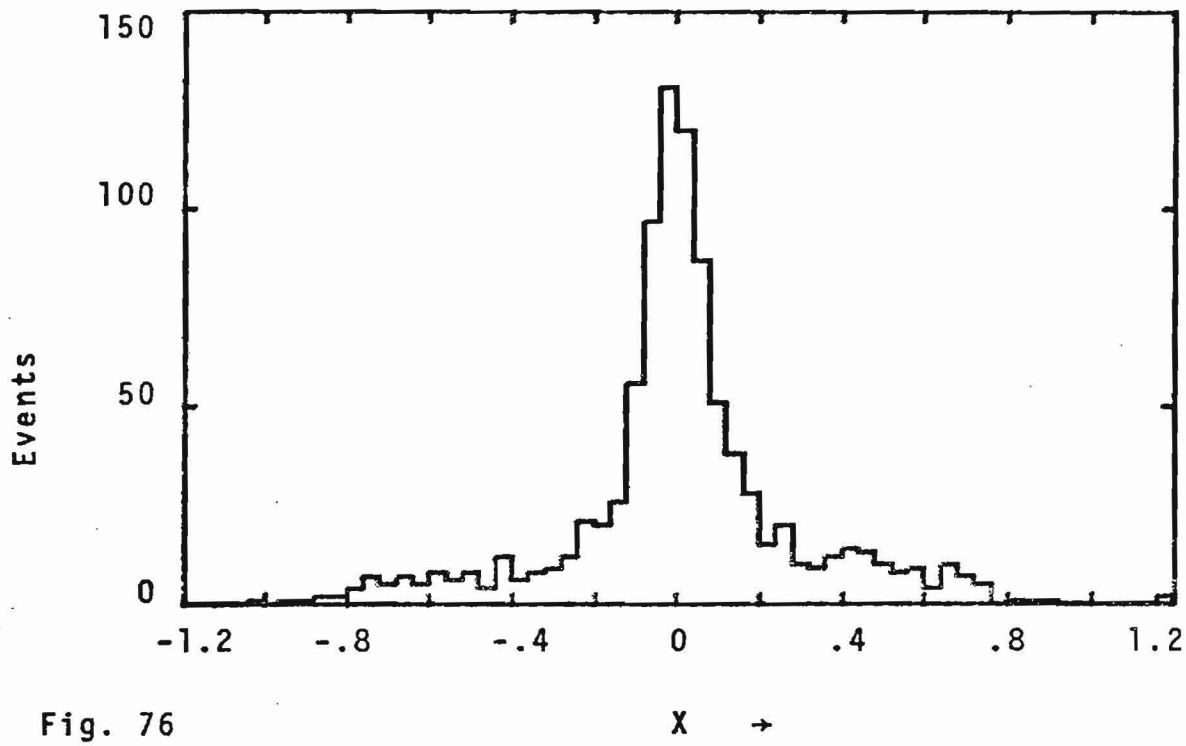

Fig. 76

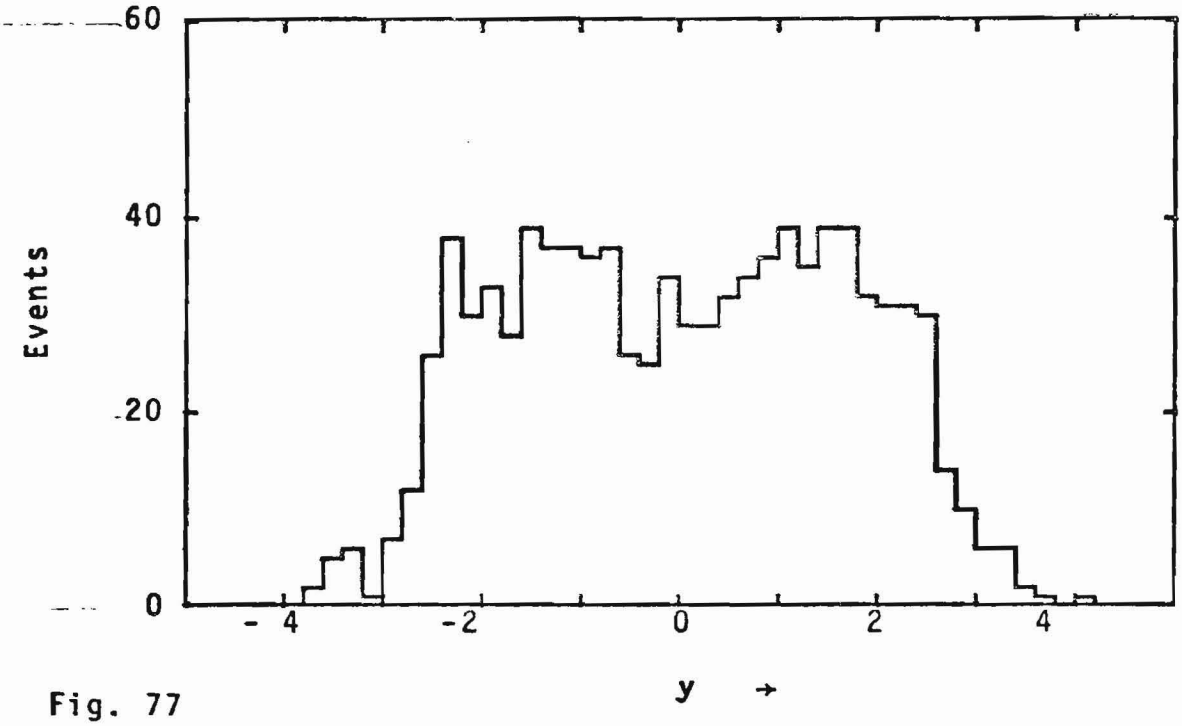

Fig. 77

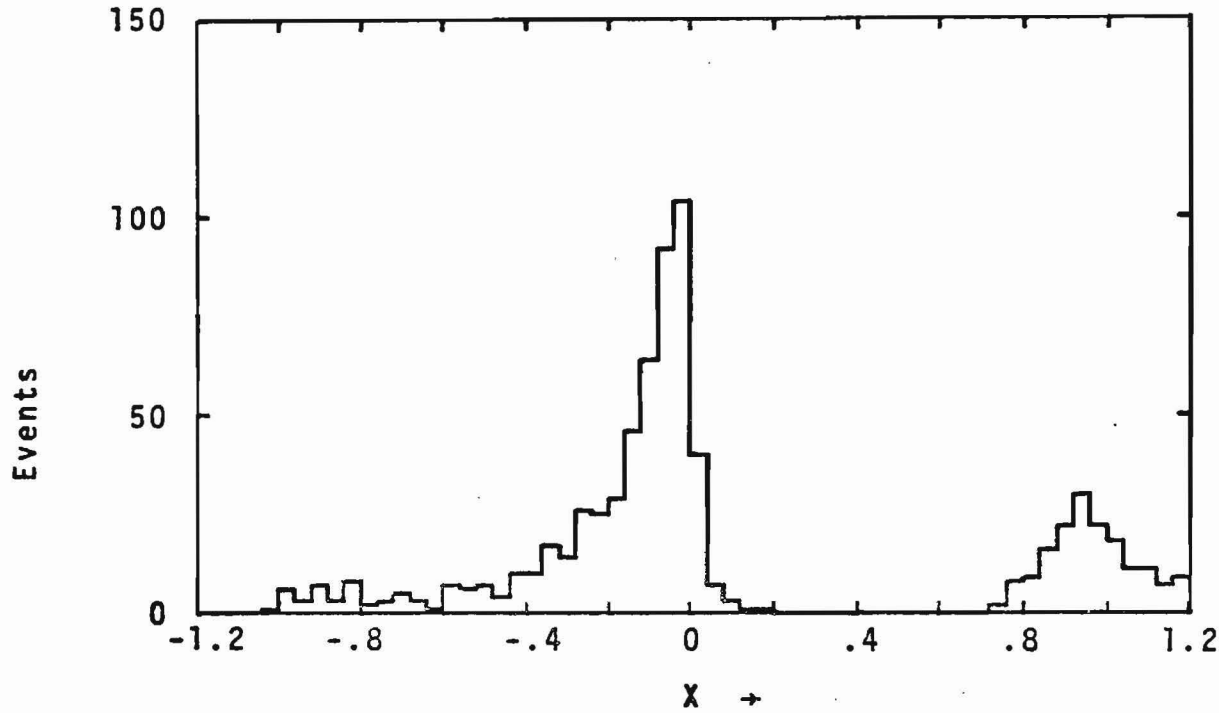

Fig. 78

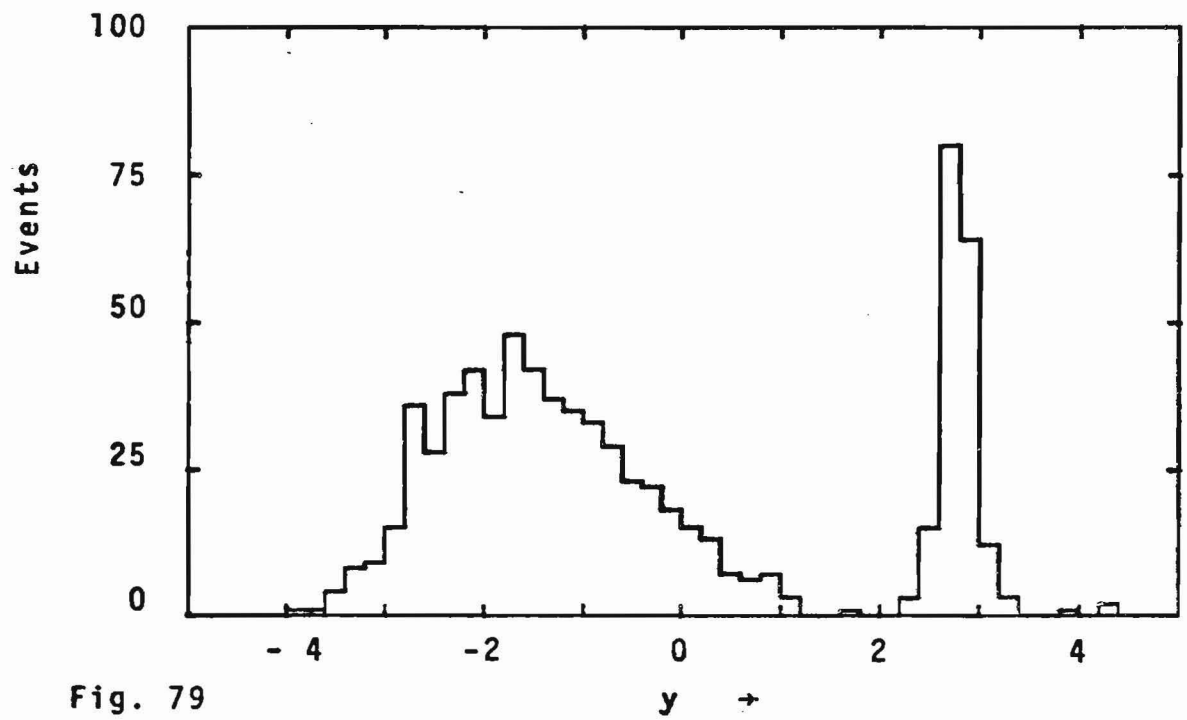

Fig. 79

$$g(x) = O(x)\ f(x) + \int_x^1 F(z)\ S(x,z)\ dz$$

where f(x) is the π^0 distribution, O(x) describes the fraction of π^0 decays resulting in two overlapping showers in the detector, and S(x,z) is the probability of a π^0 decay (at Feynman $x_{\pi^0} = z$) resulting in a gamma shower in the detector at $x_\gamma = x$. The functions O(x) and S(x,z) were determined using the Monte Carlo program for acceptance calculations. If all gammas were detected with no overlap, the above formula could be rewritten using the high energy approximation $S(x,z) \approx \frac{2}{z}$ as follows:

$$f(x) = -\left(\frac{x}{2}\right) \frac{dg}{dx}$$

This formula (Sternheimer, 1955; Kopylov, 1970) has been used to extract the π^0 x-distribution from bubble chamber measurements of the x-distribution of gammas.

For a discrete histogram, one can write:

$$\bar{g}i \sim \bar{O}_i\ \bar{f}_i + \left(\sum_{j=i}^{N} \bar{f}_j\ \bar{S}_{ij}\right) \Delta x$$

where average values are taken at the center of a bin. Inverting gives:

$$\bar{f}_i = \left[\bar{g}_i - \sum_{g=i+1}^{N} \bar{f}_j\ \bar{S}_{ij}\ \Delta x\right] \Big/ (\bar{O}_i + \bar{S}_{ii})$$

The gamma spectrum h(x), can be obtained from the $\bar{f}_i$:

$$\bar{h}_i = 2\,\Delta x \sum_{j=i}^{N} \bar{f}_j / x_j$$

Figures 80 and 81 show the weighted, inclusive π^0 x-distributions obtained by this procedure for π^+- proton and proton-proton events. Also shown are the corresponding π^+ and π^- distributions. The cross section for π^0 production is seen to be larger than the π^- cross section for both reactions, and there are considerably more π^0's at high x for π^+-proton events than for proton-proton events. In fact, a direct comparison of the distribution of total energy deposited in the lead glass from π^+-proton and proton-proton events (Figs. 82 and 83) indicates this. One can see considerably more events from π^+ beam with large energy deposition ($\gtrsim$ 60 GeV), indicating greater probability for energetic π^0's. These results are in agreement with naive expectations. The suppression of fast π^- is expected since production at $x \sim 1$ would require isospin 2 exchange for a π^+-proton interaction or baryon exchange for proton-proton. (see Barnes, et al., 1978a, 1978b)

Central production of π^+, π^0, and π^- might be expected to occur with equal frequency, independent of beam and target, for hadron-hadron reactions. The fragmentation of a proton or π^+ would be expected to produce more π^0's than π^-'s. For example, in the naive quark model, the proton contains two u-quarks and only one d-quark; the π^+ contains a u-quark and a $\bar{d}$ -quark,

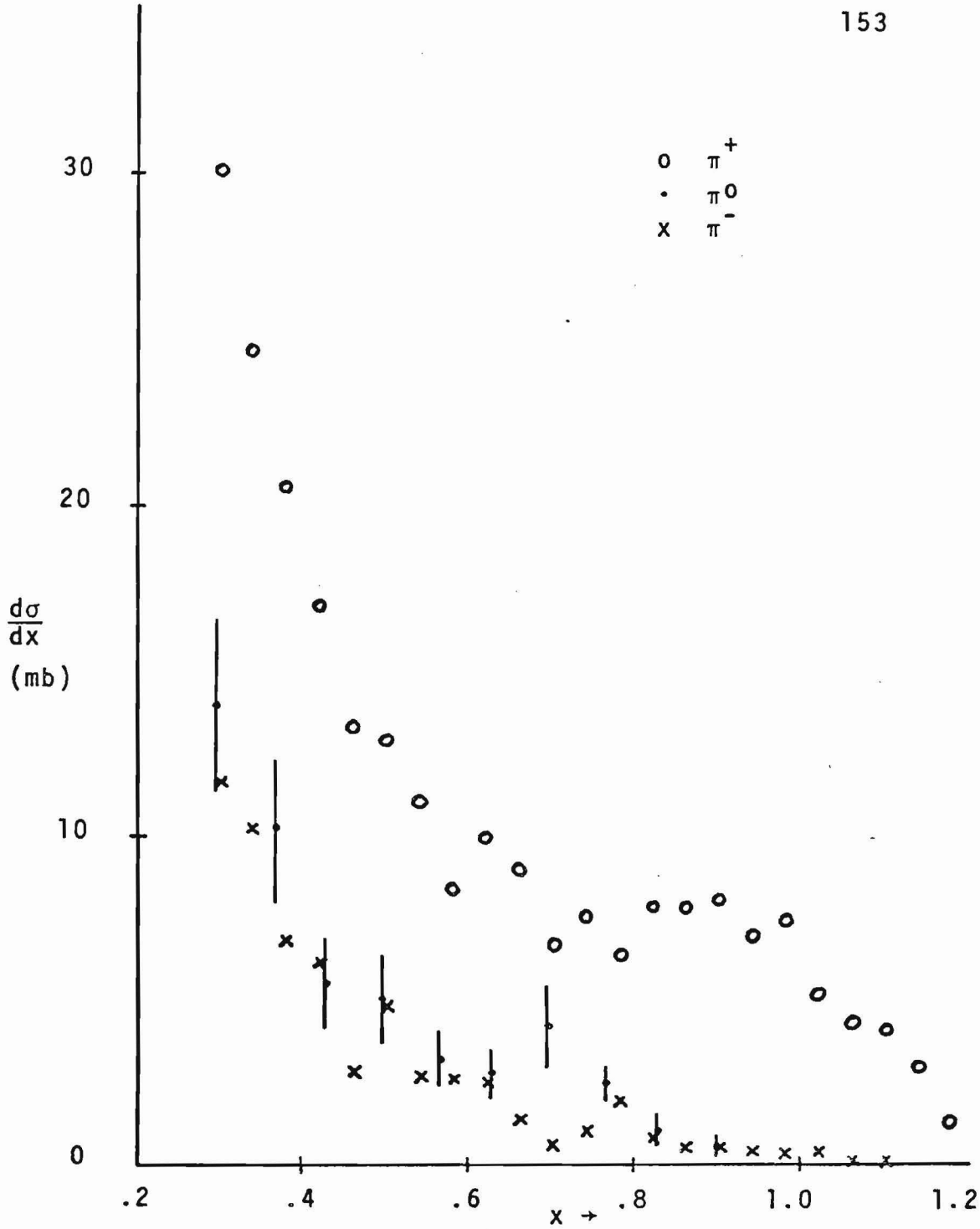

Fig. 80 - π^+ - Proton Events

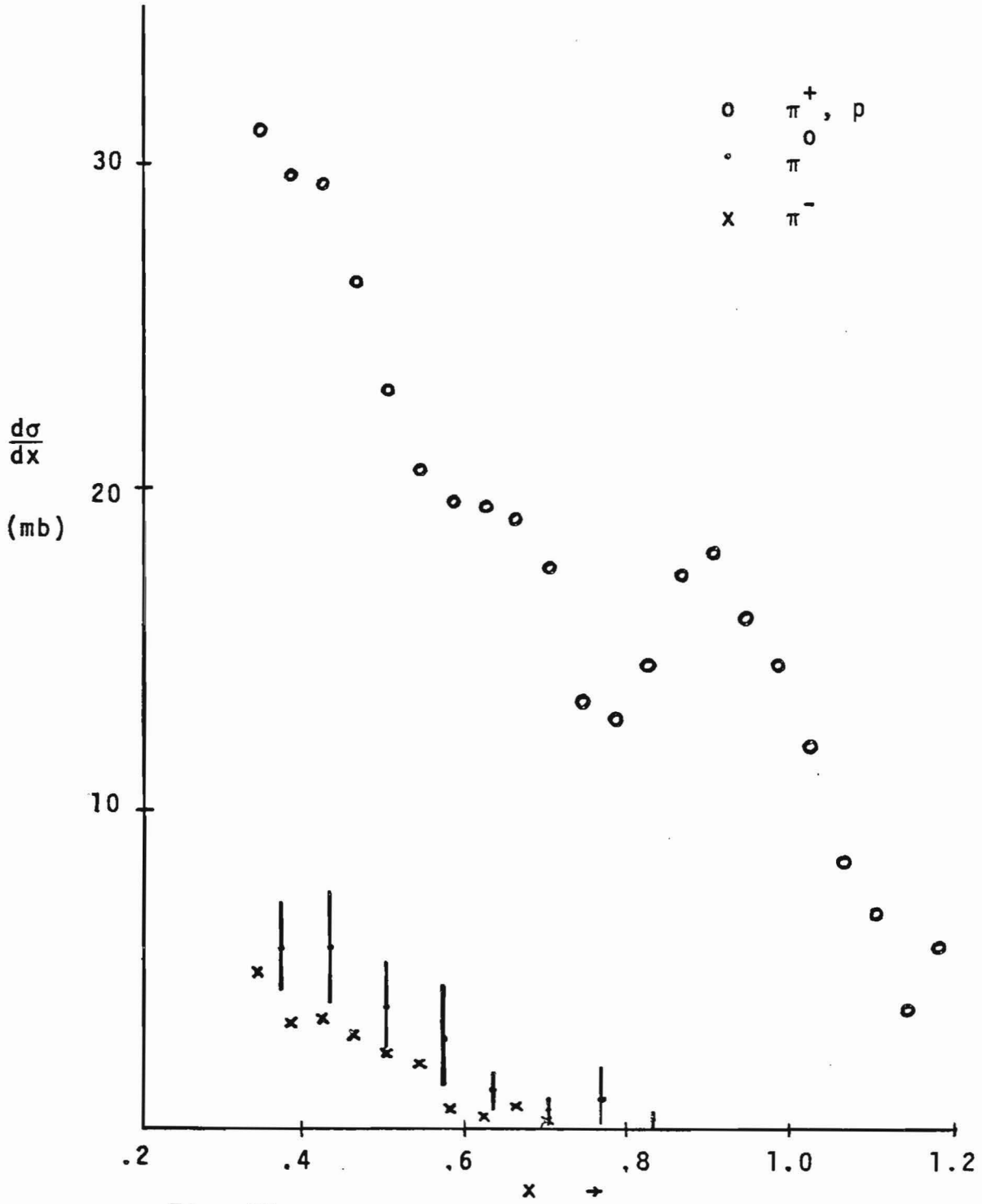

Fig. 81 Proton-Proton Events

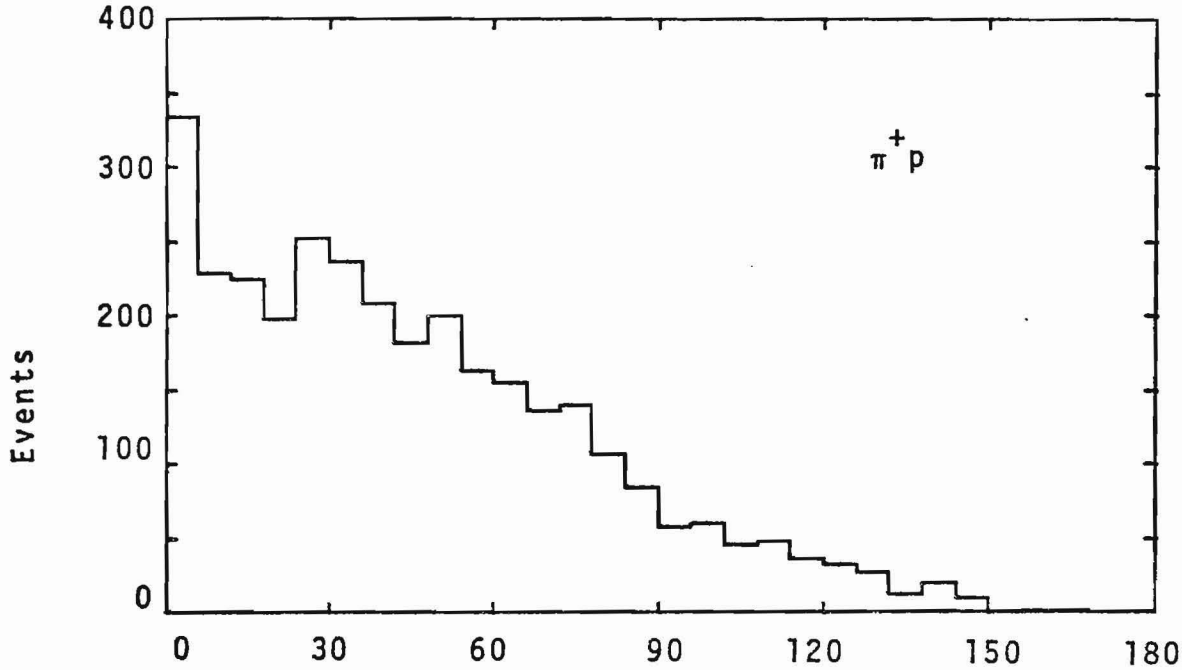

Fig. 82 Total Energy in Detector in GeV

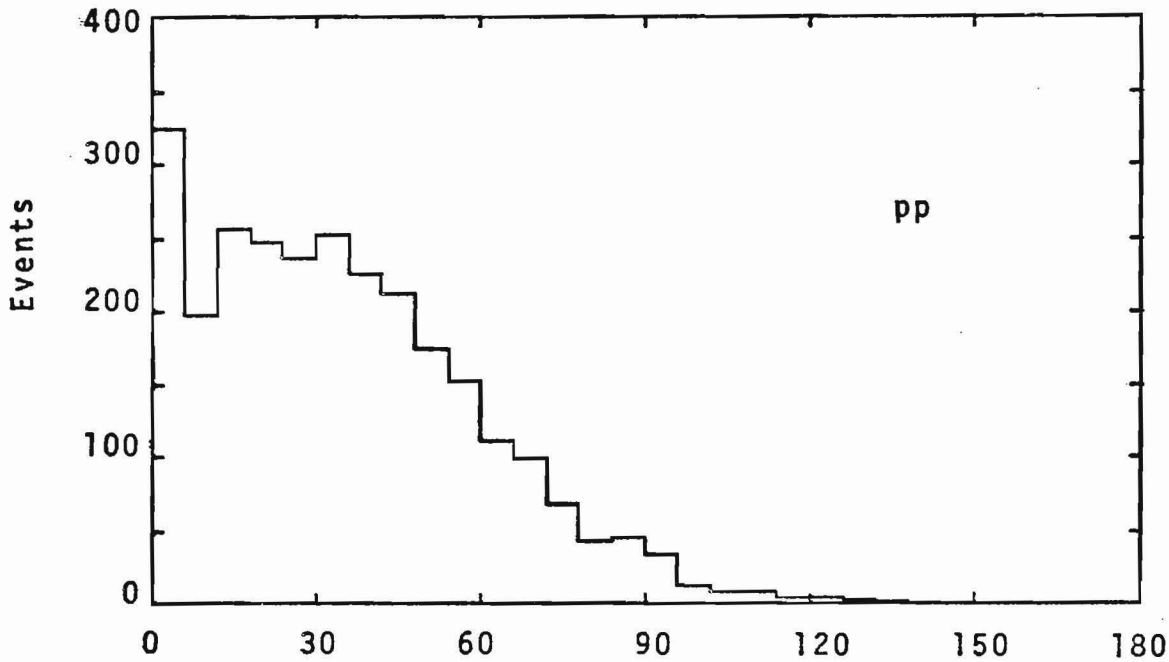

Fig. 83 Total Energy in Detector in GeV

neither of which is contained in the π^- (Ljung et al., 1977).

Figures 84 and 85 show the Feynman x-distributions of gammas measured in the bubble chamber together with the forward gamma spectra for proton-proton and π^+-proton events.

In principle, the gamma and π^0 distributions for diffractive events are obtained by the same "unfolding" procedure All events with associated gamma detector data were classified using the rapidity gaps between changed particles only, as previously done for the total data sample.

Forward gamma data for the leading beam events is useful primarily as a check on the separation technique. The requirement of $x > .75$ for a leading beam particle ensures that the x value of any associated fragment is less than $x = .25$. Any gammas reaching the detector must come either from misidentified events, i.e. non-leading beam, or from the small forward part of the target fragmentation. The results are given in Tables XIV and XV. Of the detected π^0's, four had $x > .25$ in the π^+-proton events, and four also had $x > .25$ in the proton-proton events. If all events with detected gammas are assumed to be non-diffractive, then the leading-beam sample is reduced by 12% for π^+-proton events and by 11% for proton-proton events.

Leading proton events were examined to determine the number of showers produced in beam fragmentation and the distribution according to event prong count. After hadron shower rejects were removed a sample of 157 π^+-proton and 152 proton-

Fig. 84

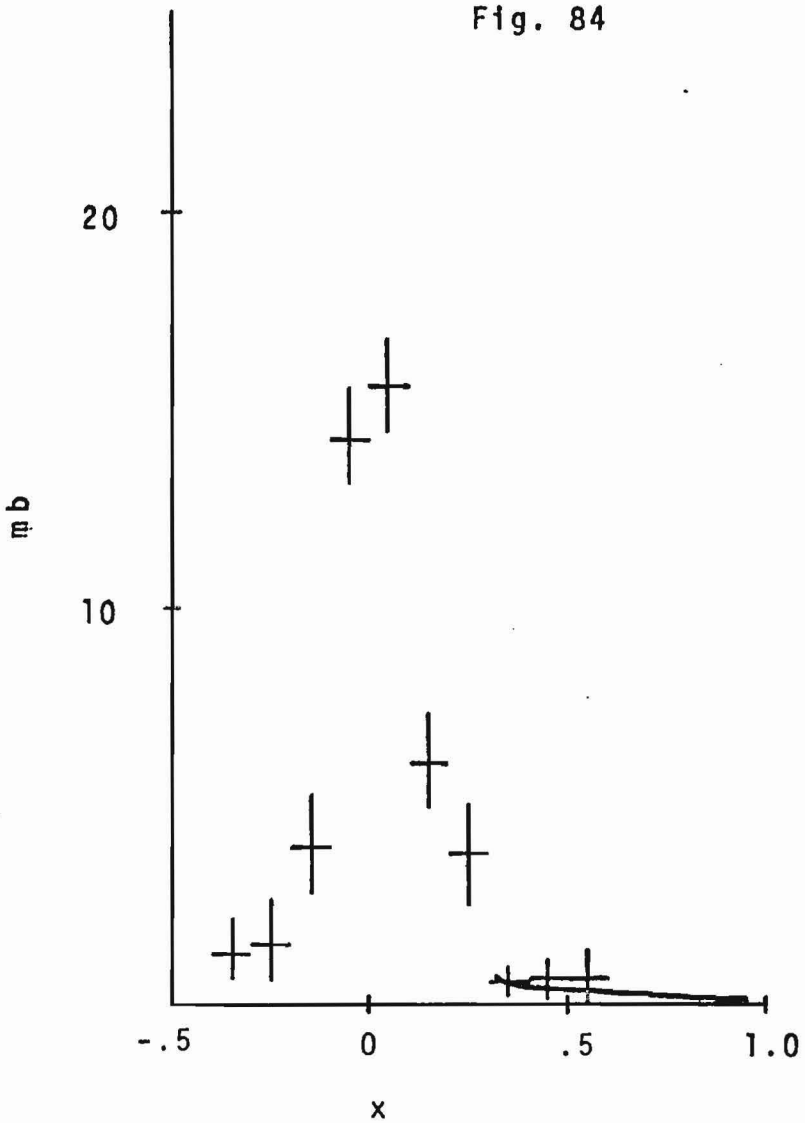

Fig. 85

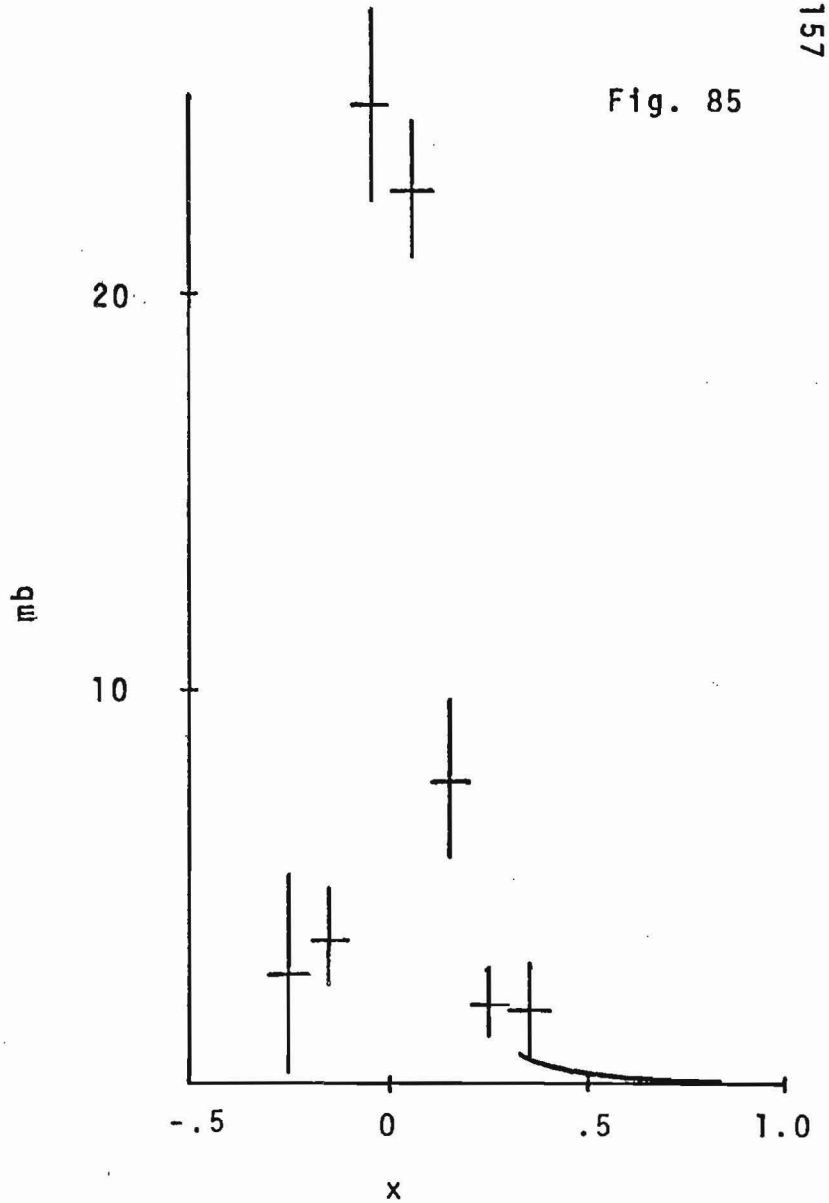

TABLE XIV

Distribution of Showers in Leading Beam Events

Number of Events	Proton-proton Events	π^+-proton Events
0	213	258
1	10	15
2	8	8
3	5	11
4	3	0
	239	292

TABLE XV

Multiplicity Distribution of Leading Beam Events

Prong Count	proton-proton Events	Number of Detected π^0's	π^+-proton Events	Number of Detected π^0's
2	97	2	108	4
4	74	4	106	4
6	42	2	42	1
8	20	1	25	1
10	5	0	8	1
12	1	0	2	0
14	0	0	1	0
	239	9	292	11

proton events remained. Results are summarized in Tables XVI and XVII. Of the detected 39 π^0's, 24 events had $x > .25$. The energy distribution of detected showers is shown in Figures 86 and 87 for $\pi^+ p$ and proton-proton events respectively. An interesting result is that a large fraction, 62% of the π^+-proton events and ~52% of the proton-proton events have associated showers in the gamma detector. This agrees with the observations made in Section II. Based on the number of 4-constraint fits in previous measurements, more than half of the diffractive events contain one or more neutral particles.

D. Resonance Production

Production of $\rho^0(770) \rightarrow \pi^+ \pi^-$ and $\Delta^{++}(1232) \rightarrow p \pi^+$ resonances has been studied at several Fermilab energies using pion and proton beams (Whitmore 1976; Higgins et al. 1979; Brick et al. 1978). The inclusive cross section for production of these resonances does not decrease as a power of s, as do exclusive processes, such as charge exchange ($\pi^- p \rightarrow \pi^0 n$). A substantial part of the produced ρ^0's from a pion beam are associated with the beam fragmentation region. Virtually all of the detected Δ^{++} are associated with proton fragmentation. The forward gamma detector data was used to search for production of resonances involving a single π^0, in particular, $\rho^{\pm} \rightarrow \pi^{\pm} \pi^0$ and $\omega^0(783) \rightarrow \pi^+ \pi^- \pi^0$.

TABLE XVI

Distribution of Showers in Leading Target Events

Number of Showers	proton-proton Events	π^+-proton Events
0	73	60
1	22	26
2	22	28
3	21	29
4	13	12
5	1	2
	152	157

TABLE XVII

Multiplicity Distribution of Leading Target Events

Prong Count	proton-proton Events	Number of Detected π^0's	π^+-proton Events	Number of Detected π^0's
2	78	9	70	6
4	47	9	52	17
6	21	7	23	10
8	6	3	12	6
	152	28	157	39

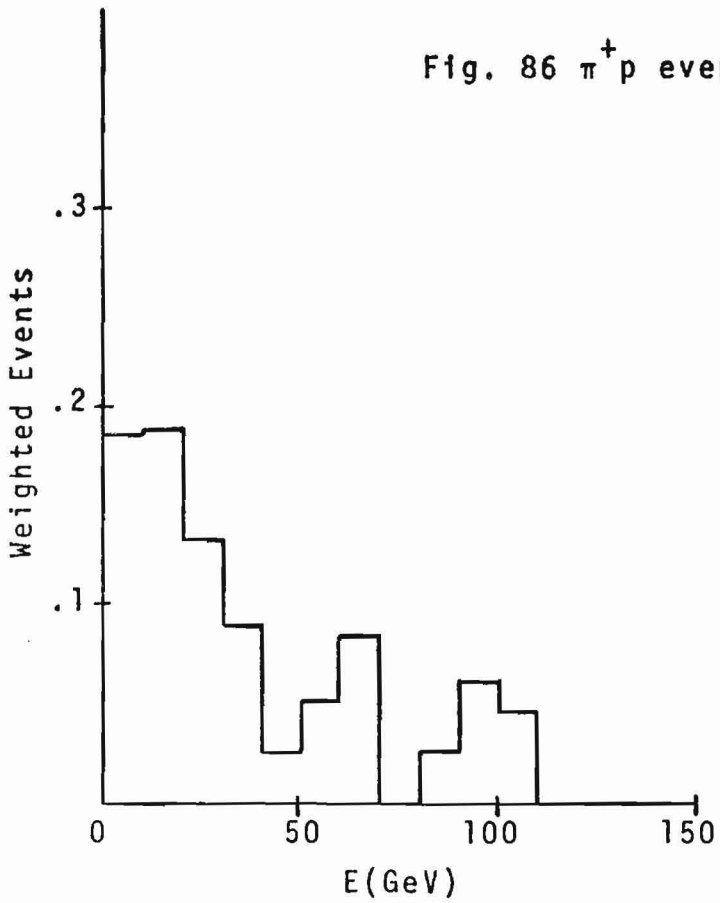

Fig. 86 π^+p events

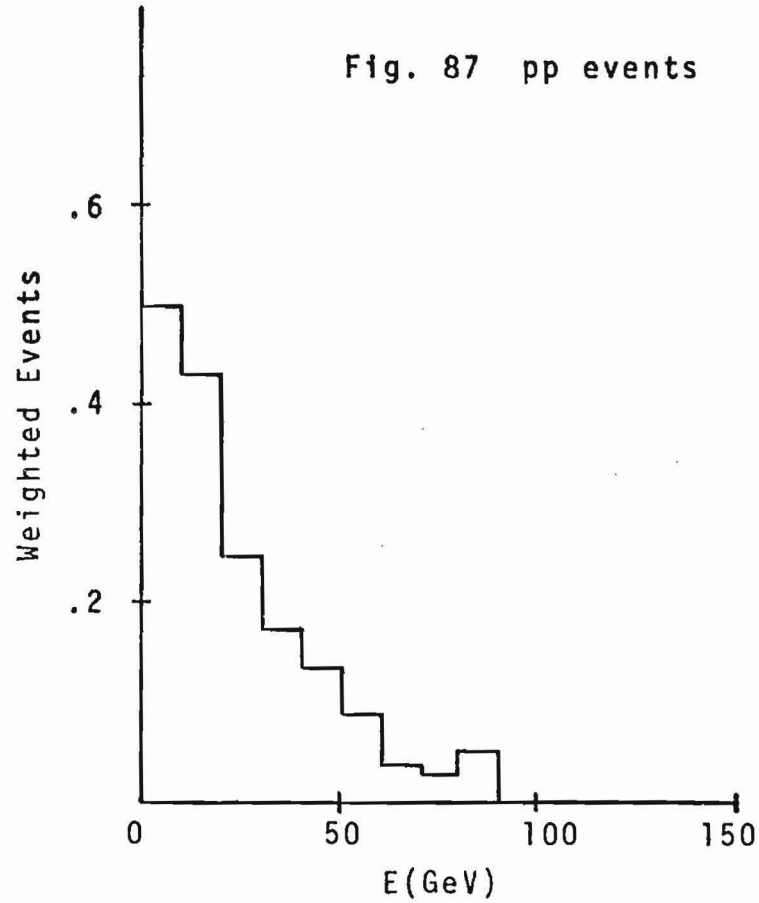

Fig. 87 pp events

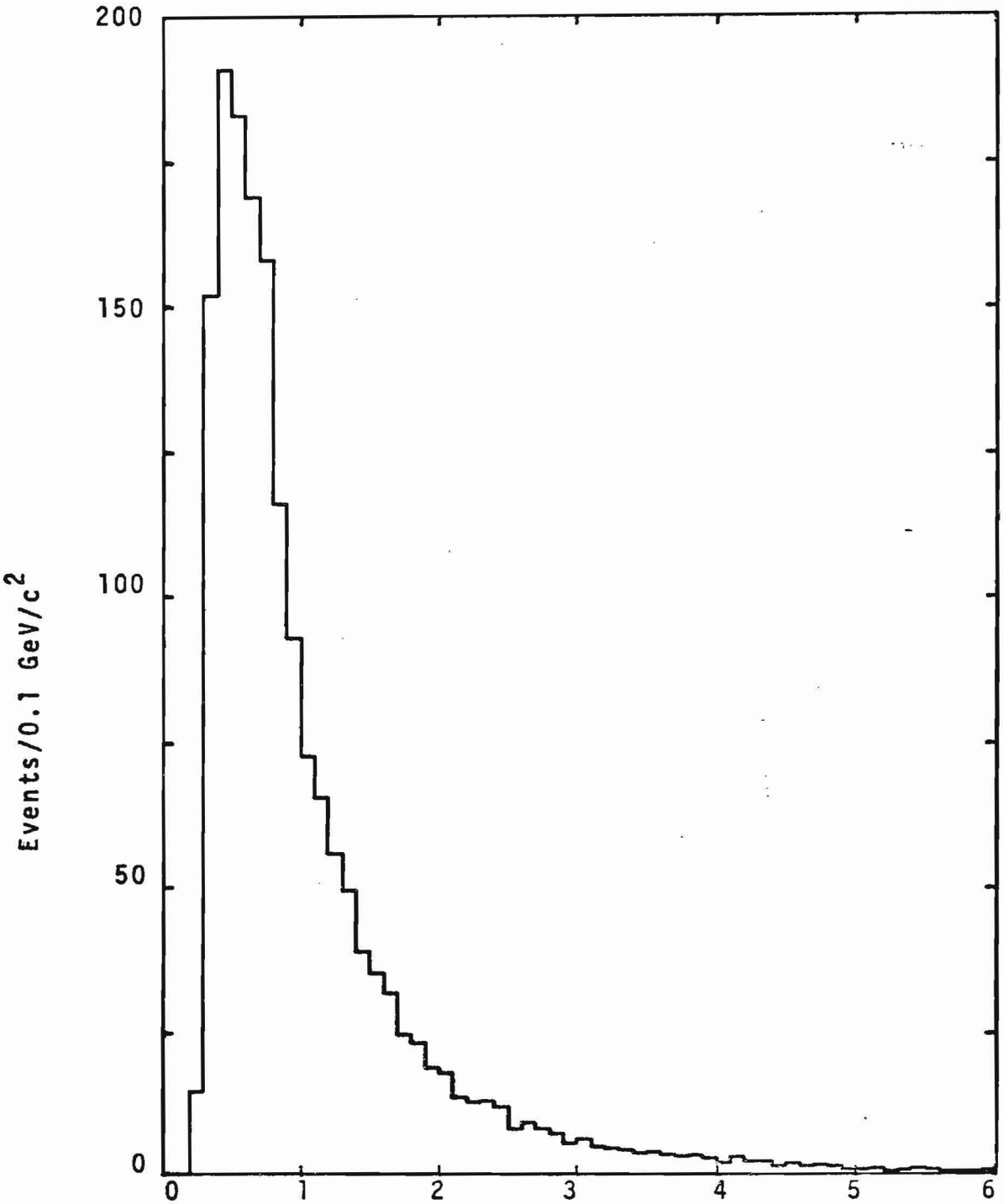

Fig.88 - $M(\pi^+\pi^-)$ GeV/c^2

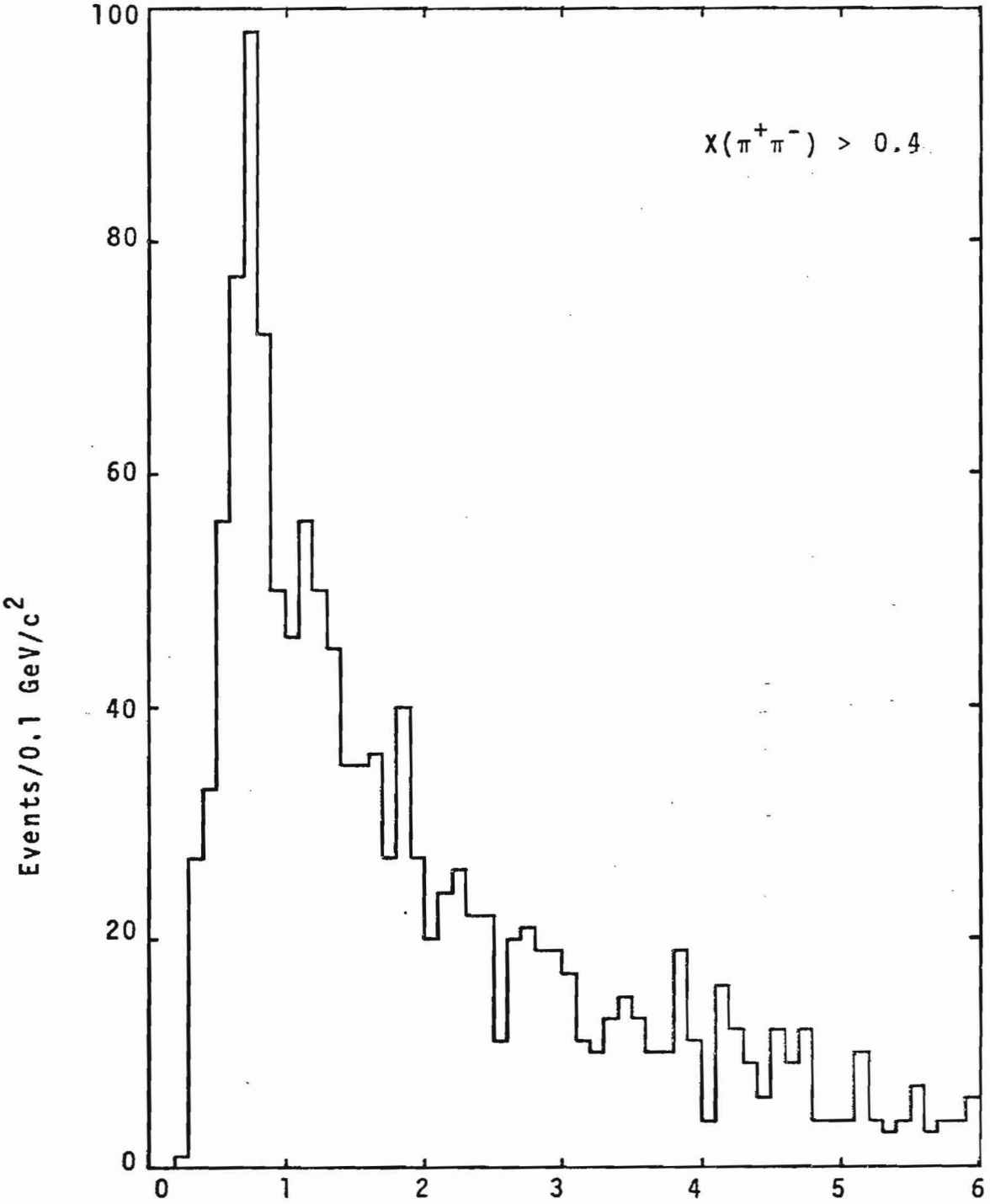

Fig. 89 -

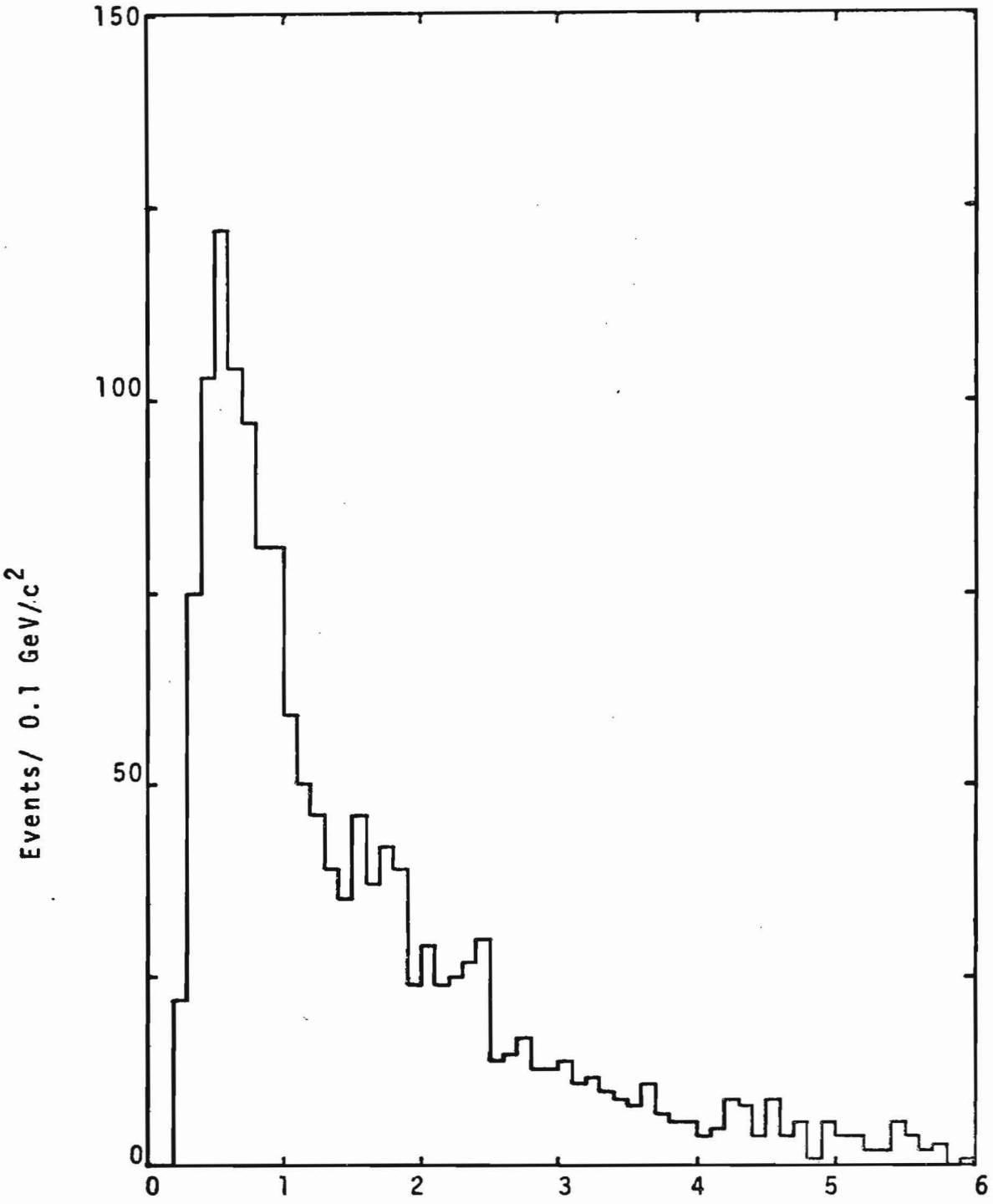

Fig. 90 -

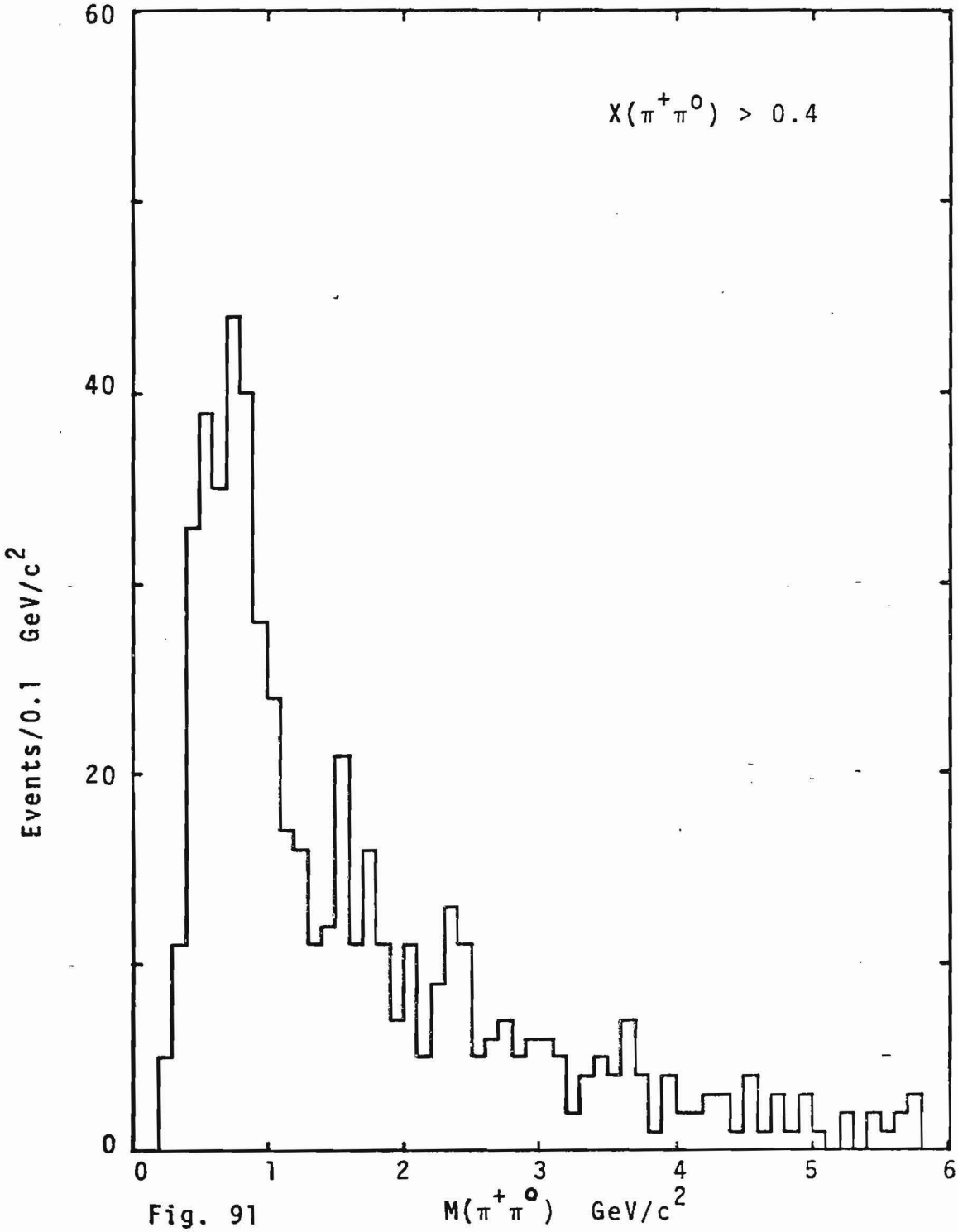

Fig. 91

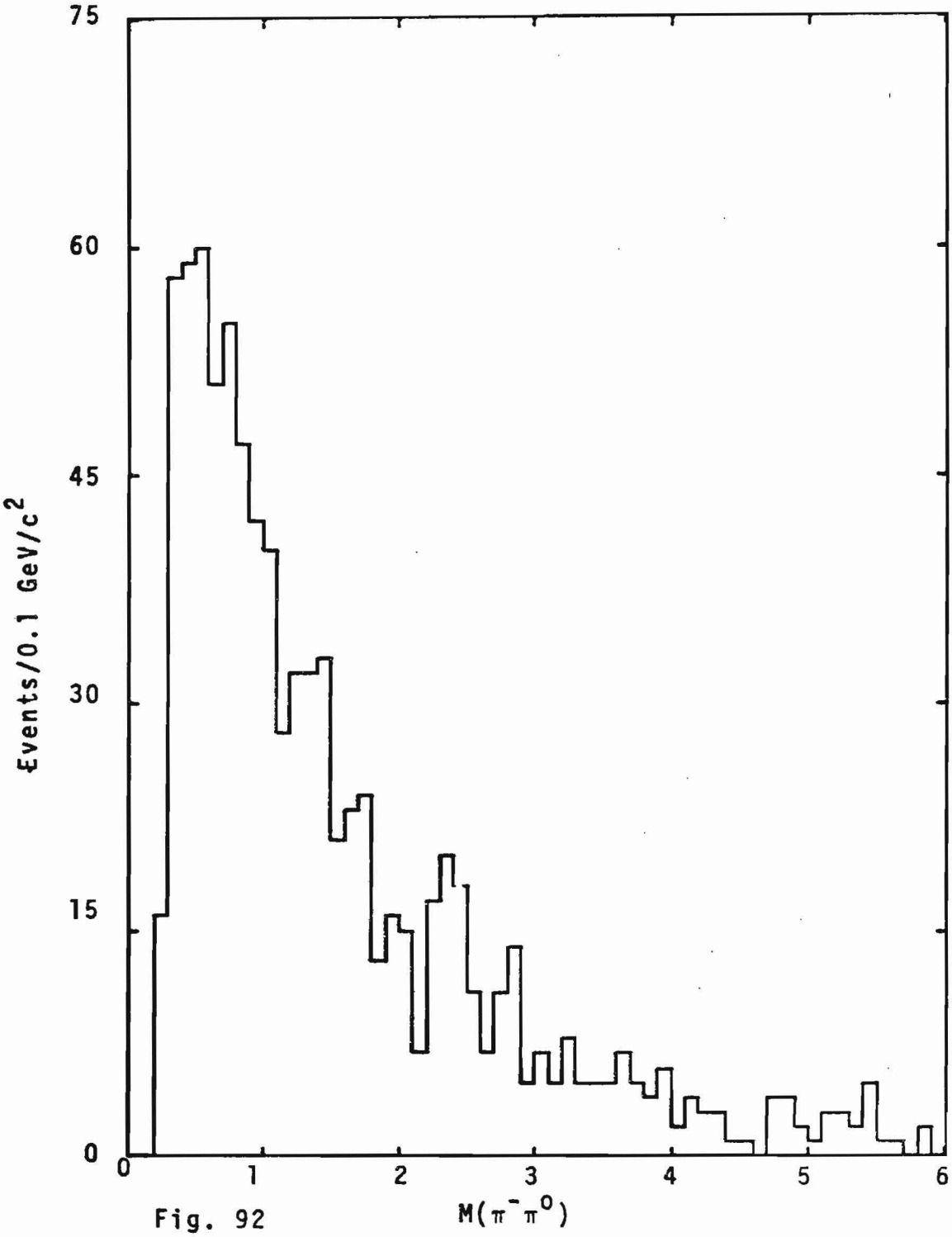

Fig. 92

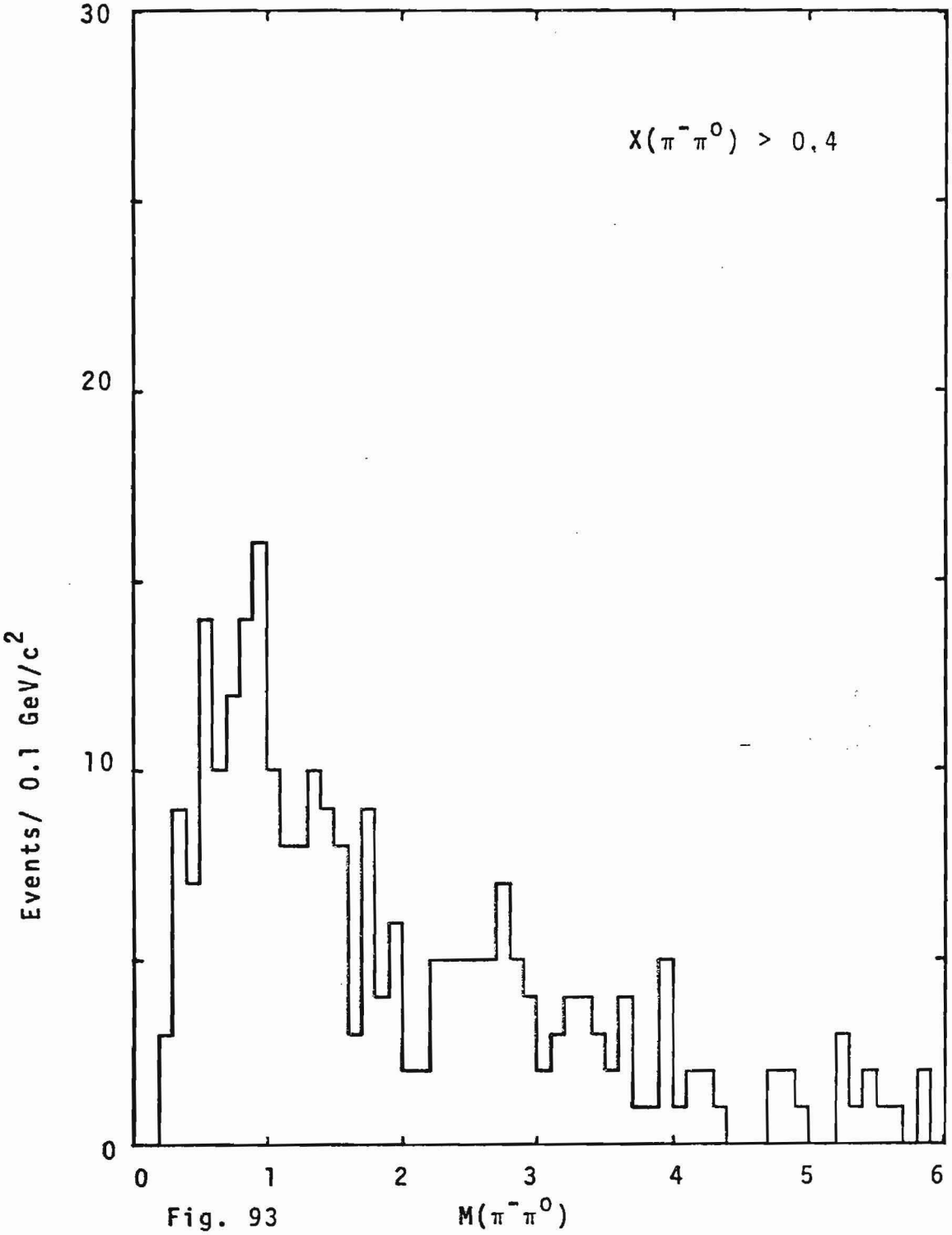

Fig. 93

Figure 88 is the $\pi^+\pi^-$ invariant mass distribution; only a slight shoulder is seen at the location of the $\rho^0(770)$. This ρ^0 signal was enhanced by restricting the plots to $\pi^+\pi^-$ combinations with the Feynman x of the dipion system greater than 0.4 (Fig. 89). The corresponding distributions for the $\pi^+\pi^-$ combinations are shown in Figure 90 and 91, and the $\pi^-\pi^0$ combinations are shown in Figures 92 and 93. Both the $\pi^+\pi^-$ and $\pi^+\pi^0$ combinations are compatible with substantial ρ^0 and ρ^+ production (respectively). The background shape makes estimation of cross sections difficult, however, a sensible background curve may be estimated using the higher statistics available by including $\pi^+\pi^-$ combinations from events with no associated gamma data.

When this background curve is normalized to the data of Figures 76 and 77, an excess of ~50 combinations is found near the ρ^0 mass and ~60 combinations near the ρ^+ mass. The acceptance of the gamma detector for a fast shower from ρ^+ decay varies from 83 - 93% as x_ρ increases from .4 to 1.0. Conversion losses of fast gammas from π^0 decay result in an altered background distribution, however, with fewer dipion combinations at larger mass values. Neglecting this effect, the number of fast ρ^+'s is estimated to be equal, $\pm 30\%$, to the number of fast ρ^0's from π^+-proton interactions.

Resonance decay of $\omega^0(783) \rightarrow \pi^+\pi^-\pi^0$ was not observed; the $(3\pi)^0$ invariant mass distribution displayed a smooth rise in this region.

VII. Discussion and Conclusions

Data from a prototype forward gamma detector have been used to extract information regarding gamma, and hence π^0, production associated with π^+-proton and proton-proton interactions in the Fermilab 30-inch hybrid bubble chamber spectrometer. Inclusive single-particle π^0 distributions in the kinematic variables of Feynman x, rapidity, and transverse momentum (x,y, p_T) have been examined and compared with corresponding $\pi^{\pm}$ distributions. The π^+ -proton events exhibit higher probability for fast π^0 and π^- production than do the proton-proton events. Production of ρ^0 and ρ^+ in the π^+-proton events can account for most of the difference.

Good momentum resolution for fast tracks in the downstream spectrometer system allows a clean separation of leading particle events. Such events were required to 1) have the largest rapidity gap (between adjacent charged particles as ordered in rapidity) next to the first or last particle in the ordered rapidity chain, and 2) have a Feynman x for the leading particle such that $|x| \geq .75$. This sample should predominantly isolate events containing diffractive excitation of either the beam or the target particle and events in the triple-Regge region due to PPP, PPR, and RRR terms which contain leading particle peaks. The multiplicity distributions and kinematic properties of this sample were examined. Contributions from PPR and RRR terms are expected to cause shrinkage of the

leading particle peak at higher energy. Approximately 62% of the leading-target π^+-proton events were found to have detected gammas (52% for the corresponding proton-proton events). Production of ρ^+ might account for fast π^0's in the leading-target π^+-proton events -- the data sample is too small to allow a stronger conclusion. Most of the fast π^0's result from events in the non-diffractive sample.

In conclusion, useful physics data have been obtained utilizing a prototype forward gamma detector. The most significant contribution of the present experiment may, however, be an understanding of the problems of hadron shower background and multishower resolution, allowing most efficient use of the full-scale detector for future high statistics studies of π^0 production.

APPENDIX

Proton Assignment without Ionization Information

A portion of the data was measured without ionization information. An attempt was made to identify slow protons using the following methods. Using events identified as elastics, by program PWGEL, a scatterplot of $\cos\theta$ versus momentum was made for the slow positive tracks, where θ is the angle between the track and the beam direction in the scattering plane. This yields a distinctive functional dependence, which can be explicitly calculated. Energy and momentum conservation leaveonly two free parameters, which may be chosen as angle and momentum of the recoil proton. A two-dimensional cut identifies almost all quasi-elastic protons, with a minimal background of misidentified pions. As a quality check, events with measured ionization were processed in the same manner as the Rutgers data, ignoring the ionization information. More than 90% of the tracks selected as protons were in the sample identified as protons. The elastic 2-prong events indicate that, even with complete ionization information, approximately 10% of the protons can not be identifed. This may be compared with an estimate of 3-9%, for $\pi^- p$ at 147 GeV/c, using a linear extrapolation above 1.5 GeV/c of the momentum spectrum of ionization-identified protons (Brick et al., 1978). The Feynman-x distribution of these protons (which were assigned a pion mass) was found to be contained in the range $-.56 < x < -.12$. This

allows a search for unidentified protons in events having a specific kinematical configuration (quasi-elastic) and prong count >2.

Tracks faster than 1.5 GeV/c can not be identified by ionization. Only the comparatively rare decays of a track inside the bubble chamber allow some mass determinations, for example, $\pi^{\pm} \rightarrow \mu^{\pm}\nu \rightarrow e^{\pm}\bar{\nu}\nu$. However, the events with ionization data allow relatively accurate determination of the π^{+} and π^{-} x-distributions in the backward hemisphere in the center of mass (CM) frame. Only 1% of the proton-proton events have a π^{+} of $x < -.5$, while 97% of the identified protons lie in this range. Accordingly, all positive particles with $x > +.5$ are assigned a proton mass in proton-proton events. In addition, if an event had the largest rapidity gap at the target end of the ordered rapidity chain, and $x < -.12$ for the end particle, the end particle was assigned a proton mass. The combined effect of all these cuts gives an asymmetry in the proton-proton events: an excess of slow protons. This was taken into account in the cross section computations. Rutgers is presently measuring ionization, and a comparison can soon be made.

R E F E R E N C E S

Abarbanel, H.D.I., 1976, Rev. Mod. Phys. 48, No. 3, 435.

Amaldi, U., M. Jacob and G. Matthiae, 1976, Ann. Rev. Nucl. Sci. 26, 385.

Andersson, A.A. and I.A. Pless, 1976, Proceedings of the Conference on Computer Assisted Scanning, Padova, 512.

Ayres, D.S. et al., 1977, Phys. Rev. D15, 3105.

Bachman, L., 1978, Program Hopion, private communication.

Baksay, L. et al., 1976, Phys. Lett. 61B, 89.

Barash-Schmidt, N. et al., 1978, Particle Properties Data Booklet, printed at Lawrence Berkeley Laboratory, Berkeley, California.

Barish, S. et al., 1974, Phys. Rev. D9, 1171.

Barnes, A.V. et al., 1978a, Inclusive π^0 and η Production From 100 GeV/c π^+p Collisions in the Triple Regge Region, preprint CALT-68-664.

——————— 1978b, Inclusive π^0 and η Production in the All Neutral Mode from 100 GeV/c π^-p Collisions, preprint CALT 68-667.

Bettini, A. et al., 1975, An External Gamma Ray Detector to be used with BEBC with the TST for Experiments at the SPS, CERN/SPSC/75-24/p.45. Addendum: CERN/SPSC/75-60/p.45/Add. 1.

Biel, J. et al., 1976, Phys. Rev. Lett. 36, No. 10, 504.

Bingham, H.H. et al., 1974, Phys. Lett. 51B, 397.

Bober, J.T. and T.A. Frank, 1976, A 5x5 Lead Glass Block Hodoscope, APC Engineering Note 76-5.

Brau, J., 1977, TRACK ORGANIZER Documentation, APC Programming Note DAS 77-8.

Brick, D. et al., 1978, Phys. Rev. D18, 3099.

Brucker, E.B., 1978, private communication.

Bugg, W.M., 1974a, PHS Consortium Newsnote No. 28.

_____ 1974b, PHS Consortium Newsnote No. 30.

Bushnin, Yu. et al., 1973, N.I.M. 106, 493.

_____ 1974, N.I.M. 120, 391.

Day, T.B. et al., 1974, Univ. of Maryland AEC-ORO-2504-100 Supplements.

De Kerret, H. et al., 1976, Phys. Lett. 63B, 477.

Derrick, M. et al., 1974a, Phys. Rev. D9, 1215.

_____ 1974b, Phys. Rev. D9, 1853.

_____ 1975, in "Particles and Fields", p.33, Seattle.

DeTar, C.E., 1971, Phys. Rev. D3, 128.

d'Innocenzo, A., G. Ingrosso, and P. Rotelli, 1978, Nuovo Cimento 44A, No. 3.

Erwin, J. et al., 1974, Phys. Rev. Lett. 32, 254.

Feinberg, E.L. and I.Ia. Pomeranchuk, 1956, Suppl. Nuovo Cimento III, 652.

Fiałkowski, K. and H.S. Miettinen, 1973, Phys. Lett. 43B, 61.

Fong, D. et al., 1976a, Nucl. Phys. B102, 386.

_____1976b, Nuovo Cimento 34A, 659.

_____1975, Phys. Lett. 60B, 124.

_____1974, Phys. Lett., 53B, 290.

Frazer, W.R. and D.R. Snider, 1973, Phys. Lett. 45b, No.2,136.

Froissart, M., 1961, Phys. Rev. 123, 1053.

Glauber, R.J., 1955, Phys. Rev. 99, 1515.

Goggi, G. et al., 1977, Phys. Lett. 72B, 261.

Good, M.L. and W.D. Walker, 1960, Phys. Rev. 120, 1857.

Hafen, E.S., 1975, GEOMAT - Part I, APC Programming Note DAS 75-1.

Hafen, E.S. and R.I. Hulsizer, 1977, IHS Consortium Newsnote No. 43.

Harari, H. and Rabinovici, E., 1973, Phys. Lett. 43B, 49.

Heller, M. et al., 1978, N.I.M. 152, 379.

Higgins, P.D. et al., 1979, Phys. Rev. D19, 65.

Kafka, T. et al., 1979, Phys. Rev. D19, 76.

Kerns, C., 1975, Fermilab, private communication.

Kopylov, G.I., 1970, The Basis of Resonance Kinematics, Nauka, Moscow.

Lach, J. and E. Malamud, 1973, Phys. Lett., 44B, 474.

Leith, D.W.G.S., 1974, in "Proceedings of Summer Institute on Particle Physics," SLAC 179, Vol. I, p. 1.

Ljung, D., 1974, Selection of .2 GeV/c to 1.4 GeV/c Protons Using PEPR Ionization Measurements.

Ljung, D. et al., 1977, Phys. Rev. D15, 3163.

Low, F.E., 1975, Phys. Rev. D12, 163.

Ludlam, T., 1977, PROGRAM PWGEL, private communication.

Messiah, A.H., 1966, Quantum Mechanics, Chapter 10, John Wiley and Sons, New York.

Miettinen, H.I. and J. Pumplin, 1978, Phys. Rev. D18, 1696.

Morecroft, L., 1978, Updated GEOMAT and GEOMAT Tape Format for Use with GEOMAT Version 3.22, APC Programming Note DAS 78-2.

Mueller, A.H., 1970, Phys. Rev. D2, 2963.

Nagy, E. et al., 1979, Nucl. Phys. B150, 221.

Napier, A., 1977, P.W.G.P. Documentation, APC Programming Note, 77-11.

_____1979, GAMMA -- A Shower Location and Fitting Program for the Prototype Forward Gamma Detector, unpublished note.

Perl, M.L., 1974, High Energy Hadron Physics, Chapters 2-3, John Wiley and Sons, New York.

Pless, I.A., 1965, PEPR System, IEEE Trans. on Nucl. Sci., Vol. N 12, No. 4.

Snyder, A.E., 1975, Ph.D. Thesis, Univ. of Illinois at Urbana-Champaign.

Sternheimer, R.M., 1955, Phys. Rev. 99, 277.

Trepagnier, P.C., 1975, Ph.D. Thesis, M.I.T., Cambridge, Mass.

Van Hove, L. and K. Fiałkowski, 1976, Nucl. Phys. B107, 211.

Warshaw, M., 1978, CERBERUS 4.0 and 4.2, APC Programming Note, DAS 78-8.

Webb, P. et al., 1975, Phys. Lett. 55B, No. 3, 331.

Whitmore, J., 1974, Phys. Reports 10C, 273.

_____ 1976, Phys. Reports 24C, 1.

Winkelmann F.C., 1974, Phys. Lett. 48B, 273.

Yamamoto, R.K., 1975, PDP-11 On-Line System for 30-Inch Hybrid and 15-Foot Tagging, (unpublished note).

LIST OF FIGURES

1. s-channel view of diffractive scattering.

2. t-channel view of diffractive scattering.

3. Fermilab 30-Inch Bubble Chamber (horizontal section).

4. Fermilab 30-Inch Bubble Chamber (vertical section).

5. Fermilab 30-Inch Hybrid Spectrometer.

6. Acceptance vs. track momentum for the downstream PWC system.

7. Film analysis and data processing chain.

8. Percentage of reject 99 events by topology.

9. Percentage of complete and charge-balanced events by topology.

10. Schematic of the Forward Gamma Detector.

11. Light pipes and phototube mounts in the scintillator hodoscope.

12. Calibration scheme for the lead glass blocks.

13. Calibration scheme for the scintillator hodoscope.

14. Energy deposited in the converter by 50 GeV electron showers.

15. Energy deposited in the absorber by 50 GeV electron showers.

16. Total energy deposited in the lead glass by 50 GeV (nominal) electron showers.

17. Linearity of the gamma detector response vs. electron beam energy.

18. Energy resolution vs. electron beam energy.

19. Average shower profile in one plane of the scintillator hodoscope.

20. GAMMA event processing sequence.

21. Energy deposited in the gamma detector by 147 GeV π^+.

22. Distribution of the number of charged tracks per event which strike the absorber.

23. Profile display of an event with three showers.

24. Histogram display of scintillator hodoscope data and triple search results.

25. Histogram display of the profile fit to three showers.

26. Results of an energy distribution fit to two showers in the absorber.

27. Profile display of an electron-positron pair.

28. Gamma detector acceptance for $\pi^0 \rightarrow \gamma\gamma$ vs. π^0 energy.

29. Gamma detector acceptance for $\pi^0 \rightarrow \gamma\gamma$ vs. η^0 energy.

30. Probability of resolving both gammas from $\pi^0 \rightarrow \gamma\gamma$ vs. π^0energy.

31. Average number of showers observed from $\pi^0 \rightarrow \gamma\gamma$ decay vs. π^0energy.

32. Invariant mass distribution for two-shower combinations in $\pi^+ p$ events.

33. Invariant mass distribution for two-shower combinations in pp events.

34. Feynman x distribution of π^0's from $\pi^+ p$ events.

35. Feynman x distribution of π^0's from pp events.

36. Transverse momentum distribution of π^0's from $\pi^+ p$ events.

37. Transverse momentum distribution of π^0's from pp events.

38. Rapidity distribution of π^0's from $\pi^+ p$ events.

39. Rapidity distribution of π^0's from pp events.

40. Laboratory momentum distribution of π^0's from $\pi^+ p$ events.

41. Laboratory momentum distribution of π^0's from pp events.

42. Plot of $\ln(N_-!\sigma_{N_-})$ vs. N_- for π^+p, K+p, pp events at 147 GeV/c.

43. Topological cross sections for the low multiplicity component from two component fits.

44. Feynman x distribution for charged particles in 2-prong π^+p events.

45. Rapidity distribution for charged particles in 2-prong π^+p events.

46. Feynman x distribution for charged particles in 4-prong π^+p events.

47. Rapidity distribution for charged particles in 4-prong π^+p events.

48. Feynman x distribution for charged particles in 6-prong π^+p events.

49. Rapidity distribution for charged particles in 6-prong π^+p events.

50. Rapidity gap between charged particles for 2-prong π^+p events.

51. Largest rapidity gap between adjacent particles (in rapidity) for 4-prong π^+p events.

52. Location of the largest gap in the ordered rapidity chain for 4 - 12 prong proton-proton events.

53. Location of the largest gap in the ordered rapidity chain for 4 - 12 prong π^+- proton events.

54. Average size of rapidity gaps according to order vs. prong count for proton-proton events.

55. Average gap sizes for uniformly distributed particles in a unit rapidity interval.

56. Average gap sizes for proton-proton events, normalized to the rapidity interval between beam and target.

57. Topological cross sections for the diffractive π^+p and pp events.

58. Multiplicity distributions for proton-proton events: a) all; b) events with the largest rapidity gap on the end of the chain; c) largest gap at the end, and $|x| > .75$ for the end particle.

59. Multiplicity distributions for π^+-proton events corresponding to those in figure 58.

60. x distribution of positives from pp events.

61. Distribution of negatives from pp events,

62. Distribuiton of protons from pp events.

63. Distribution of positives from π^+p events.

64. Distribution of negatives from π^+p events.

65. Distribution of protons from π^+p events.

66. Comparison of $\frac{1}{\sigma_{inel}} \cdot \frac{d\sigma}{dx}$ for positive particles from pp and π^+p events.

67. Comparison of $\frac{1}{\sigma_{inel}} \cdot \frac{d\sigma}{dx}$ for negative particles from pp and π^+p events.

68. x distribution of charged particles in 4-prong proton-proton events having the largest rapidity gap near the target.

69. Rapidity distribution corresponding to Figure 68.

70. x distribution of charged particles in 4-prong proton-proton events having the largest gap between the two central particles (on the ordered rapidity chain).

71. Rapidity distribution corresponding to Figure 70.

72. x distribution of charged particles in 4-prong proton-proton events having the largest rapidity gap near the beam.

73. Rapidity distribution corresponding to Figure 72.

74. x distribution as in figure 68, with the additional requirement $x < -.75$ for the end particle.

75. y distribution corresponding to Figure 74.

76. x distribution of charged particles in the selected non-diffractive sample.

77. y distribution corresponding to Figure 76.

78. x distribution as in Figure 72, with the additional requirement $x > .75$ for the end particle.

79. y distribution corresponding to Figure 78.

80. Inclusive $\frac{d\sigma}{dx}$ for π^0's from π^+p events.

81. Inclusive $\frac{d\sigma}{dx}$ for π^0's from pp events.

82. Total energy deposited in the gamma detector for $\pi^{\pm}$ proton events.

83. Total energy deposited in the gamma detector for proton-proton events.

84. Invariant x distribution of gammas from π^+p events.

85. Invariant x distribution of gammas from pp events.

86. Lab. energy distribution of detected showers in π^+p events.

87. Lab. energy distribution of detected showers in pp events.

88. Invariant mass distribution for $\pi^+\pi^-$ combinations.

89. Invariant mass distribution for $\pi^+\pi^-$ combinations with $x(\pi^+\pi^-) > 0.4$.

90. Invariant mass distribution for $\pi^+\pi^0$ combinations.

91. Invariant mass distribution for $\pi^+\pi^0$ combinations with $x(\pi^+\pi^0) > 0.4$.

92. Invariant mass distribution for $\pi^-\pi^0$ combinations.

93. Invariant mass distribution for $\pi^-\pi^0$ combinations with $x(\pi^-\pi^0) > 0.4$.

LIST OF TABLES

I.	Leading Particle Cross Sections for $\pi^- p$ at 147 GeV/c.	20
II.	Vertex Types.	39
III.	Event Summary.	49
IV.	Topological Cross Sections in pp Interactions at 147 GeV/c.	50
V.	Topological Cross Sections in $\pi^+ p$ Interactions at 147 GeV/c.	51
VI.	Forward Gamma Event Summary	99
VII.	Inclusive $\pi^+ p$ Shower Distribution.	100
VIII.	Inclusive pp Shower Distribution.	100
IX.	Selection Criteria for π^0's.	105
X.	Results of Poisson fit to $N \geq 10$ Prong Cross Sections.	111
XI.	Cross Sections for the Low Multiplicity Component.	111
XII.	Results of a two Poisson Fit to the Multiplicity Distributions	114
XIII.	Diffractive Cross Sections for $\pi^+ p$ and pp at 147 GeV/c.	131
XIV.	Distribution of Showers in Leading Beam Events.	158
XV.	Distribtuion of π^0's in Leading Beam Events.	158
XVI.	Distribution of Showers in the Leading Target Events.	160
XVII.	Distribution of π^0's in the Leading Target Events.	160